Doc.No.: SPIN-UB-ATBD-2.02
Version: 2.02.1
Date: April 2, 2014

ESA SPARC Initiative – SPIN

Algorithm Theoretical Baseline Document

– ATBD –

Version 2.02.1

Greg Bodeker[3]
Adam Bourassa[2]
Lena Brinkhoff[1]
John Burrows[1]
Andreas Jonsson[6]
Erkki Kyrölä[4]
Charles McLandress[6]
Andreas Penckwitt[3]
Patricia Liebing[1]
Landon Rieger[2]
Alexei Rozanov[1]
Simo Tukiainen[4]
Joachim Urban[5]
Katja Weigel[1]

[1] Institute of Environmental Physics, University of Bremen, Germany
[2] Institute for Space and Atmospheric Sciences, University of Saskatchewan, Canada
[3] Bodeker Scientific, Alexandra, New Zealand
[4] Finnish Meteorological Institute, Helsinki, Finland
[5] Department of Earth and Space Sciences, Chalmers University of Technology, Gothenburg, Sweden
[6] Department of Physics, University of Toronto, Canada

April 2, 2014

Contents

Document Properties

Reference	SPIN-UB-ATBD-2.02
Issue	2.02.1
Revision	00
Status	Draft
Date of issue	April 2, 2014
Document type	Deliverable

	Function	Name	Date
Lead author	Deliverable Coordinator	Patricia Liebing	April 2, 2014
Contributing authors	WP authors	Greg Bodeker Adam Bourassa Lena Brinkhoff John Burrows Andreas Jonsson Erkki Kyrölä McLandress Andreas Penckwitt Patricia Liebing Landon Rieger Alexei Rozanov imo Tukiainen Joachim Urban Katja Weigel	
Reviewed by			
Approved by			
Issued by			

Change Record and Distribution List

Document Change Log

Version	Date	Section/Page	Description
Draft 1.00	August 23, 2012	all	new document
Draft 1.01	September 19, 2012	7.1, 7.2	added
		1	minor changes
		author list	added J. Urban
Draft 1.02	March 24, 2013	1.1	added description of ATBD principle
		2	added
		3.1	data version 7.03→7.04
		3.1	Eqs. 3.4, 3.6 updated
		3.1.2.3	Henyey-Greenstein part replaced by Mie phase function description
		3.1.4	added
		6.1	added version number
		6.1.1	added influence of different L1 versions
		6.1.13	added error estimates
		6.1.12	added figure 6.1
		5.1	updated text, added fig. 5.1
		5.1.2.1(3)	removed
		4.1	added/changed first 2 paragraphs
		8	added
Draft 2.01	September 10, 2013	5.2	added
		3.3	added
		7	minor updates to sections 7.1 and 7.2
Draft 2.02	February 20, 2014	3.3.3 and 3.3.4	removed
		3.3.3	added
		3.3.1, 3.3.2	updated
		6.1	minor corrections
		5.1	updated
		5.2	updated, divide section into BS and FMI approach
		5.3	added, divide section into BS and FMI approach
		4.3	added
		4.4	added
		6.2	added
	April 2, 2014	4.2	added
		5.4	added

Distribution List

- ESA

1 Introduction

This document was prepared by the SPIN consortium as deliverable D6 of the ESA SPARC Initiative (SPIN) project. The main scope of this project is to make use of ESA and ESA Third-Party Mission data to establish climate quality stratospheric data records from satellite instruments for the four essential climate variables of ozone, aerosol, water vapor and temperature in the stratosphere. The document aims at the facilitation of the use of these data products.

This work is supported by the European Space Agency.

1.1 Purpose and Scope

Algorithm Theoretical Baseline Documents (ATBD) were originally created within NASAs Earth Observing System. The approach has been accepted by all relevant space agencies. ATBDs are intended to describe the physical background or theory, the mathematical foundation and inversion techniques used to derive data products. All assumptions applied to the data are explained and justified. In general, ATBDs are written for different levels of product e.g. level 0 to 1, level 1 to 2 etc. The levels of data product are defined as follows: Level 0 data are raw instrument data, often in engineering units, as recorded by the instrument. Level 1 data are related variables after the application of a raw signal to the measurement algorithm, e.g. radiance at the top of the atmosphere. Level 2 data are the geophysical variables, e.g. trace gas or aerosol profiles at a given location and time of the observation. Level 3 data (products) usually take the form of a homogeneous regularly gridded field. Level 4 data are products derived from further processing and consolidation of Level 3 data (value-adding). The geophysical quantities are then available to the scientific community for studies of the various characteristics of the Earth system. The ATBD approach was developed to meet the need of the entire user community to assess the information content of a data product, its precision and accuracy.

In the context of the SPIN project. the Algorithm Theoretical Baseline Document describes the algorithms used within the various work packages of the SPIN project to generate the delivered data products. This comprises the specification of the data sets used, the description of the applied filtering and processing steps and of the theoretical assumptions or model parameters involved in the algorithms. It also contains an uncertainty assessment where possible. It does not include the algorithms to obtain the input data such as the calibrated data from satellite instruments.

The document is structured into four chapters for each climate variable considered within the project. Each section contains the description of the algorithm for one particular deliverable data product.

2 Scientific Background and Motivation

The scientific objective of the SPIN project is to characterize or extent existing and to establish new Climate Data Records (CDR) for four essential variables in the stratosphere (ozone, water vapor, temperature and aerosols). The explicit goal of SPIN is to make use of ESA and ESA Third Party missions (TPM) in order to continue and complement the CDRs so far obtained mainly using data by US (NASA and NOAA) missions.

CDRs usually contain a synergy of observations by several instruments combined in such a way that instrument specific errors are minimized and spatial and temporal coverage is optimized. While the SPARC CDRs currently rely heavily on data from solar occultation instruments which were operational until around 2005, the inclusion of ESA and ESA-TPM mission data will not only extent these CDRs in time but also by numerous novel measurement techniques. These include limb scatter observations in a wide spectral range (SCIAMACHY and OSIRIS, bright limb observations by GOMOS) as well as stellar occultation technique (GOMOS). The addition of these new data therefore significantly improves the spatio-temporal coverage of the CDRs.

The use of these new measurement techniques requires the application of novel analysis methods in order to account for complications due multiple scattering in limb observations or scintillations in stellar occultation measurements. Therefore, a considerable amount of time during phase 1 of the project will be assigned to the investigation and maturation of data products obtained from such measurements.

This Algorithm Theoretical Baseline document will describe the algorithms applied to obtain the matured individual data sets and the revised or new climatologies of stratospheric temperature and short lived species as outlined in Task 2 as well as the procedures used to obtain the merged data sets within Tasks 3 and 4 of the project.

Within the first phase of SPIN this comprises the description of the matured SCIAMACHY and OSIRIS aerosol data, the SCIAMACHY water vapor product and the GOMOS bright limb ozone product. The generation of stratospheric temperature climatologies for ACE-FTS, MIPAS, SMR and radio occultation data and of climatologies for short lived species are outlined here as well. Within phase 2 of SPIN the data sets of stratospheric temperature and ozone are to be compared to and merged with historical data records to create long term climatologies. In addition, a path to merging climatologies for aerosols (including the limb scatter data) and water vapor with the corresponding historical records based on extensive comparison studies is to be outlined.

3 Algorithm Theoretical Baseline – Aerosol

3.1 Algorithms for the Maturation of Aerosol Products – SCIAMACHY (WP–12)

This section is adapted from Ernst et al. (2012).

The retrieval of stratospheric aerosols is based on SCIAMACHY Level 1 data version 7.04. The Level 1 data are calibrated with all calibration options but flags 0, 6, and 7, i.e., memory effect correction, polarization correction and absolute calibration were not performed due to remaining issues with these calibration steps.
The stratospheric aerosol extinction profiles are retrieved from SCIAMACHY limb-radiance profiles at two wavelengths using a color-index approach. The two wavelengths are $\lambda_s = 470$ nm and $\lambda_l = 750$ nm. Spectral windows with weak atmospheric absorption are selected in order to avoid retrieval errors caused by incorrect knowledge of absorber profiles. Both wavelengths used are sufficiently distant from the center of the Chappuis absorption band of O_3 near 600 nm. λ_s falls between an NO_2 and the Chappuis absorption band, and λ_l is just below the O_2 A-band. The measurement vector required for the retrieval is derived from the limb-radiance profiles at the two wavelengths using a 2-step approach following the method previously used by Bourassa et al. (2007).
First we normalize the limb-radiance at each tangent height with the radiance at a reference tangent height of the same limb-radiance profile:

$$I_N^{\lambda}(TH) = I^{\lambda}(TH)/I^{\lambda}(TH_{ref}) \tag{3.1}$$

This technique is adapted from trace gas retrievals (e.g., Flittner et al., 2000; von Savigny et al., 2003). It has two advantages: first, an absolute calibration of the limb-radiances is not required. Furthermore, von Savigny et al. (2003) showed that the tangent height normalization leads to a reduced sensitivity to errors in the assumed ground albedo. This is based on the assumption that the fraction of ground-reflected sunlight in the limb-radiance is similar at all tangent heights, including the reference tangent height. A reference tangent height (TH_{ref}) of about 35 km is chosen because at this point (and above) the aerosol loading in the atmosphere is small under background conditions. Above that tangent height the SCIAMACHY limb measurements are potentially contaminated by external or "baffle" stray light.

In a second step we combine the normalized limb-radiance profiles at the two wavelengths in a color-index-ratio. Retrieving aerosol extinction profiles from limb-radiance profiles at a single wavelength is also an option, but it relies on the assumption that the background Rayleigh atmosphere can be modeled perfectly. Any uncertainty in the neutral density would result in an error in the aerosol profile. To reduce this effect, it is suitable to use the ratio of a long to a short wavelength. Since the Ångstrøm exponent for Mie-scattering is highly variable – but for stratospheric aerosols generally significantly smaller than for Rayleigh scattering ($\alpha \approx 4$) – wavelength pairing provides a suitable measurement vector for the retrieval of stratospheric aerosols. Instead of the simple ratio of the two normalized limb-radiance profiles, we use the natural logarithm of the ratio as the retrieval vector for the inversion (see below). The wavelength pairing can then be described mathematically as follows:

$$y(TH) = \ln\left(\frac{I_N^{\lambda_l}(TH)}{I_N^{\lambda_s}(TH)}\right) \tag{3.2}$$

Obtaining stratospheric aerosol extinction coefficient profiles from SCIAMACHY limb-radiance profiles is an inverse problem, requiring the inversion of the following generic equation:

$$\mathbf{y} = \mathbf{K}\mathbf{x} + \epsilon, \tag{3.3}$$

where $\mathbf{y}$ is the measurement vector containing logarithms of the normalized and paired limb-radiance profiles at each selected tangent height – as described above. $\mathbf{x}$ is the so-called state vector, representing the height distribution of the desired atmospheric parameter, i.e., in this case the aerosol extinction coefficient at each altitude. $\mathbf{K}$ is the weighting function matrix or Jacobian matrix which contains logarithmic weighting functions for the aerosol extinction coefficient at tangent heights from about 11.5 km to 31.5 km (tangent height numbers 6 to 12). ϵ contains all errors. In order to solve the inversion problem we employ the optimal estimation technique – briefly described in the following Sect. 3.1.1 – in combination with the radiative transfer model SCIATRAN – described in Sect. 3.1.2.

3.1.1 Retrieval technique

In SCIATRAN, Eq. (3.3) is used in form of

$$\hat{\mathbf{y}} = \mathbf{K}\hat{\mathbf{x}} + \epsilon, \tag{3.4}$$

where $\hat{\mathbf{y}} = \mathbf{y} - \mathbf{y_0}$ is the measurement vector containing the differences between logarithms of measured and simulated spectra (both normalized and paired) and $\hat{\mathbf{x}} = (\mathbf{x} - \mathbf{x_0})/\mathbf{x_0}$ is the state vector containing relative differences between the a priori and retrieved aerosol extinction profiles. Following Rodgers (2000), the solution of Eq. (3.4) is found as

$$\mathbf{x} = \mathbf{x}_0 + (\mathbf{K^T}\mathbf{S_y^{-1}}\mathbf{K} + \mathbf{S}_a^{-1})^{-1}\mathbf{K^T}\mathbf{S_y^{-1}}(\mathbf{y} - \mathbf{y}_0)\mathbf{x}_0 \tag{3.5}$$

with $\mathbf{S}_\mathrm{a}$ as the a priori covariance matrix and $\mathbf{S}_\mathrm{y}$ as the noise covariance matrix. Because of the non-linearity of the problem, the forward model and retrieval code SCIATRAN version 3.1 (Rozanov et al., 2005) is used to find the solution iteratively:

$$\mathbf{x}_{i+1} = \mathbf{x}_i + (\mathbf{K^T}_i\mathbf{S}_y^{-1}\mathbf{K}_i + \mathbf{S}_a^{-1})^{-1}\mathbf{K^T}_i\mathbf{S}_y^{-1}(\mathbf{y} - \mathbf{y}_i)\mathbf{x}_i \tag{3.6}$$

with $\mathbf{S}_\mathrm{i} = (\mathbf{K^T}_\mathrm{i}\mathbf{S}_\mathrm{y}^{-1}\mathbf{K}_\mathrm{i} + \mathbf{S}_\mathrm{a}^{-1})^{-1}$ as the solution covariance matrix.
The noise covariance matrix is chosen to be diagonal, i.e., the errors are assumed to be uncorrelated. A signal to noise ratio of 200 is used for all tangent heights and spectral points. In terms of the a priori covariance matrix the non-diagonal elements drop off exponentially with a correlation radius of 3.3 km and the diagonal elements correspond to a relative standard deviation of 1.

3.1.2 Input to the retrieval

3.1.2.1 SCIATRAN

SCIATRAN is a linearized radiative transfer model designed to simulate the scattered solar radiation and the weighting functions of various atmospheric parameters in the UV-Visible-near-IR spectral range for any viewing geometry (nadir, zenith, off-axis, limb, etc.) and any observer position within and outside the atmosphere. The software package also contains a retrieval algorithm, which can be easily adjusted to solve a wide range of scientific tasks. For the retrieval of aerosols from SCIAMACHY limb-measurements, the discrete ordinate solver of SCIATRAN 3.1 (Rozanov et al., 2005) was used. SCIATRAN allows for a field of view integration to take the finite vertical resolution of the SCIAMACHY limb-measurements into account. The retrieval altitude grid is a regular 1 km grid.

3.1.2.2 Auxiliary Data

The albedo values are taken from the Matthews data base (Matthews, 1983) and the temperature and pressure profiles for the location, date and time at each limb measurement are taken from the ECMWF Operational Atmospheric Model Data Sets.
The wavelength dependence of the aerosol extinction coefficient is determined by the assumed aerosol model. Trace gases are not considered.

3.1.2.3 Aerosol parameterization in SCIATRAN

For the retrieval, Version 1.1, the needed parameters are delivered manually to SCIATRAN by using a Mie phase function. As discussed among others by Deshler (2008), for background stratospheric aerosols the dominating smaller particle mode can be described by the lognormal size distribution with a median radius of r = 0.11 μm and a distribution width of $\sigma = 1.37$. These parameters have been adopted to calculate the aerosol phase function using a Mie code. In accordance to Yue et al. (1994) the real part of the refractive index of aerosol particles has been set to $n_r = 1.453$ at 450 nm and to $n_r = 1.446$ at 800 nm, while the imaginary part of $n_i = 10^{-8}$ has been used for both wavelengths.

3.1.2.4 A priori aerosol extinction profiles

The a priori aerosol extinction profiles required for the retrievals are determined with the ECSTRA model by Fussen and Bingen (1999). ECSTRA is a climatological model of vertical extinction coefficient profiles of stratospheric aerosols in the UV-Visible range as a function of wavelength, month, latitude, and volcanism level represented by the aerosol optical depth. The ECSTRA model is based on SAGE II stratospheric aerosol extinction profile data. ECSTRA provides aerosol extinction profiles above the tropopause only, and the tropopause height is taken – depending on latitude and month of the year – from the climatological tropopause height data set by Randel et al. (2000). The vertical structure of the ECSTRA aerosol profile climatology describes the tropopause region, the Junge layer and the high altitude domain (Fussen and Bingen, 1999).
The ECSTRA aerosol extinction profiles are extrapolated exponentially above 30 km with a scale height of 4 km, based on Thomason et al. (2006), and we remove the edge below the tropopause that is generated by the ECSTRA model.

3.1.3 Output

The retrieval output is the aerosol extinction coefficient at $\lambda_s = 470$ nm and $\lambda_l = 750$ nm for each tangent height in 1 km steps.

3.1.4 Error

The main error source of the retrieval Version 1.0 was the aerosol phase function, which has been improved in Version 1.1. A sensitivity study for the median radius of the phase function showed a maximum relative error in the retrieved aerosol extinction coefficients of - 100% for large radii (relative to r = 0.11 m) at the equator and + 100% to + 200% for very small radii in the southern hemisphere. Further potential error sources of Version 1.1 were tested by means of synthetic retrievals. The effect on the retrieved aerosol extinction of a ± 15% uncertainty in the ozone profile is below 1% for both a polar and tropical geometry. For a typical SCIAMACHY tangent height error of ± 200 m (von Savigny et al., 2009), the maximum error is 8% at 16 km and smaller than 5% above 20 km. The error due to uncertainties in the assumed surface albedo is up to 30% (at 40°S) when changing the true albedo from 0 to 1 and running the retrieval with A = 0.5. However, the application of a cloud screening – assuming tropospheric clouds below the SCIAMACHY measurement to be a major source for albedo uncertainties – does not improve the retrieval (see Ernst et al. (2012)). Furthermore, changing the

true neutral density by ± 3% by scaling the ground pressure of 1013 hPa by ± 30 hPa has an effect on the retrieved aerosol extinction, which is smaller than 20% below 20 km and smaller than 5% above. Finally, the impact of the a priori profile on the retrieval result has been analysed. The relative error due to the a priori profile using 6 modifications – multiplication with a factor of 0.5 and 2, a height shift of the complete profile by ± 3 km, and an artificial maximum and minimum around an altitude of 25 km – is smaller than 10%.

Bibliography

Bourassa, A. E., Degenstein, D. A., Gattinger, R. L., and Llewellyn, E. J., Stratospheric aerosol retrieval with optical spectograph and infrared imaging system limb scatter measurements, J. Geophys. Res., 112, D10217, 2007.

Deshler, T.: A review of global stratospheric aerosol: Measurement, importance, life cycle, and local stratospheric aerosol, Atmos. Res., 90, 223–232, doi:10.1016/j.atmosres.2008.03.016, 2008.

Ernst, F., von Savigny, C., Rozanov, A., Rozanov, V., Eichmann, K.-U., Brinkhoff, L. A., Bovensmann, H., and Burrows, J. P., Global stratospheric aerosol extinction profile retrievals from SCIAMACHY limb-scatter observations, Atmos. Meas. Tech. Discuss, 5, 5993–6035, 2012.

Flittner, D. E., Bhartia, P. K., and Herman, B. M., O3 profiles retrieved from limb scatter measurements: Theory, Geophys. Res. Lett., 27(17), 2601–2604, doi:10.1029/1999GL011343, 2000.

Fussen, D. and Bingen, C., A volcanism dependent model for the extinction profile of stratospheric aerosols in the UV-visilble range, Geophys. Res. Lett., 26(6), 703–706, 1999.

Matthews, E., Global vegetation and land use: new high resolution data base for climate studies, J. Climate Appl. Meteor., 22, 474–487, 1983.

Randel, W., Wu, F., and Gaffen, D., Interannual variability of the tropical tropopause derived from radiosonde data and NCEP reanalyses, J. Geophys. Res., 105(D12), 15509–15523, 2000.

Rodgers, C. D., Inverse Methods for Atmospheric Sounding: Theory and Practice, World Scientific, Singapore, 2000.

Rozanov, A., Rozanov, V., Buchwitz, M., Kokhanovsky, A., and Burrows, J. P., SCIATRAN 2.0 - A new radiative transfer model for geophysical applications in the 175–2400 nm spectral region, Adv. Space Res. 36(5), 1015–1019, doi:10.1016/j.asr.2005.03.012, 2005.

von Savigny, C., Haley, C. S., Sioris, C. E., McDade, I. C., Llewellyn, E. J., Degenstein, D., Evans, W. F. J., Gattinger, R. L., Griffioen, E., Kyrölä, E., Lloyd, N. D., McConnell, J. C., McLinden, C. A., Mégie, G., Murtagh, D. P., Solheim, B., and Strong, K., Stratospheric ozone profiles retrieved from limb scattered sunlight radiance spectra measured by the OSIRIS instrument on the Odin satellite, Geophys. Res. Lett., 30(14), 1755, doi:10.1029/2002GL016401, 2003.

von Savigny, C., Bovensmann, H., Bramstedt, K., Dikty, S., Ebojie, F., Jones, A., Noël, S., Rozanov, A., and Sinnhuber, B.-M.: Indications for long-term trends and seasonal variations in the SCIAMACHY Level 1 version 6.03 tangent height information, SCIAMACHY Technical Note, TN-IUP-scia-pointing-2009-01, University of Bremen, Bremen, 2009.

Thomason, L.W., Peter, Th., Carslaw, K. S., Kärcher, B., Notholt, J., Bingemer, H., Hamill, P., Brogniez, C., Deshler, T., Anderson-Sprecher, R., Weisenstein, D. and Bekki, S., SPARC Assessment of Stratospheric Aerosol Particles, World Climate Research Programme (WCRP) SPARC Project Report (4), 1–320, 2006.

Yue, G. K., Poole, L. R., Wang, P.-H., and Chiou, E. W.: Stratospheric aerosol acidity, density, and refractive index deduced from SAGE II and NMC temperature data, J. Geophys. Res., 99(D2), 3727–3738, doi:10.1029/93JD02989, 1994.

3.2 Algorithms for the Maturation of Aerosol Products – OSIRIS (WP–12)

This algorithm theoretical basis document describes the retrieval of stratospheric aerosol extinction and Ångström coefficients on a scan-by-scan basis using the limb scatter OSIRIS instrument (*Llewellyn et al.*, 2004) onboard the Odin satellite.

3.2.1 Algorithm Overview

Currently, stratospheric aerosol extinction is retrieved by OSIRIS using a single 750 nm measurement vector and a multiplicative algebraic reconstruction technique (MART) as described in detail by *Bourassa et al.* (2007, 2011). For these retrievals a lognormal particle size distribution of the form,

$$\frac{dn(r)}{dr} = \frac{n_{\text{aer}}}{r\ln(\sigma_g)\sqrt{2\pi}} \exp\left(-\frac{(\ln r - \ln r_g)^2}{2\ln(\sigma_g)^2}\right), \tag{3.7}$$

is assumed with a mode radius, r_g, of 80 nm and mode width, σ_g, of 1.6, as is typical of stratospheric aerosol during volcanically quiescent periods (*Deshler et al.*, 2003). The number density, n_{aer}, is then retrieved and converted to extinction to decrease the dependence on the particle size assumptions. While extinction is much less sensitive to the assumed parameters (*McLinden et al.*, 1999), error in the assumed size distribution still biases the retrieved extinction. This work seeks to extend the current algorithm to retrieve an estimate of aerosol particle size and improve the retrieved extinction.

The aerosol signal detected by a limb scatter instrument is highly wavelength dependent and incorporation of this dependence can be used to improve the determination of aerosol extinction as well as retrieve information about particle microphysics. This technique uses OSIRIS measurements at two wavelengths, 750 nm and 1.53 μm to retrieve two parameters of a unimodal lognormal distribution, the number density and mode radius. These are then converted to a 750 nm aerosol extinction and the Ångström coefficient to decrease the dependence on particle size assumptions. Inversion of the OSIRIS measurements are performed using SASKTRAN, a fully spherical multiple scattering radiative transfer model (*Bourassa et al.*, 2008), to iteratively compute the atmospheric state.

3.2.2 The Aerosol Measurement Vector

To maximize the sensitivity to aerosols the radiance measurements, I, are first normalized in log space by a modeled measurement, I_{Ray}, in a clean, aerosol free atmosphere.

$$y_j(\lambda) = \ln\left(\frac{I(\lambda, j)}{I_{\text{Ray}}(\lambda, j)}\right). \tag{3.8}$$

To minimize the sensitivity of the aerosol measurement to an unknown surface albedo and tropospheric clouds and eliminate the need for an absolute calibration, the radiance measurements are then normalized by one or more high altitude measurements (*von Savigny et al.*, 2003). To select altitudes which are above the bulk of the aerosol layer and below altitudes which are contaminated by stray light, altitudes are chosen in which the measurement vector given by Equation 3.8 is at a minimum. Any altitudes with a measurement vector within 0.01 of the minimum are then used for normalization. This provides the final measurement vector,

$$y_j(\lambda) = \ln\left(\frac{I(\lambda, j)}{I_{\text{Ray}}(\lambda, j)}\right) - \frac{1}{N}\sum_{j=m}^{m+N} \ln\left(\frac{I(\lambda, j)}{I_{\text{Ray}}(\lambda, j)}\right), \tag{3.9}$$

where N lines-of-sight, from tangent altitude $j = m$ to $m+N$ are used in the normalization. Typically, this results in normalization between 35 and 40 km in the tropics, extending to lower altitudes at higher latitudes (*Bourassa et al.*, 2011).

3.2.3 Aerosol Inversion

3.2.3.1 Albedo retrieval and MART Initialization

The OSIRIS version 5 aerosol algorithm (*Bourassa et al.*, 2011) is used as the *a priori* estimate of aerosol extinction and particle size for the improved retrieval. First, an effective Lambertian surface albedo must be retrieved due to the strong effect of albedo on the retrieved aerosol. Albedo is retrieved by modeling the 750 nm OSIRIS signal at the normalization altitude for albedo values of 0, 0.25, 0.5, 0.75 and 1 using the *a priori* aerosol values. The modeled radiances are then linearly interpolated from the nearest modeled values to find the retrieved albedo.

The aerosol number density is then retrieved using the MART technique (*Lloyd and Llewellyn*, 1989) assuming a single mode lognormal particle size distribution with a mode radius of 80 nm and mode width of 1.6. For this, an *a priori* aerosol profile is chosen with very low values at all altitudes to ensure the Jacobian is positive and to maximize the retrieval range. At each iteration the aerosol number density at altitude j is updated based on the ratio of the measurement, y, to the model, $F(\hat{\mathbf{x}}^{(n)}, \tilde{\mathbf{b}})$,

$$\hat{x}_i^{(n+1)} = \hat{x}_i^{(n)} \sum_j \frac{y_j}{F_j(\hat{\mathbf{x}}^{(n)}, \tilde{\mathbf{b}})} W_{ji}. \tag{3.10}$$

For the aerosol retrieval, the weighting matrix, $\mathbf{W}$, is simply the identity matrix and MART simplifies to a Chahine relaxation (*Chahine*, 1970, 1972). Ten iterations are performed to ensure convergence. Albedo is then re-retrieved and then aerosol is again retrieved with ten iterations using the updated albedo. This provides a stable albedo and aerosol product with further iterations typically changing albedo by less than 1%.

3.2.3.2 Coupled Extinction and Particle Size Retrieval

Although three parameters are required to fully describe the lognormal distribution only two independent measurements are taken, requiring the mode width to be assumed constant at 1.6. The number density and mode radius are then the two quantities which are retrieved. Solving for the atmospheric state is equivalent to searching the two dimensional solution space for the point which minimizes the difference between the model and the measurements. There are several possible methods for this, however for multidimensional non-linear problems Levenberg-Marquardt is often used, as it provides a good combination of speed and robustness (*Marquardt*, 1963). Each iteration of the atmospheric state at altitude j is then given by

$$\hat{x}_j^{(n+1)} = \hat{x}_j^{(n)} + \left(\mathbf{K}_j^{\mathrm{T}}\mathbf{K}_j + \gamma \mathrm{diag}(\mathbf{K}_j^{\mathrm{T}}\mathbf{K}_j)\right)^{-1} \mathbf{K}_j^{\mathrm{T}} \left(y_j - F_j(\hat{\mathbf{x}}^{(n)}, \tilde{\mathbf{b}})\right). \tag{3.11}$$

Jacobian Calculation

The Jacobian, $\mathbf{K}$ for each line-of-sight is assumed to be independent, with no altitude coupling. While possible to compute the full Jacobian with altitude coupling terms, the computational time is prohibitive and for long wavelengths the altitude coupling is relatively small. Inclusion is then unnecessary for convergence and the Jacobian for a particular altitude, j, can be written,

$$\mathbf{K}_j = \begin{pmatrix} \dfrac{\partial y_j(750\,nm)}{\partial r_g} & \dfrac{\partial y_j(750\,nm)}{\partial n_{\mathrm{aer}}} \\ \dfrac{\partial y_j(1.53\mu m)}{\partial r_g} & \dfrac{\partial y_j(1.53\mu m)}{\partial n_{\mathrm{aer}}} \end{pmatrix}. \tag{3.12}$$

Calculation of the Jacobian is performed numerically at each iteration by successively perturbing the entire aerosol number density and mode radius profiles by 5% and recomputing the measurement vectors. Each Jacobian element is then found through the forward difference before and after perturbation.

Damping Factor

Ideally, the damping factor is calculated such that the step is taken within an approximately linear region of the solution space. *Marquardt* (1963), suggested assuming an initial $\gamma = \gamma_0$, calculating a step, and performing the iteration. If the residual is increased, the step is rejected and γ is increased by a factor of ν. This is repeated until the step improves the residual and the iteration is kept. If the solution is improved sufficiently, γ can be reduced so the next iteration takes a larger step to decrease the number of iterations required for convergence. The difficulty in applying this technique to a coupled problem is that the residual for a particular altitude may increase due to coupling despite the solution moving closer to the true state. As well, calculating a damping factor based on the total residual may keep γ unnecessarily large for most altitudes, slowing convergence. This problem can be avoided by using a less rigorous determination of γ based on Marquardt's method, but with the relaxed constraint that the γ is only increased if the total residual increases past a certain point relative to the previous iteration. While this does not guarantee convergence, proper choice of this threshold can provide good results that are relatively robust and less affected by the altitude coupling. For this algorithm γ_0 is set to 0.02 and the iteration is kept provided the total residual does not increase by more than 2%.

Retrieval Steps

The coupled retrieval of aerosol number density and mode radius then proceeds as follows:

1. Determine the aerosol number density profile using the *a priori* particle size estimate and MART retrieval on the 750 nm measurement.
2. Calculate the Jacobian numerically based on the current estimate.
3. Determine the improved mode radius and extinction estimate at each altitude independently using the Levenberg-Marquardt algorithm.
4. a) If the increase in the total residual is more than 2% reset the atmospheric state to the previous iteration, set $\gamma = \gamma \cdot 10$ and proceed to step 2.
   b) If the total residual is reduced by more than a factor of five keep the step, set $\gamma = \gamma/2$ and proceed to step 2.
   c) If the solution has converged or the iteration limit has been reached, stop.
   d) Otherwise, proceed to step 2.

Iterations are stopped by testing for convergence or a maximum iteration limit. Convergence is checked by testing the flatness of the solution space at the current location through the norm of the Jacobian; whether progress is being made towards a solution through the step size; and whether the model has matched the measurements sufficiently. The convergence limits for the code tested here are given in Table 3.1, and are said to be satisfied if any of the limits are met for all retrieved altitudes.

Table 3.1: Levenberg Marquardt convergence limits

Jacobian Norm	Step Size	Total Residual	Iteration Limit
10^{-5}	0.01%	10^{-4}	20

Retrieved Parameters

The retrieved quantities of number density and mode radius are highly dependent on the microphysical assumptions in the model, namely that the aerosol distribution is a single mode lognormal

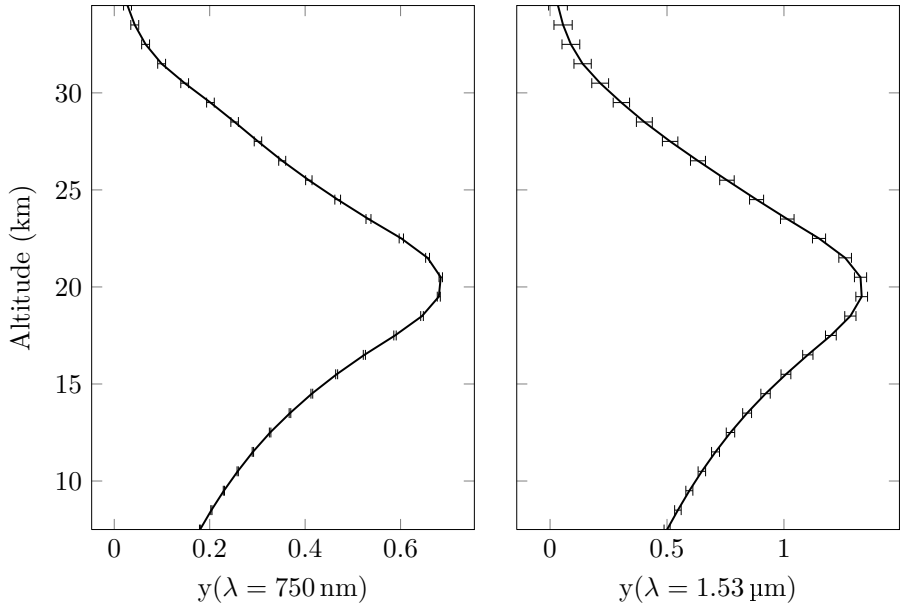

Figure 3.1: Measurement vectors shown with typical noise margins. Left panel is the 750 nm measurement and right panel is the 1.53 μm measurement.

with a mode width of 1.6. However, conversion of the retrieved parameters to more general quantities can decrease this dependence. Extinction is much less dependent on the microphysical assumptions than number density (*McLinden et al.*, 1999) and is converted using the formula:

$$k_{\text{aer}}(\lambda) = n_{\text{aer}}\sigma_{\text{aer}}(\lambda), \tag{3.13}$$

where k_{aer} is the extinction and σ_{aer} the scattering cross section. Similarly, the mode radius is converted to an Ångström coefficient, α, using

$$\left(\frac{\lambda_1}{\lambda_2}\right)^{-\alpha} = \frac{\sigma_{\text{aer}}(\lambda_1)}{\sigma_{\text{aer}}(\lambda_2)}, \tag{3.14}$$

where λ_1 and λ_2 are the 750 nm and 1.53 μm wavelengths respectively.

3.2.4 Error Analysis

The following sections estimate the error of the retrieved quantities using the methods detailed by *Rodgers* (2000). Generally, the inverse problem is linearized about the retrieved atmospheric state with error calculations based on the sensitivity of the retrieved quantities to small perturbations in either the measurements or true atmospheric state. Calculations below consider only the uncorrelated errors.

3.2.4.1 Measurement Error

The uncorrelated error in the measurement vector y_k at altitude j can be determined from error in the radiance measurement as,

$$\delta y_{jk} = \frac{\delta I_j(\lambda_k)}{I_j(\lambda_k)}. \tag{3.15}$$

Typical measurement errors for a scan are shown in Figure 3.1. The covariance matrix of the measurement error, $\mathbf{S}_\epsilon$, is the diagonal matrix with elements δy_i^2. Propagation of this error through the

forward model is determined from the sensitivity of the retrieved quantity, $\hat{\mathbf{x}}$, to the measurement, $\mathbf{y}$, also known as the gain matrix, $\mathbf{G}$,

$$\mathbf{G} = \frac{\partial \tilde{\mathbf{x}}}{\partial \mathbf{y}}. \tag{3.16}$$

The covariance matrix of the retrieved quantity is then,

$$\mathbf{S}_m = \mathbf{G}\mathbf{S}_\epsilon\mathbf{G}^{\mathrm{T}}, \tag{3.17}$$

with the square root of the diagonal elements yielding the uncorrelated errors for the retrieved quantities.

3.2.4.2 Smoothing Error

Smoothing error results from the fact that measurements are not of a single point, but smoothed by an averaging kernel. Fluctuations in the true state with a higher resolution than the averaging kernel are thus undetectable, or largely so, and contribute to measurement error. This can be seen from computation of the averaging kernel, $\mathbf{A}$, which determines the change in the retrieved state, $\hat{\mathbf{x}}$, for a change in the true state, $\mathbf{x}$, or

$$\mathbf{A} = \frac{\partial \hat{\mathbf{x}}}{\partial \mathbf{x}}. \tag{3.18}$$

The magnitude of the smoothing error, $\boldsymbol{\epsilon}_s$, is then

$$\boldsymbol{\epsilon}_s = (\mathbf{A} - \mathbf{I})(\mathbf{x} - \mathbf{x}_a). \tag{3.19}$$

The uncorrelated smoothing error is calculated as the diagonal elements of $(\mathbf{A} - \mathbf{I})$ multiplied by the difference between the *a priori* and retrieved states, $(\mathbf{x} - \mathbf{x}_a)$.

3.2.4.3 Albedo Error

The albedo retrieval works well at 750 nm, however cannot be extended to the infrared imager due to lack of an absolute calibration. The current solution is the assumption that albedo is unchanged from 750 nm to 1.53 μm. While this assumption is certainly incorrect to some degree it is further complicated by the presence of a water vapor absorption band at 1.44 μm which extends slightly into the 1.53 μm detector's range. At stratospheric altitudes the water vapor mixing ratio is small, approximately 5 ppm (*Chiou et al.*, 1997), limiting the error in radiance to considerably less than that of measurement noise. At low altitudes however, water vapor can compose a substantial portion of the atmosphere, on the order of 1%, and ignoring water vapor is no longer valid. While retrievals are not performed at these low altitudes upwelling radiation in the water absorption bands will be systematically reduced, causing a reduction in the apparent albedo when compared to wavelengths outside of the absorption band. This likely leads to a systematic overestimation of the 1.53 μm albedo, although the amount will vary depending on atmospheric and ground conditions.

The magnitude of this error on the retrieved parameters can be determined in a similar fashion to the other error quantities through the formula

$$\boldsymbol{\epsilon}_b = \mathbf{G}\mathbf{K}_b(\mathbf{b} - \hat{\mathbf{b}}). \tag{3.20}$$

However, unlike measurement noise and smoothing errors, the error in albedo may be large, and the assumption that the forward model remains linear in the region of interest may be violated. A more accurate estimate of the error can be obtained by simulating retrievals with incorrect albedo values. Figure 3.2 shows the retrieved extinction and mode radius values for three cases where the true 1.53 μm albedo is 0.0, 0.5 and 1.0, while the assumed albedo is constant at 0.5. Both the true and assumed albedos for the 750 nm measurements are constant at 0.5 as well. The geometry of this scan was chosen to have a zenith angle of 72° and a scattering angle of 119° creating a relatively large

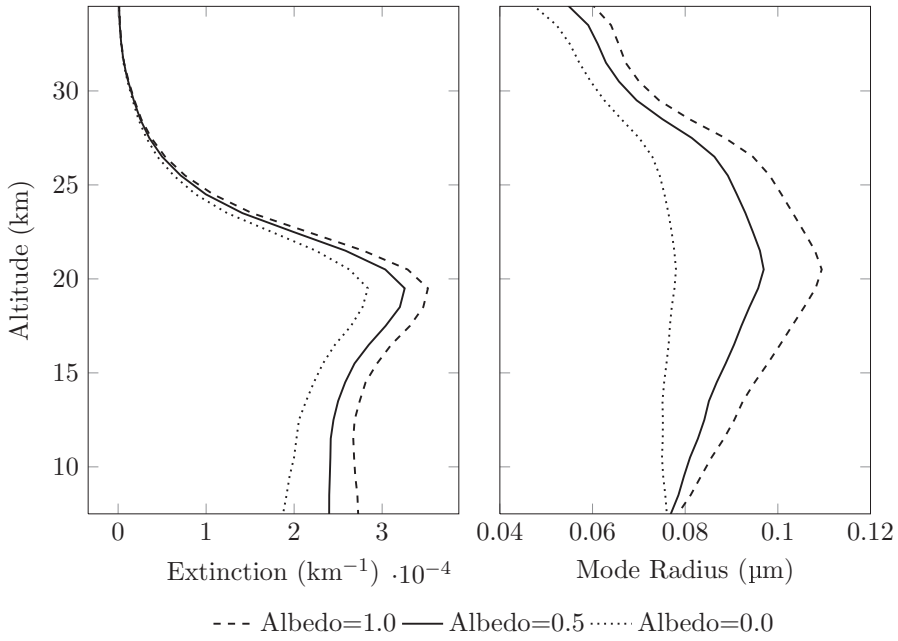

Figure 3.2: Error in the retrieval due to assumption that albedo is constant with wavelength.

albedo contribution to the total signal. If the true albedo is underestimated the measurement vector is systematically too large, leading to an increase of both particle size and extinction. For the geometry and cases tested the error due to incorrect albedo is approximately 15% for extinction and 30% for mode radius near the peak aerosol concentrations. The affect is also non-linear, with underestimation causing a larger error in both retrieved extinction and mode radius than overestimation. Note that this is close to a worst case, with albedo error of forward geometries for the same atmospheric conditions limited to less than 5% for both parameters.

The total error due these factors is summarized in Figure 3.3 as a percent of the true values for a strongly forward scatter geometry. At altitudes above 30 km and below 15 km error begins to dominate the signal, with virtually all of the error due to measurement noise. This is primarily due to the large error on the 1.53 μm measurements, which is approximately 5-10 times that of the 750 nm measurements.

3.2.4.4 Particle Size Error

Error due to incorrect particle size assumptions can be tested through simulated measurements and retrievals. The simulated atmosphere was assumed to be largely bimodal at lower altitudes, with coarse particles contributing approximately 50% of the overall extinction. The coarse mode fraction was decreased with altitude to simulate the sedimentation of larger particles, leading to an extinction due almost entirely to fine particles by 30 km. The fine mode parameters were also assumed incorrectly for the retrievals, with exact parameters given in Table 3.2. The simulated retrieval was tested with these atmospheric conditions for several hundred OSIRIS measurement geometries with results shown in Figure 3.4. The extinction and particle size retrieval has an error typically less than 10%, even when the true state is largely bimodal. The error in the retrieved Ångström coefficient is slightly larger, particularly at altitudes which are largely bimodal, however it still provides a large improvement over the *a priori* estimate.

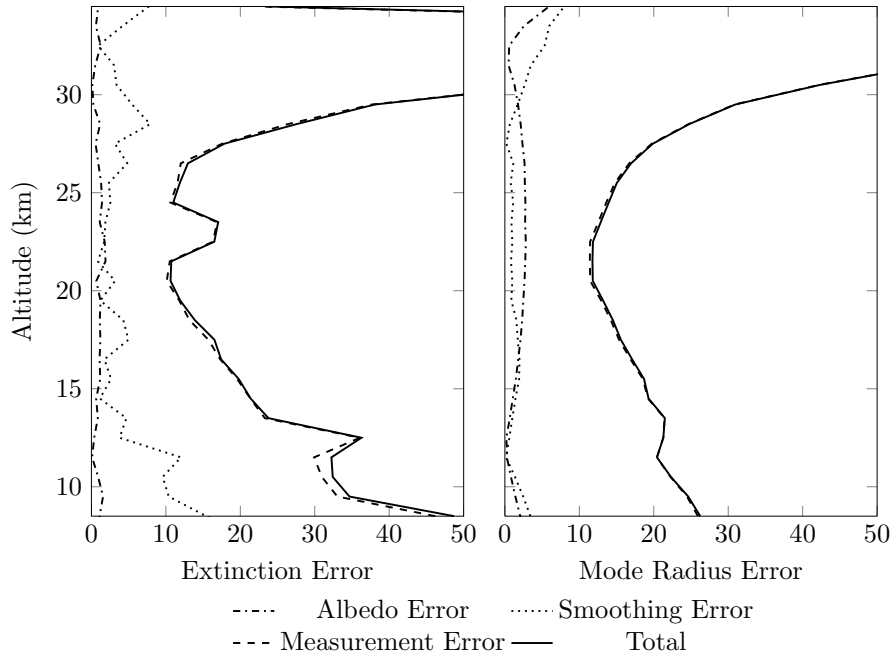

Figure 3.3: Total error in the retrieved quantities due to albedo, smoothing and measurement error contributions.

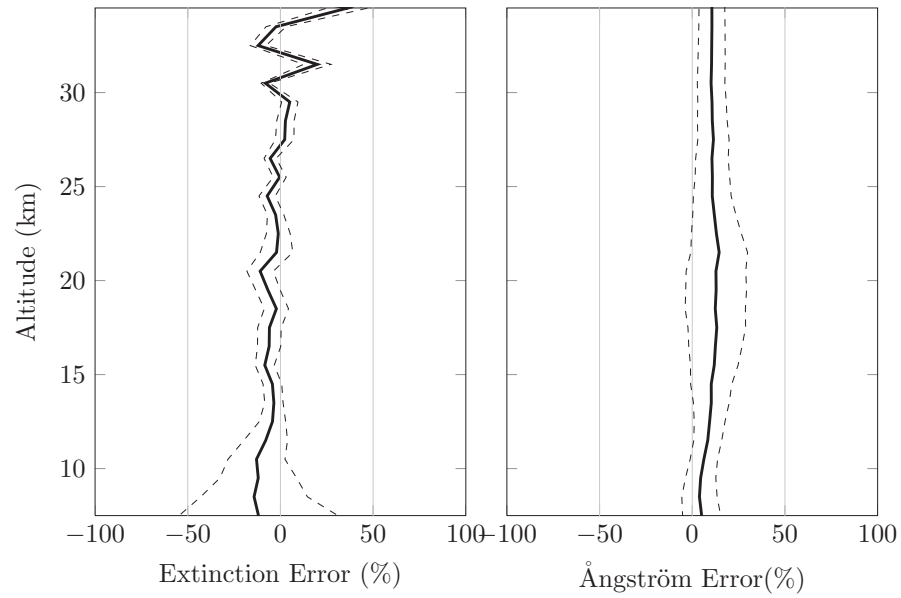

Figure 3.4: Error in the retrieved parameters under a variety of simulated measurement conditions when the true atmospheric state is bimodal. Percent error is shown as solid black line with standard deviation shown as dashed lines.

Table 3.2: Lognormal size parameters used in the simulated retrievals

Mode	MART Retrieval	Coupled Retrieval	True State
Fine Mode	$r_g = 80\,\text{nm}$ $\sigma_g = 1.60$	$r_g = N/A$ $\sigma_g = 1.60$	$r_g = 90\,\text{nm}$ $\sigma_g = 1.75$
Coarse Mode	$r_g = N/A$ $\sigma_g = N/A$	$r_g = N/A$ $\sigma_g = N/A$	$r_g = 400\,\text{nm}$ $\sigma_g = 1.20$

Bibliography

Bourassa, A. E., D. A. Degenstein, R. L. Gattinger, and E. J. Llewellyn (2007), Stratospheric aerosol retrieval with optical spectrograph and infrared imaging system limb scatter measurements, *J. Geophys. Res.*, *112*, D10,217, doi:10.1029/2006JD008079.

Bourassa, A. E., D. A. Degenstein, and E. J. Llewellyn (2008), SASKTRAN: A spherical geometry radiative transfer code for efficient estimation of limb scattered sunlight, *J. Quant. Spec. Radiat. Transf.*, *109*, 52–73, doi:10.1016/j.jqsrt.2007.07.007.

Bourassa, A. E., L. A. Rieger, N. D. Lloyd, and D. A. Degenstein (2011), Odin-OSIRIS stratospheric aerosol data product and SAGE III intercomparison, *Atmos. Chem. Phys. Discuss.*, *11*, 25,785–25,811, doi:10.5194/acpd-11-25785-2011.

Chahine, M. I. (1972), A General Relaxation Method for Inverse Solution of the Full Radiative Transfer Equation., *J. Atmos. Sci*, *29*, 741–747, doi:10.1175/1520-0469(1972)029⟨0741:AGRMFI⟩2.0.CO;2.

Chahine, M. T. (1970), Inverse Problems in Radiative Transfer: Determination of Atmospheric Parameters., *J. Atmos. Sci.*, *27*, 960–967, doi:10.1175/1520-0469(1970)027⟨0960:IPIRTD⟩2.0.CO;2.

Chiou, E. W., M. P. McCormick, and W. P. Chu (1997), Global water vapor distributions in the stratosphere and upper troposphere derived from 5.5 years of SAGE II observations (1986-1991), *J. Geophys. Res.*, *102*, 19,105–19,118, doi:10.1029/97JD01371.

Deshler, T., M. E. Hervig, D. J. Hofmann, J. M. Rosen, and J. B. Liley (2003), Thirty years of in situ stratospheric aerosol size distribution measurements from Laramie, Wyoming (41°N), using balloon-borne instruments, *J. Geophys. Res.*, *108*, 4167, doi:10.1029/2002JD002514.

Llewellyn, E., N. D. Lloyd, D. A. Degenstein, R. L. Gattinger, S. V. Petelina, A. E. Bourassa, J. T. Wiensz, E. V. Ivanov, I. C. McDade, B. H. Solheim, J. C. McConnell, C. S. Haley, C. von Savigny, C. E. Sioris, C. A. McLinden, E. Griffioen, J. Kaminski, W. F. J. Evans, E. Puckrin, K. Strong, V. Wehrle, R. H. Hum, D. J. W. Kendall, J. Matsushita, D. P. Murtagh, S. Brohede, J. Stegman, G. Witt, G. Barnes, W. F. Payne, L. Piche, K. Smith, G. Warshaw, D. L. Deslauniers, P. Marchand, E. H. Richardson, R. A. King, I. Wevers, W. McCreath, E. Kyrola, L. Oikarinen, G. W. Leppelmeier, H. Auvinen, G. Megie, A. Hauchecorne, F. Lefevre, J. de La Noe, P. Ricaud, U. Frisk, F. Sjoberg, F. von Scheele, and L. Nordh (2004), The OSIRIS instrument on the odin spacecraft, *Can. J. Phys.*, *82*, 411–422, doi:10.1139/p04-005.

Lloyd, N. D., and E. J. Llewellyn (1989), Deconvolution of blurred images using photon counting statistics and maximum probability, *Can. J. Phys.*, *67*, 89–+.

Marquardt, D. W. (1963), An algorithm for least-squares estimation of nonlinear parameters, *J. Soc. Ind. Appl. Math.*, *11*, pp. 431–441.

McLinden, C. A., J. C. McConnell, C. T. McElroy, and E. Griffioen (1999), Observations of Stratospheric Aerosol Using CPFM Polarized Limb Radiances., *J. Atmos. Sci.*, *56*, 233–240, doi:10.1175/1520-0469(1999)056⟨0233:OOSAUC⟩2.0.CO;2.

Rodgers, C. D. (2000), *Inverse methods for atmospheric sounding: theory and practice*, World Scientific.

von Savigny, C., C. S. Haley, C. E. Sioris, I. C. McDade, E. J. Llewellyn, D. Degenstein, W. F. J. Evans, R. L. Gattinger, E. Griffioen, E. Kyrölä, N. D. Lloyd, J. C. McConnell, C. A. McLinden, G. Mégie, D. P. Murtagh, B. Solheim, and K. Strong (2003), Stratospheric ozone profiles retrieved from limb scattered sunlight radiance spectra measured by the OSIRIS instrument on the Odin satellite, *Geophys. Res. Lett.*, *30*, 1755, doi:10.1029/2002GL016401.

3.3 Analysis of GOMOS, SCIAMACHY and OSRIS Aerosol Records (WP–26)

This section describes the analysis of the GOMOS AerGom V1.1, SCIAMACHY V1.1 and OSIRIS V6 aerosol records in preparation of their intercomparison. The retrieval algorithms for the AerGom data is described in (Vanhellemont et al.(2011), for the SCIAMACHY data in section 3.1 and for OSIRIS in section 3.2. The results of the intercomparison of monthly zonal means from all three data sets are described in the Product Validation Report (PVR).

3.3.1 GOMOS Data

The analysis was restricted to one month of GOMOS data, June 2003. The data set used for the comparison contains about 900 valid profiles meeting the following criteria:

- The magnitude of the reference star should not be larger than 2.5
- The brightness temperature of the reference star should not be smaller than 5000K.
- The solar zenith angle should be larger than 117°.

The latitude range of these profiles is between 60°S and 30°N, albeit with sparse sampling in some latitude bands in between. The ranges between 60°S-40°S and 30°S-30°N are fairly well sampled. Within some latitude bands, aerosol extinction profiles for different reference stars were compared with each other. Several features were observed during this comparison:

- There is in general a large scatter between different GOMOS profiles of the same star below about 20-25 km. The scatter cannot be explained by just the statistical error of the measurements. Profiles with large negative extinction values below 20 km occur quite frequently.
- Oscillations along the altitude of each profile are observed whose frequency and amplitude may be related to the cutoff altitude of each profile. The largest oscillations occur for the highest cutoff altitudes.
- The cutoff altitude is related to the tangent height at which the measurement stopped because the star signal was lost, typically when a cloud obscures the star. Statistically, however, it can be seen that the cutoff altitude also increases with star magnitude.
- For altitudes above 20 km, the extinction at 350 and 550 nm seems to be relatively stable (modulo some oscillations) with values in about the expected range. The 756 nm extinction profiles exhibit systematically low and negative values between 20-30 km and strong oscillations, though.

These features point to potential problems in the Level 1 data or the algorithm and have to be investigated further. At the moment it can only be concluded that the 756 nm extinction is not usable, while the 350 and 550 nm extinction can be used above 20 km. Since the statistical error of the retrieved extinction increases when the signal of the reference star decreases, the monthly zonal averages used in the comparison are error weighted means. In latitude bins where more than one star is available, the average aerosol extinction is therefore weighted towards profiles obtained with the higher signal stars.

3.3.2 SCIAMACHY Data

In addition to the aerosol extinction profiles, the corresponding Level-1 data were also available for analysis and could be related to the data. Individual, unfiltered aerosol extinction data frequently

have extremely large and sometimes unphysical values at altitudes below about 20 km. Also in the SCIAMACHY data set the profiles oscillate between low and high values with amplitudes often related to the extinction values at low altitudes. The SCIAMACHY extinction values can be unphysically low, but never negative. An analysis of the corresponding Level-1 radiances revealed that the large extinction values and oscillations are most of the time related to clouds or other structures with a large radiative effect (i.e., thick tropospheric or low stratospheric aerosol layers, PSCs etc.). The aerosol data seem to be most affected by clouds above 10 km, that is, within the altitude range which is used for the aerosol retrieval. By applying a cloud filter, the frequency of extreme values and strong oscillations can be reduced. A measurement at a specific tangent height is positively identified as cloud free if

$$\frac{R^*(\lambda = 1550\text{nm})}{R^*(\lambda = 1670\text{nm})} > 0.7, \tag{3.21}$$

where R^* is the measured reflectance normalized to a modeled reflectance for Rayleigh scattering with a dark surface (Albedo=0). Model comparisons show, that with this cut clouds in the field of view with an optical depth larger than 0.01 can be removed with a high efficiency, while layers with high aerosol loads remain unaffected. Due to the vertical undersampling of SCIAMACHY, geometrically or optically thin clouds which mainly reside between tangent height steps may be missed or assigned to the wrong tangent height, though. Therefore, for the comparison here the SCIAMACHY profiles were required to be cloud free between 0 and 20 km. Due to the upper limit of 20 km, and also because the signal at 1670 nm is noisy at higher altitudes, PSCs are typically not excluded from the sample. Due to the filtering the average extinction values increase by 20-30% at tangent heights about 5 km above the clouds. Oscillations over the entire altitude range still remain, but with a much smaller amplitude. The RMS variance between 20-35 km is about 50% of that for the unfiltered data. Even after applying the cloud filter, a small number of profiles has unphysically large extinction values, such that in addition it is required that the maximum extinction value in a profile does not exceed 5 km^{-1}. The oscillations are introduced intrinsically by the ill constrained retrieval algorithm and cannot be completely avoided. Filtering and averaging over a large number of profiles results in realistic values that can be used for the comparison.

3.3.3 OSIRIS Data

The OSIRIS data do not contain any obvious outliers nor do they exhibit strong oscillations over altitude. Also, systematic deviations between the a.m. and p.m. data samples, distinguishable by the relative azimuth angle are typically below 20%. Most clouds and also optically thick aerosol layers which could potentially disturb the retrieval are implicitly filtered already because the signal at $1.5\mu m$ is saturated under such conditions. Signal saturation sometimes also occurs when volcanic aerosol layers are present, such that data at tangent heights below about 20 km are frequently missing after volcanic events or average values may be too low due to biased sampling. In a similar way, PSCs may also not be detected. Since PSCs are not filtered from GOMOS and SCIAMACHY data, lower extinction values in the respective latitudes and seasons are expected.

Bibliography

Filip Vanhellemont, Christine Bingen, Charles Robert: *Algorithm Theoretical Basis Document (ATBD) GOMOS AERGOM Version 1.1*, ESA Climate Change Initiative aerosol_cci document, ATBD0-AERGOM, Aerosol_cci_GOMOS_ATBD_v1.1.doc.

4 Algorithm Theoretical Baseline – Temperature

4.1 Algorithms for the Computation of Temperature Climatologies (WP–18)

Monthly mean zonal mean temperature climatologies were produced for ACE-FTS, MIPAS, and SMR following the same procedure as outlined in section 7.1 for short-lived species, in order to produce datasets on a common grid compatible the SPARC data initiative.

Monthly mean zonal mean temperature climatologies based on radio occultation (RO) data were produced as follows. CHAMP and GRACE data were obtained directly from the GFZ Helmholtz Centre in Potsdam (contacts: Jens Wickert and Torsten Schmidt). The source data consist of files of individual temperature profiles. Linear interpolation in log pressure coordinates was used to interpolate temperatures onto the pressure grid 300, 250, 200, 170, 150, 130, 115, 100, 90, 80, 70, 50, 30, 20, 15, 10, 7, 5, 3, 2, 1.5, and 1 hPa. Values at pressures below the bottom of the profile, or above the top of the profile, were omitted. Input data were also screened such that temperatures below 150 K were omitted as were temperatures above 330 K. The interpolated values were corrected for their zonal representativeness using NCEP (National Centers for Environmental Prediction) CFSR (Climate Forecast System Reanalyses) 6 hourly temperature fields on pressure surfaces as:

$$T_{corr} = T_{RO}(\theta, \phi, P, t) \times \frac{\overline{T_{CFSR}}(5^\circ, P, \text{month})}{T_{CFSR}(\theta, \phi, P, t)} \tag{4.1}$$

where

T_{corr} is the bias corrected temperature value,

T_{RO} is the radio occultation temperature measurement interpolated onto pressure P at latitude θ, longitude ϕ at time t,

$\overline{T_{CFSR}}(5^\circ, P, \text{month})$ is the NCEP-CFSR 5° zonal mean monthly mean temperature at pressure P, and

T_{CFSR} is the NCEP-CFSR temperature at the same time and location as T_{RO}.

Applying equation (4.1) corrects the radio occultation measurements for their sampling bias both in terms of geographical coverage and coverage within the month of interest. T_{corr} values were then accumulated into 5° latitude zones and monthly blocks. Averages of the data within each block were then calculated. These monthly means, together with the number of values used in each mean, are listed in the 36 (one for each 5° zone) output data files.

4.2 Algorithms for the Extension of the Upper Stratosphere Temperature Record (WP–23)

The MIPAS climatologies computed in WP-18 are used to extend the SSU temperature record in the stratosphere. As discussed in the PVR, data from the other ESA instruments (ACE-FTS and SMR), as well RO data from CHAMP, could not be used to extend the SSU record. As explained in the PVR, only the near-global mean (70S-70N) MIPAS climatologies are used to extend the SSU record.

In order to extend the SSU record, the MIPAS climatologies must first be averaged in the vertical using the SSU weighting functions, which are available at:

`ftp://ftp.star.nesdis.noaa.gov/pub/smcd/emb/mscat/data/SSU/SSU_v2.0/Weighting_Function/`

The three weighting functions that are used have peak values near 15, 5 and 2 hPa. Since the weighting functions ω are normalized to one, the weighted vertical integrals of the MIPAS zonal and monthly temperature climatologies T are given by

$$T_{\text{weighted}} = \int \omega(\ln(p)) \cdot T(\ln(p)) \, \mathrm{d}\ln(p) \tag{4.2}$$

where p denotes pressure. The integral is computed from 300 hPa to 0.1 hPa, the nominal height range of the MIPAS data. As discussed in the PVR, this results in a slight underestimate of the full integral, which extends from the surface to the top of the atmosphere. For each month of data the vertical weighting is performed at each latitude and the (area-weighted) near-global mean is computed after.

The next step is to adjust the SSU-weighted MIPAS times series so that they merge smoothly with the corresponding SSU time series. To do this the MIPAS and SSU data are first deseasonalized by performing a least squares fit to a function that includes a constant term, a linear trend and the first four harmonics of the annual cycle and then subtracting off the annual and semiannual harmonics from the original time series. The deseasonaliation is applied separately to the SSU and MIPAS datasets, using data from 1978 to 2006 for SSU and from 2002 to 2011 for MIPAS. Using the deseasonalized data, the mean difference (or offset) between MIPAS and SSU in the overlap period (2002-2006) is computed for each channel. These constant offsets, whose values are provided in the PVR, are then added to the deseasonalized MIPAS data. The last step is to add back on the annual and semi-annual harmonics. The final merged SSU and SSU-weighted MIPAS near-global mean temperature time series for the three SSU channels extends from 1978 to 2011: SSU from January 1978 to April 2006 and MIPAS from May 2006 to April 2011. The MIPAS data in the overlap period are excluded from the final data product since they were used in computing the offsets.

4.3 Algorithms for the Extension of the UT/LS Stratosphere Temperature Record (WP–24)

4.3.1 Introduction

The temperature climate data records generated in WP18 from ESA and ESA-TMP (ACE-FTS, MIPAS and SMR) missions and from radio occultation measurements (CHAMP, GRACE and TSX) were merged to create a new monthly mean temperature time series for the upper troposphere and lower stratosphere (UTLS). Differences between the instruments were modelled statistically using an offset and drift that also accounted for seasonality in the differences. The data set was validated against COSMIC radio occultation measurements (which were excluded from the original merging) as well as against the RATPAC radiosonde data set as reported in the PVR.

This UTLS data set was then vertically integrated to produce a second data set that could be used to assess the quality of the merged MSU4 and AMSU9 lower stratospheric temperature series provided by two groups — Remote Sensing Systems (RSS) (Mears and Wentz (2008)) and the University of Alabama at Huntsville (UAH) (Christy et al. (2003)). As the MSU channel 4 (hereafter MSU4) and AMSU channel 9 (hereafter AMSU9) temperature time series are representative of a single broad atmospheric layer, a weighting function appropriate for MSU4 and AMSU9 was used as the weighting functions in the vertical integration of our UTLS data set. The comparison with the merged MSU4 and AMSU9 datasets can be found in the PVR.

4.3.2 Bodeker Scientific UTLS merged temperature climate record

A new zonal mean monthly mean temperature time series for the upper troposphere and lower stratosphere (UTLS) was created from the data sets generated in WP18, viz.:

- The ACE-FTS, MIPAS and SMR temperature data sets.
- The CHAMP, GRACE and TSX radio occultation data sets.

Radio occultation measurements have been shown to be an effective climate benchmark below ∼25 km altitude. WP18 showed that of the three radio occultation data sets used in that work package, GRACE tends to be anomalous. Of CHAMP and TSX, since CHAMP provides the longer record we start the merging process with CHAMP. We then select the data set which shows the biggest temporal overlap with CHAMP. This is found to be MIPAS. At each latitude zone and pressure level differences are calculated between the CHAMP and MIPAS monthly mean temperatures. These are then modelled statistically using a model that includes an offset and drift where the offset fit coefficient is expanded in Fourier pairs to account for seasonality in the differences

$$f(t) = a_1 + a_2 t + a_3 \sin(2\pi t) + a_4 \cos(2\pi t) + a_5 \sin(4\pi t) + a_6 \cos(4\pi t). \tag{4.3}$$

The uncertainty of the difference function $f(t)$ takes into account possible correlations between the coefficients

$$\sigma_f(t)^2 = \sum_{i=1}^{6} \left(\frac{\partial f(t)}{\partial a_i} \right)^2 \cdot \sigma_{a_i}^2 + 2 \sum_{i=1}^{5} \sum_{k=i+1}^{6} \frac{\partial f(t)}{\partial a_i} \frac{\partial f(t)}{\partial a_k} \cdot \mathrm{cov}(a_i, a_k) \tag{4.4}$$

That statistical model fit is then used to correct the MIPAS data

$$T_{\mathrm{MIPAS,corr}}(t) = T_{\mathrm{MIPAS}}(t) + f(t), \tag{4.5}$$

$$\sigma_{\mathrm{MIPAS,corr}}(t) = \sqrt{\sigma_M^2(t) + \sigma_f^2(t)} \tag{4.6}$$

and merge them with the CHAMP data to create a new benchmark time series

$$T_{\mathrm{merged}} = \frac{w_{\mathrm{CHAMP}} \cdot T_{\mathrm{CHAMP}} + w_{\mathrm{MIPAS,corr}} \cdot T_{\mathrm{MIPAS,corr}}}{w_{\mathrm{CHAMP}} + w_{\mathrm{MIPAS,corr}}} \tag{4.7}$$

where the weights in the weighted average are given by $w_x = 1/\sigma_x^2$. The uncertainty in the correction applied to the MIPAS monthly means is incorporated into a new estimate of the uncertainty on the monthly mean

$$\sigma_{\mathrm{merged}} = \frac{1}{\sqrt{w_{\mathrm{CHAMP}} + w_{\mathrm{MIPAS,corr}}}} \tag{4.8}$$

The process is then repeated with the question being asked which of the remaining data sets shows the biggest temporal overlap with the merged CHAMP+MIPAS data set. This is found to be GRACE. Differences between the GRACE monthly mean temperatures and those of CHAMP and corrected MIPAS are then used as input to a new statistical model to derive corrections to be applied to the GRACE monthly means. This process is repeated, successively folding the MIPAS, GRACE, TSX, ACE-FTS and SMR into the original CHAMP data to successively extend the CHAMP data. This process is shown graphically in Figure 4.1. The inclusion of each additional data set helps to reduce the uncertainty on the final product (as long as they are appropriately corrected). We have such time series for every 5° latitude zone and on the following 17 pressure levels: 300, 250, 200, 170, 150, 130, 115, 100, 90, 80, 70, 50, 30, 20, 15, 10, 7 hPa.

4.3.3 Vertically weighted mean temperature series for comparison with MSU4+AMSU9

Our new UTLS temperature climate data record is then used to create a proxy for the merged MSU4+AMSU9 data sets. RSS provides text files of vertical weighting functions for the different MSU channels on their ftp-server based on the U.S. Standard Atmosphere. While the exact form of the weighting function depends on the temperature, humidity, and liquid water content of the atmospheric column, the representative weighting function based on the mean state of the atmosphere for MSU4 and for AMSU9 is given in the file

- `ftp://ftp.ssmi.com/msu/weighting_functions/std_atmosphere_wt_function_chan_tls.txt`

As this weighting function $\omega(p)$ is normalized to unity, the weighted means of our temperature time series are given by

$$T_{\text{weighted}} = \int \omega(\ln(p)) \cdot T(\ln(p)) \, \mathrm{d}\ln(p) \tag{4.9}$$

The uncertainty on the weighted mean is calculated similarly as a weigthed average of the measurement uncertainties

$$\sigma_{\text{weighted}} = \int \omega(\ln(p)) \cdot \sigma(\ln(p)) \, \mathrm{d}\ln(p) \tag{4.10}$$

Vertically integrated values are only considered to be valid if data from all 17 pressure levels are available. Figure 4.2 illustrates the calculation of the vertically integrated temperature for the latitude zone 35°N to 40°N in May 2002 as an example.

Bibliography

Christy, J.R., Spencer, R.W., Norris, W.B., Braswell, W.D., and Parker, D.E., Error Estimates of Version 5.0 of MSU–AMSU Bulk Atmospheric Temperatures, J. Atmos. Oceanic Technol., 20, 613-629, 2003.

Mears, C.A. and Wentz, F.J., Construction of the Remote Sensing Systems V3.2 Atmospheric Temperature Records from the MSU and AMSU Microwave Sounders, J. Atmos. Oceanic Technol., 26, 1040-1056, 2008.

4.4 Detection of cold point tropopause temperatures (WP–25)

4.4.1 Introduction

Temperature profiles from four ESA(TMP) instruments (ACE-FTS, MIPAS, SMR and GOMOS-HRTP) were used to calculate monthly mean zonal mean temperature data sets referenced with respect to the tropopause height, i.e. all profiles have been transformed to having the tropopause at $z = 0$. The tropopause height at each profile's latitude and longitude (which vary slightly with altitude) was obtained from the NCEP (National Centers for Environmental Prediction) CFSR (Climate Forecast System Reanalysis) tropopause height fields that provide 6 hourly data. Linear interpolation in time, and bilinear interpolation in space was used to extract tropopause heights at the exact latitude and longitude of the ESA(TPM) temperature profile. Temperature profiles were then interpolated onto equidistant altitude levels from -15 km to 30 km with respect to the tropopause height and were accumulated in 5° latitude zones and by year and month. After being corrected for their zonal and monthly mean representativeness using the NCEPCFSR temperature fields, monthly mean zonal mean values were calculated to derive the final data products.

4.4.2 Referencing temperature profiles to the tropopause height

4.4.2.1 Tropopause height

The NCEPCFSR data set provides the tropopause height every 6 hours on a regular $2.5° \times 2.5°$ latitude – longitude grid. To obtain the tropopause height at a certain time t, latitude θ and longitude ϕ, we first extract the tropopause height at that latitude and longitude for the times t_0 and t_1 closest to t with $t_0 < t < t_1$, where t_0 and t_1 are six hours apart. This is done by spatial bilinear interpolation within the NCEPCFSR tropopause height fields. In a second linear interpolation between t_0 and t_1, the tropopause height is obtained at time t.

4.4.2.2 Temperature profile with respect to tropopause height

The ACE-FTS, MIPAS and SMR data sets provide latitude and longitude information for each temperature profile. The tropopause height associated with each of these profiles is obtained as described above. If the tropopause height cannot be determined because any of the eight values necessary for the interpolation is missing in the NCEPCFSR tropopause data set, the temperature profile is not used in the analyses. If the tropopause height could be obtained for the temperature profile, the whole profile is shifted in altitude by subtracting the tropopause height. Temperature values are then linearly interpolated onto an equidistant altitude grid with respect to the tropopause from -15 km to 30 km and 1 km spacing. Temperatures are only interpolated onto the new altitude grid if there is at least one measurement value within 1 km distance of an analysis level.

The High Resolution Temperature Profile (HRTP) of the GOMOS data set has no explicit latitude and longitude information. Latitude and longitude can be inferred from the simultaneous GOMOS profile measurements of trace gases. We take the average latitude and longitude to determine the tropopause height for the profile and shift it as described above.

Figure 4.3 shows the effects of referencing the profiles with respect to the tropopause height. All individual profiles measured by ACE-FTS in August 2008 in the latitude zone from 35°N to 40°N are shown. Averaging the original profiles in panel (a) causes 'smearing' near the tropopause and the coldest temperature is not captured at the tropopause. A much better result is achieved in panel (b), where all profiles have been referenced to the tropopause height.

Figure 4.4 compares the mean profiles from Figure 4.3 side-by-side. When temperatures are referenced to the tropopause height, the coldest mean temperature is considerably colder than for the mean of the original profiles (by about 3 K) and appears exactly at the tropopause ($z = 0$) as expected.

4.4.2.3 The calculation of monthly means

It is essential when calculating zonal mean monthly means from point-like measurements to correct for zonal mean monthly mean representativeness. As described in more detail in the next section (Section 4.4.3), NCEPCFSR temperature fields on pressure levels were converted to altitude levels using NCEPCFSR geopotential height data, and then referenced to the tropopause height. Zonal mean monthly mean temperatures with respect to the tropopause height were then calculated in 5° latitude zones. The mean representativeness correction for each temperature measurement is then given by

$$T_{corr} = T_{orig}(\theta, \phi, z, t) \times \frac{\overline{T_{\mathrm{NCEP}}}(5°, z, \mathrm{month})}{T_{\mathrm{NCEP}}(\theta, \phi, z, t)} \tag{4.11}$$

where

T_{corr} is the bias corrected temperature,

T_{orig} is the original temperature interpolated onto height z with respect to the tropopause at latitude θ, longitude ϕ at time t,

$\overline{T_{\mathrm{NCEP}}}(5°, z, \mathrm{month})$ is the zonal mean monthly mean temperature from the NCEPCFSR model, and

T_{NCEP} is NCEPCFSR temperature at the same time and location as T_{orig}.

All temperatures in Equation (4.11) are referenced to the tropopause height. After this correction is applied, temperature measurements are averaged for each zone and month for the different instruments, respectively. These are the data sets supplied as NetCDF files and are described in the PSD.

4.4.3 Use of NCEPCFSR data

This section describes the use of NCEPCFSR data to generate data sets suitable for calculating the mean representativeness correction described in Section 4.4.2.3. First, the temperature fields were downscaled from a $0.5° \times 0.5°$ latitude – longitude grid to a $2.5° \times 2.5°$ grid since the tropopause height information is only available at that resolution. This was done by averaging cells of 5×5 points using an area-weighted average with weights $w_i = \cos(\theta)$ except at the poles were only 3×5 points were averaged.

Since NCEPCFSR temperature fields are given on pressure levels, in a second step, they were converted to altitude levels using NCEPCFSR geopotential height information. We used data from the following 18 pressure levels: 500, 450, 400, 350, 300, 250, 225, 200, 175, 150, 125, 100, 70, 50, 30, 20, 10 and 7 hPa. Once converted to altitude levels, profiles were referenced to the tropopause height and interpolated onto the same equidistant altitude levels from -15 km to 30 km and 1 km spacing as the ESA(TMP) temperature measurements. The 6 hourly data were averaged for every day giving daily values $T_{\mathrm{NCEP}}(\theta, \phi, z, t)$ for use in Equation (4.11). The monthly means $\overline{T_{\mathrm{NCEP}}}(5°, z, \mathrm{month})$ were calculated using area-weighted averages in 5° latitude zones. Values on both the upper and lower borders of the latitude zone were included, but given half their weight. For reference, the NCEPCFSR zonal mean monthly mean temperature data set is provided together with the four ESA(TMP) data sets. In the PVR, the four data sets are compared to this NCEPCFSR data set.

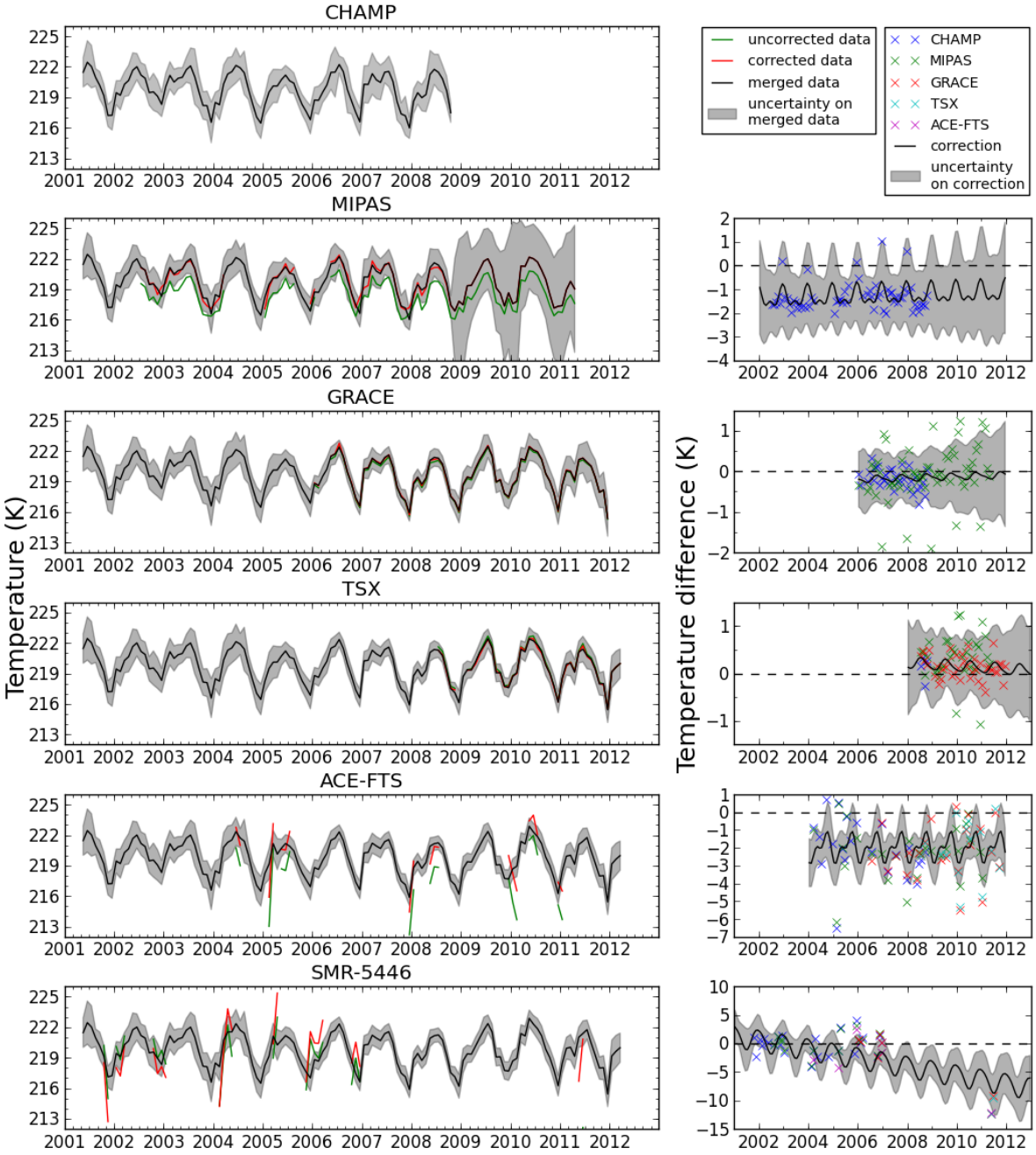

Figure 4.1: An example of the generation of the new temperature of the UTLS database, in this case showing the time series at 100 hPa and between 50°N and 55°N. The upper left panel shows the CHAMP monthly means and their 1σ uncertainties (obtained from WP18) which form the starting point for the process. The second row of panels show the uncorrected MIPAS monthly mean temperatures (green) in the leftmost panel and their differences against the CHAMP data in the rightmost panel. The regression model fit to these differences is shown as a black line in the rightmost panel together with the uncertainty on the regression model fit (grey shaded area). The regression model fit is then used to correct the MIPAS data which is then shown as the red line in the leftmost panel. The black line and grey shaded region in the leftmost panel show what a merged CHAMP and MIPAS data set would look like. The remaining data sets are then successively folded in as described in the text. The final resultant data set is displayed as a black line and grey shaded region in the bottom left panel.

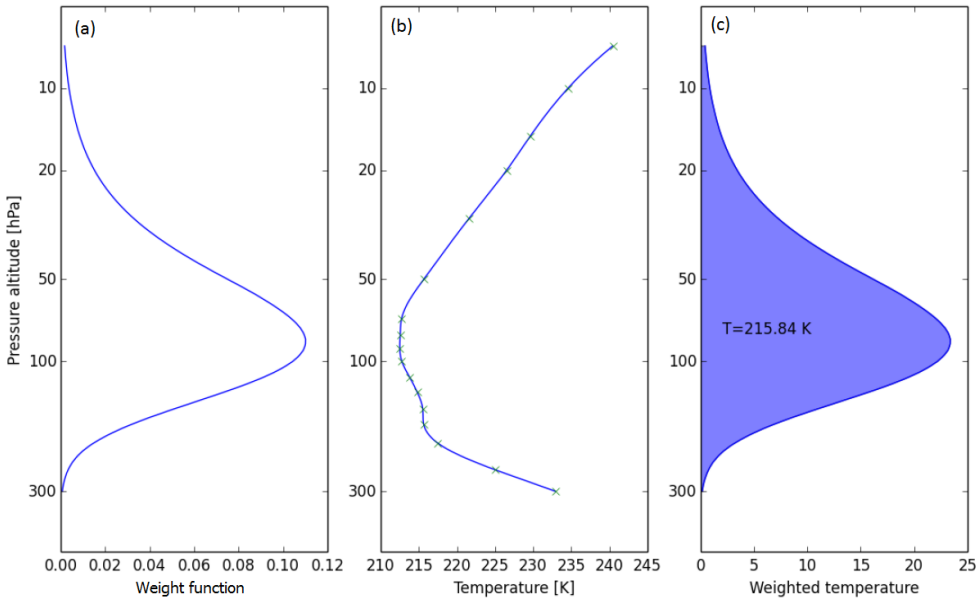

Figure 4.2: Calculation of weighted temperature in latitude zone 35°N to 40°N in May 2002. (a) Normalized weighting function of MSU4+AMSU9. (b) Temperature profile. (c) Weighted temperature function $\omega(p) \cdot T(p)$ and the integrated temperature T_{weighted} in the shaded region.

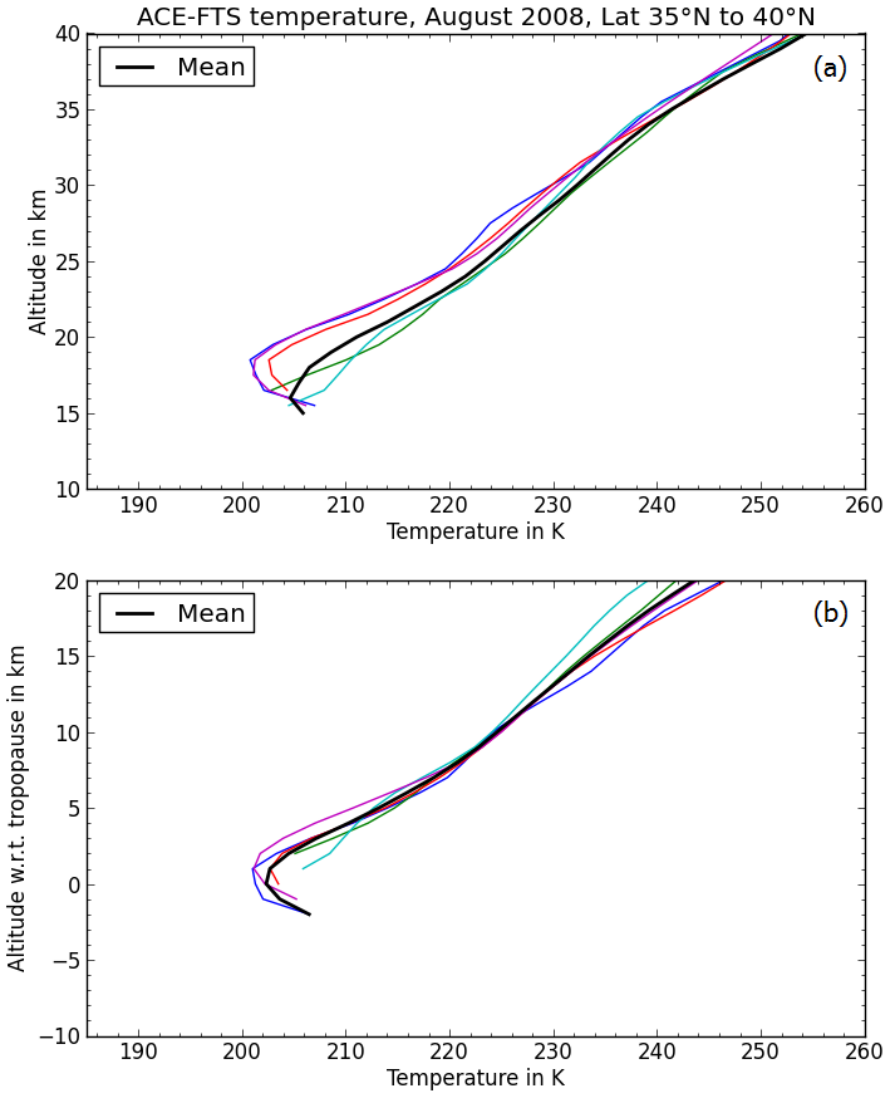

Figure 4.3: All individual ACE-FTS temperature profiles (coloured lines) in August 2008 between 35°N to 40°N and their mean (bold black line) (a) on the original altitude levels and (b) referenced to the tropopause height.

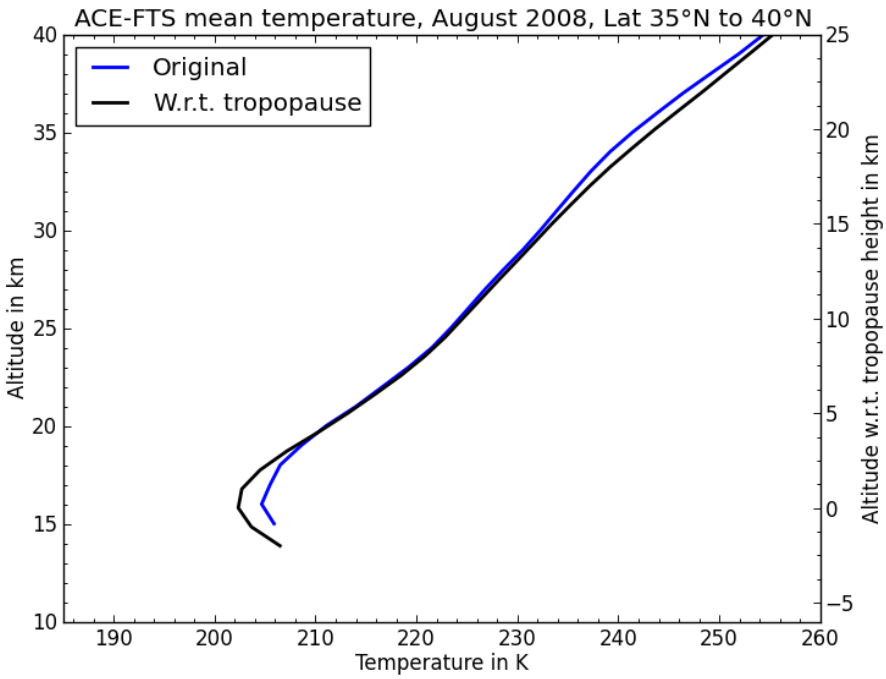

Figure 4.4: Mean temperature profile of all ACE-FTS profiles from August 2008 between 35°N to 40°N. The blue line is for the original altitude levels (z-axis on the left hand side) and the black line is referenced to the tropopause height (z-axis on the right hand side).

5 Algorithm Theoretical Baseline – Ozone

5.1 Algorithms for the GOMOS Bright Limb Ozone Analysis and Sample Processing (WP–17)

5.1.1 GOMOS bright limb processing

GOMOS (Global Ozone Monitoring by Occultation of Stars) is a spectrometer on board the European Space Agency's Envisat satellite (see Ref. Bertaux et al. (1991, 2000, 2004); Kyrölä et al. (2004); Bertaux et al. (2010); ESA (2001), and http://envisat.esa.int/dataproducts/gomos).

GOMOS is a medium resolution spectrometer. Spectrometers A1 and A2 cover the UV-visible wavelength region 248–690 nm with 1416 pixels with the spectral width 0.31 nm. The spectral resolution is 0.8 nm. The spectrometer B1 covers 755–774 nm with 420 0.045 nm wide pixels. The spectral resolution is 0.13 nm. The spectrometers B2 covers 926–954 nm with 500 0.052 nm wide pixels. The spectral resolution is 0.13 nm. The two photometers work at blue 473–527 nm and red 646–698 nm wavelengths at a frequency of 1 kHz (see Popescu and Paulsen (1999a)).

The ozone profiles obtained from the night time occultations are considered to have better than 5% accuracy at the stratosphere (Gijsel et al. , 2010; Renard et al., 2008; Meijer et al., 2004). However, the majority of the day time ozone profiles retrieved from occultations are currently of poor quality.

The GOMOS level 1b and Level 2 algorithms have been explained in Bertaux (1999); Kyrölä (1999); Kyrölä et al. (2010); Bertaux et al. (2010)). GOMOS error characterization have been discussed in Tamminen et al. (2010). GOMOS data products are discussed in Ref. Popescu and Paulsen (1999b).

In addition to the star signal, GOMOS also records the limb scattered sunlight during day time. The first experiment to retrieve ozone profiles from the limb signal was done by Taha et al. (2008). The processing presented here is based on Tukiainen et al. (2010).

5.1.2 GOMOS radiance measurements

GOMOS measures the atmosphere using three separate optical bands. The central band measures the sum of the star and the limb scattered signal, while the upper and the lower bands measure only the limb contribution. In the operational occultation retrieval, the upper/lower band radiance is removed from the central band measurement to get pure star signal, which is then used for the retrievals. This subtraction is performed for day and twilight observations but not in dark limb conditions (when the limb contribution is zero anyway).

5.1.2.1 Stray light removal

The GOMOS radiances suffer from severe stray light contamination at high tangent altitudes. The GOMOS stray light is a function of wavelength and altitude but the altitude dependence is complex and hard to model. The altitude dependence of stray light is affected by the cloud coverage below the satellite and the tangent point. There are several possible strategies to model the stray light. For the GOMOS bright limb v1.1 data we have used the simplest possible stray light estimator. We assume a constant stray light with only a spectral dependence (no altitude dependence). The stray light spectrum is calculated for each scan as a simple average

$$S(\lambda) = \frac{1}{N} \sum_{i=1}^{N} I(\lambda, i) \tag{5.1}$$

where i denotes tangent heights >100km. This constant stray light spectrum is subtracted from each altitude (radiance).

5.1.3 Inversion Method

For every measurement layer j, a least squares fit weighted by the standard deviation of the noise term is done between the model and measurement

$$\frac{\mathbf{I}(\mathrm{j},\lambda)}{\mathbf{I}_{\mathrm{ref}}(\lambda)} = \frac{\hat{\mathbf{I}}_{\mathrm{ss}}(\mathrm{j},\lambda,\rho)}{\hat{\mathbf{I}}_{\mathrm{ref}}(\lambda)}\mathbf{R} + \epsilon, \tag{5.2}$$

where $\mathbf{I}(\mathrm{j},\lambda)$ is the observed radiance and $\mathbf{I}_{\mathrm{ref}}(\lambda)$ is a reference measurement at ∼46 km. On the right hand side, $\hat{\mathbf{I}}_{\mathrm{ss}}(\mathrm{j},\lambda,\rho)$ is modeled single scattering radiance, adjusted dynamically during the fitting operations, and $\hat{\mathbf{I}}_{\mathrm{ref}}(\lambda)$ is modeled reference radiance. The second term on the right

$$\mathbf{R} = \frac{\hat{\mathbf{I}}_{\mathrm{tot}}(\mathrm{j},\lambda)}{\hat{\mathbf{I}}_{\mathrm{ss}}(\mathrm{j},\lambda)} \tag{5.3}$$

is the ratio of modeled total to single scattering radiance. This term comes from a look-up table calculated in advance with the Monte Carlo radiative transfer model Siro (Oikarinen et al., 1999). The modeled reference radiance is calculated

$$\hat{\mathbf{I}}_{\mathrm{ref}}(\lambda) = \hat{\mathbf{I}}_{\mathrm{ss}}(\lambda,\rho_{\mathrm{ecmwf}})\mathbf{R}_{\mathrm{ref}}, \tag{5.4}$$

where ρ_{ecmwf} are trace gas profiles taken from ECMWF data (air, temperature) and climatologies (O_3, NO_2, aerosols). The iterative fitting of gas densities ρ in Eq. (5.2) is done using the Levenberg-Marquardt method (Levenberg, 1944; Marquardt, 1963) minimizing the chi square function

$$\chi^2 = (\mathbf{T}_{\mathrm{obs}} - \mathbf{T}_{\mathrm{mod}})^{\mathrm{T}}\mathbf{C}^{-1}(\mathbf{T}_{\mathrm{obs}} - \mathbf{T}_{\mathrm{mod}}), \tag{5.5}$$

where $\mathbf{T}_{\mathrm{obs}}$ and $\mathbf{T}_{\mathrm{mod}}$ denote ratios of Eq. (5.2) and $\mathbf{C}$ is the diagonal error covariance matrix including variance of the measurement (ratio) error. The standard deviation of the radiance $\mathbf{I}(\mathrm{j},\lambda)$ is approximated as

$$\sigma_{\mathrm{rad}}(\mathrm{j},\lambda) = \sqrt{\mathbf{I}_{\mathrm{e}}(\mathrm{j},\lambda) + \mathbf{I}_{\mathrm{sc}}(\lambda) + \mathbf{I}_{\mathrm{dc}}(\lambda)}\mathbf{Z}(\lambda), \tag{5.6}$$

where $\mathbf{I}_{\mathrm{e}}(\mathrm{j},\lambda)$ is the uncorrected radiance as electrons, $\mathbf{I}_{\mathrm{sc}}(\lambda)$ is the approximate variance of the stray light estimate, $\mathbf{I}_{\mathrm{dc}}(\lambda)$ is the contribution from the dark charge, and $\mathbf{Z}(\lambda)$ is the radiometric sensitivity curve to convert the values into physical units. The variance of the radiance ratio $\frac{\mathbf{I}(\mathrm{j},\lambda)}{\mathbf{I}_{\mathrm{ref}}(\lambda)}$ is approximated as

$$\sigma^2_{\mathrm{ratio}}(\mathrm{j},\lambda) = \left(\frac{\sigma_{\mathrm{rad}}(\mathrm{j},\lambda)}{\mathbf{I}_{\mathrm{ref}}(\lambda)}\right)^2 + \left(\frac{\mathbf{R}(\mathrm{j},\lambda)\sigma_{\mathrm{rad}}(\mathrm{j}_{\mathrm{ref}},\lambda)}{\mathbf{I}_{\mathrm{ref}}(\lambda)}\right)^2, \tag{5.7}$$

where $\mathbf{I}_{\mathrm{ref}}(\lambda)$ is the measurement reference radiance, $\mathbf{R}(\mathrm{j},\lambda)$ is the modeled tot/ss ratio, and $\sigma_{\mathrm{rad}}(\mathrm{j}_{\mathrm{ref}},\lambda)$ is the standard deviation of the radiance at the reference altitude. Currently, no modeling error is added in the covariance matrix $\mathbf{C}$.

The atmosphere between around 60 and 20 km is "peeled" this way from top to down to get the vertical profiles of retrieved species. We retrieve O_3, aerosols and neutral air together while NO_2 is taken from a climatology and kept fixed.

5.1.3.1 Processing

The schematic presentation of the processing chain is shown in Fig. 5.2

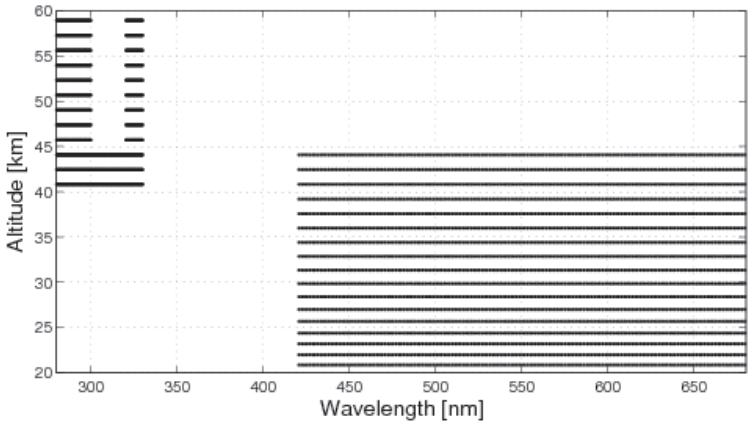

Figure 5.1: GOMOS wavelengths used in the bright limb ozone retrieval.

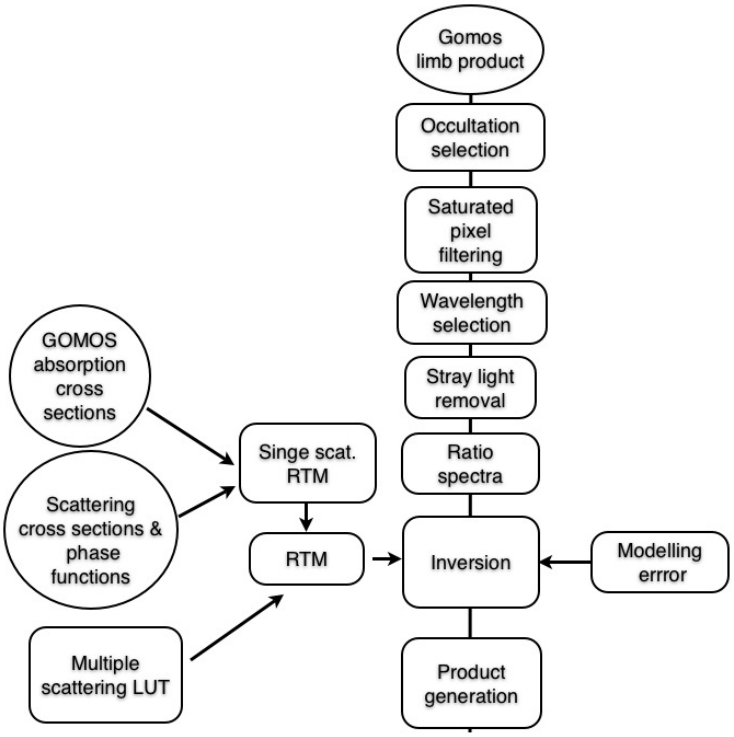

Figure 5.2: GOMOS bright limb processing

Bibliography

J. L. Bertaux. GOMOS ATBD—Level 1b. In *ESAMS99, European Symposium on Atmospheric Measurements From Space*, volume WPP-161, pages 115–123, Noordwijk, 1999. ESA.

J. L. Bertaux, G. Megie, T. Widemann, E. Chassefiere, R. Pellinen, E. Kyrölä, S. Korpela, and P. Simon. Monitoring of ozone trend by stellar occultations: The GOMOS instrument. *Adv. Space Res.*, 11(3):237–242, 1991.

J. L. Bertaux, E. Kyrölä, and T. Wehr. Stellar occultation technique for atmospheric ozone monitoring: GOMOS on Envisat. *Earth Observation Quarterly*, 67:17–20, 2000.

J. L. Bertaux, A. Hauchecorne, F. Dalaudier, C. Cot, E. Kyrölä, D. Fussen, J. Tamminen, G. W. Leppelmeier, V. Sofieva, S. Hassinen, O. Fanton d'Andon, G. Barrot, A. Mangin, B. Théodore, M. Guirlet, O. Korablev, P. Snoeij, R. Koopman, and R. Fraisse. First results on GOMOS/Envisat. *Adv. Space Res.*, 33:1029–1035, 2004.

J. L. Bertaux, E. Kyrölä, D. Fussen, A. Hauchecorne, F. Dalaudier, V. Sofieva, J. Tamminen, F. Vanhellemont, O. Fanton D'Andon, G. Barrot, A. Mangin, L. Blanot, J. C. Lebrun, K. Pérot, T. Fehr, L. Saavedra, G. W. Leppelmeier, and R. Fraisse. Global ozone monitoring by occultation of stars: an overview of GOMOS measurements on ENVISAT. *Atmospheric Chemistry & Physics*, 10:12091–12148, December 2010. doi: 10.5194/acp-10-12091-2010.

ESA. *Envisat-GOMOS, An instrument for global atmospheric ozone monitoring*, volume SP-1244. European Space Agency, 2001.

E. Kyrölä. GOMOS ATBD—Level 2. In *ESAMS99, European Symposium on Atmospheric Measurements From Space*, volume WPP-161, pages 125–137, Noordwijk, 1999. ESA.

E. Kyrölä, J. Tamminen, G. W. Leppelmeier, V. Sofieva, S. Hassinen, J.-L. Bertaux, A. Hauchecorne, F. Dalaudier, C. Cot, O. Korablev, O. Fanton d'Andon, G. Barrot, A. Mangin, B. Theodore, M. Guirlet, F. Etanchaud, P. Snoeij, R. Koopman, L. Saavedra, R. Fraisse, D. Fussen, and F. Vanhellemont. GOMOS on Envisat: An overview. *Adv. Space Res.*, 33:1020–1028, 2004.

E. Kyrölä, J. Tamminen, V. Sofieva, J. L. Bertaux, A. Hauchecorne, F. Dalaudier, D. Fussen, F. Vanhellemont, O. Fanton D'Andon, G. Barrot, M. Guirlet, A. Mangin, L. Blanot, T. Fehr, L. Saavedra de Miguel, and R. Fraisse. Retrieval of atmospheric parameters from GOMOS data. *Atmospheric Chemistry & Physics*, 10:11881–11903, December 2010. doi: 10.5194/acp-10-11881-2010.

K. Levenberg. A method for the solution of certain problems in least squares. *Quart. Appl. Math.*, 2:164–168, 1944.

D.W Marquardt. An Algorithm for Least-Squares Estimation of Nonlinear Parameters. *J. Soc. Indust. Appl. Math.*, 11:431–44, 1963.

Y. J. Meijer, D. P. J. Swart, M. Allaart, S. B. Andersen, G. Bodeker, Boyd, G. Braathena, Y. Calisesia, H. Claude, V. Dorokhov, P. von der Gathen, M. Gil, S. Godin-Beekmann, F. Goutail, G. Hansen, A. Karpetchko, P. Keckhut, H. M. Kelder, R. Koelemeijer, B. Kois, R. M. Koopman, J.-C. Lambert, T. Leblanc, I. S. McDermid, S. Pal, G. Kopp, H. Schets, R. Stubi, T. Suortti, G. Visconti, , and M. Yela. Pole-to-pole validation of ENVISAT/GOMOS ozone profiles using data from ground-based and balloon-sonde measurements. *J. Geophys. Res.*, 109(D23):art. no D23305, 2004. doi: 10.1029/2004JD004834.

L. Oikarinen, E. Sihvola, and E. Kyrölä. Multiple scattering radiance in limb-viewing geometry. *J. Geophys. Res.*, 104(D24):31,261–31,274, 1999.

A. Popescu and T. Paulsen. Gomos instrument on Envisat. In *ESAMS99, European Symposium on Atmospheric Measurements from Space*, volume WPP-161, pages 89–99. ESA, 1999a.

A. Popescu and T. Paulsen. Gomos data products. In *ESAMS99, European Symposium on Atmospheric Measurements from Space*, volume WPP-161, pages 111–114. ESA, 1999b.

J.-B. Renard, G. Berthet, C. Brogniez, V. Catoire, D. Fussen, F. Goutail, H. Oelhaf, J.-P. Pommereau, H. K. Roscoe, G. Wetzel, M. Chartier, C. Robert, J.-Y. Balois, C. Verwaerde, F. Auriol, P. François, B. Gaubicher, and P. Wursteisen. Validation of GOMOS-Envisat vertical profiles of O_3, NO_2, NO_3, and aerosol extinction using balloon-borne instruments and analysis of the retrievals. *Journal of Geophysical Research (Space Physics)*, 113(A12):A02302, February 2008. doi: 10.1029/2007JA012345.

G. Taha, G. Jaross, D. Fussen, F. Vanhellemont, E. Kyrölä, and R. D. McPeters. Ozone profile retrieval from GOMOS limb scattering measurements. *Journal of Geophysical Research (Atmospheres)*, 113(D12):23307–+, December 2008. doi: 10.1029/2007JD009409.

J. Tamminen, E. Kyrölä, V. F. Sofieva, M. Laine, J.-L. Bertaux, A. Hauchecorne, F. Dalaudier, D. Fussen, F. Vanhellemont, O. Fanton-D'Andon, G. Barrot, A. Mangin, M. Guirlet, L. Blanot, T. Fehr, L. Saavedra de Miguel, and R. Fraisse. GOMOS data characterisation and error estimation. *Atmospheric Chemistry & Physics*, 10:9505–9519, October 2010. doi: 10.5194/acp-10-9505-2010.

S. Tukiainen, S. Hassinen, A. Seppälä, H. Auvinen, E. Kyrölä, J. Tamminen, C. S. Haley, N. Lloyd, and P. T. Verronen. Description and validation of a limb scatter retrieval method for Odin/OSIRIS. *Journal of Geophysical Research (Atmospheres)*, 113(D12):4308–+, February 2008. doi: 10.1029/2007JD008591.

S. Tukiainen, E. Kyrölä, P. T. Verronen, D. Fussen, L. Blanot, G. Barrot, A. Hauchecorne, and N. Lloyd. Retrieval of ozone profiles from GOMOS limb scattered measurements. *Atmospheric Measurement Techniques Discussions*, 3:4355–4382, October 2010. doi: 10.5194/amtd-3-4355-2010.

J. A. E. van Gijsel, D. P. J. Swart, J.-L. Baray, H. Bencherif, H. Claude, T. Fehr, S. Godin-Beekmann, G. H. Hansen, P. Keckhut, T. Leblanc, I. S. McDermid, Y. J. Meijer, H. Nakane, E. J. Quel, K. Stebel, W. Steinbrecht, K. B. Strawbridge, B. I. Tatarov, and E. A. Wolfram. GOMOS ozone profile validation using ground-based and balloon sonde measurements. *Atmospheric Chemistry & Physics Discussions*, 10:8515–8551, 2010.

5.2 Algorithms for Merging Vertical Ozone Profile Measurements – Bodeker Scientific approach (WP–22)

5.2.1 Introduction

Version 7.00 SAGE (Stratospheric Aerosol and Gas Experiment) II and version IPF 6.01 GOMOS (Global Ozone Monitoring by Occultation of Stars) ozone profiles have been merged to create a near-global, vertically resolved ozone database covering the period October 1984 to April 2012. The GOMOS data are corrected for any systematic bias against SAGE II. The biases were derived independently for each 1 km spaced altitude level by statistically modelling both SAGE II and GOMOS measurements directly in the overlap period from April 2002 to August 2005 and taking the difference between those two models. Because the overlap period is relatively short, biases were only allowed to depend on season and latitude; no long-term time-dependence was considered. Above ∼2 hPa, the diurnal cycle in ozone can result in large differences in ozone mixing ratios between two spatial collocated measurements that are just a little offset in time. To circumvent the problems associated with merging the data sets above ∼2 hPa, the SAGE II and GOMOS data were therefore normalized

to a nominal 90° SZA (Solar Zenith Angle) based on scaling factors derived from high resolution ozone fields obtained from a chemistry-climate model simulation. Corrected GOMOS and SAGE II measurements were accumulated in 5° latitude zones and by year and month. After being corrected for their zonal and monthly mean representativeness based on the temporal and spatial morphology of total column ozone fields, monthly mean zonal mean values were calculated to derive the final data product. The validation of this new database is detailed in the SPIN Product Validation Report (PVR) where it is compared against the Bodeker Scientific vertically resolved ozone database Bodeker et al. (2013), vertically integrated profiles are compared with an independent total column ozone data set, and through a comparison with a similar database developed by the Finnish Meteorological Institute (FMI).

5.2.2 SAGE II version 7.00

Version 7.00 SAGE II data Damadeo et al. (2013), spanning the period October 1984 to August 2005 were provided by J.M. Zawodny (NASA; personal communication) but may also be obtained directly from `https://eosweb.larc.nasa.gov/project/sage2/sage2table`. The data were converted to the BDBP format Hassler et al. (2008) and the same screening procedures as applied in Hassler et al. (2008) were applied to the version 7.00 data. A number of improvements over the earlier version 6.20 data have been made including:

- The use of the same temperature-dependent ozone absorption cross-sections as used in SCIAMACHY (Scanning Imaging Absorption Spectrometer for Atmospheric CHartographY) retrievals Bogumil et al. (2003). The use of the new spectral data results in slightly decreased ozone densities typically on the order of 1-2%.
- The MERRA (Modern-Era Retrospective Analysis for Research and Applications) reanalysis was used to provide a single consistent meteorological data set to higher altitudes over the lifetime of all SAGE instruments. The MERRA data set reduces the neutral density at higher altitudes reducing the extinction contributions from Rayleigh scattering.
- The Twomey-Chahine retrieval method was replaced with a simple onion-peeling technique for inversion of slant-path optical depths. The use of the Twomey-Chahine algorithm introduced biases in previous versions of the SAGE data e.g. it would not allow negative values and therefore introduced a positive bias in regions of the density (extinction) profile where the signal to noise ratio was small, typically at the higher altitude end of the retrieved profile. It also systematically approached the solution from one direction and stopped once the tolerance criterion was met, producing another form of bias as a result. Its use introduced discontinuities in the profile when the slant path extinction fell below a preset value and vertical smoothing was activated.
- The EOS Toolkit routines were adopted for ephemeris calculations for more consistent pointing information. The EOS Toolkit corrects a long standing error in the solar ephemeris which resulted in a quasi-random error in the altitude registration of individual occultation events.
- A number of new transmission algorithms were adopted from SAGE III v4.00. One of the several transmission algorithm changes resulted in the slant path extinction profiles having a uniform 1 km vertical resolution. Previous versions tended towards higher vertical resolution with the possibility of aliasing effects in the 0.5 km gridded data. This 1 km resolution is now consistent with the 0.5 km gridding of the retrieved species profiles.
- The water vapour extinction in the 600 nm channel due to uncertainty in the H_2O spectroscopy in this spectral band is no longer removed.
- The estimate of the water vapour channel filter location drift has been updated which results in better agreement with more modern datasets.

5.2.3 GOMOS version IPF 6.01

The GOMOS instrument and retrieval is detailed in Bertaux et al. (2010). The following web pages indicate where the version 6.01 GOMOS data were sourced and the tools used to process them:

- `ftp://gomo2usr:gomo2usr@eoa-dp.eo.esa.int` for the data files.
- `http://www.stcorp.nl/beat/` for the BEAT software used to extract the data from the files.
- `http://www.stcorp.nl/beat/documentation/beatl2-data/records/GOMOS_NL_L2.html` for instructions on how to use the BEAT software.
- `http://earth.eo.esa.int/pcs/envisat/gomos/documentation/RMF_0117_GOM_NL__2P_Disclaimers.pdf` for the GOMOS Level 2 Product Quality Readme File.

The GOMOS data extend from 15 April 2002 to 6 April 2012. The data were converted to the BDBP format and the screening procedures defined in Section 2.51 of the GOMOS Level 2 Product Quality Readme File (see URL above) were applied. Ozone, pressure and temperature were interpolated onto a geopotential height grid between 10 and 70 km. At 10 km geometric altitude, it was assumed that the geopotential height is 10 km.

5.2.4 Diurnal cycle corrections applied to SAGE II and GOMOS

SAGE II and GOMOS measure at different local solar time. In the upper stratosphere and mesosphere there is a large diurnal cycle in ozone resulting from Chapman photochemistry. In this region there may be large differences between SAGE II and GOMOS measurements that in no way are representative of biases between the measurement systems but rather result from the measurements being made on different parts of the diurnal cycle in ozone. To correct for these effects, both the GOME and SAGE II databases were normalized to ozone values representative of a measurement made at 90° solar zenith angle (SZA). First, high temporal resolution (6 hourly) and spatial resolution ($\sim$1.875° latitude, 2.5° longitude) ozone mixing ratio fields on 66 pressure levels extending from 992.6 hPa to 5.96×10^{-6} hPa were extracted from a 3 year and 4 month simulation of the WACCM (Whole Atmosphere Community Climate Model) coupled chemistry-climate model. At each latitude, longitude, pressure and date for which ozone mixing ratios were available, the 4 values from the 6 hourly fields were extracted and plotted as a function of SZA. Second order polynomials were fitted to these quadruples of ozone mixing ratio and the value at 90° SZA extracted. All 4 values in the quadruple are then divided by this 90° SZA value to obtain ratios. These ratios were then accumulated into 10° latitude zone and 90° longitude zone mean climatologies. One example of such a climatology is shown in Figure 5.3.

Similar climatologies are available for every 90° longitude zone, every 10° latitude zone, and for every month of the year. The SAGE II and GOMOS values in the BDBP database were all normalized to 90° SZA using the ratios from these climatologies.

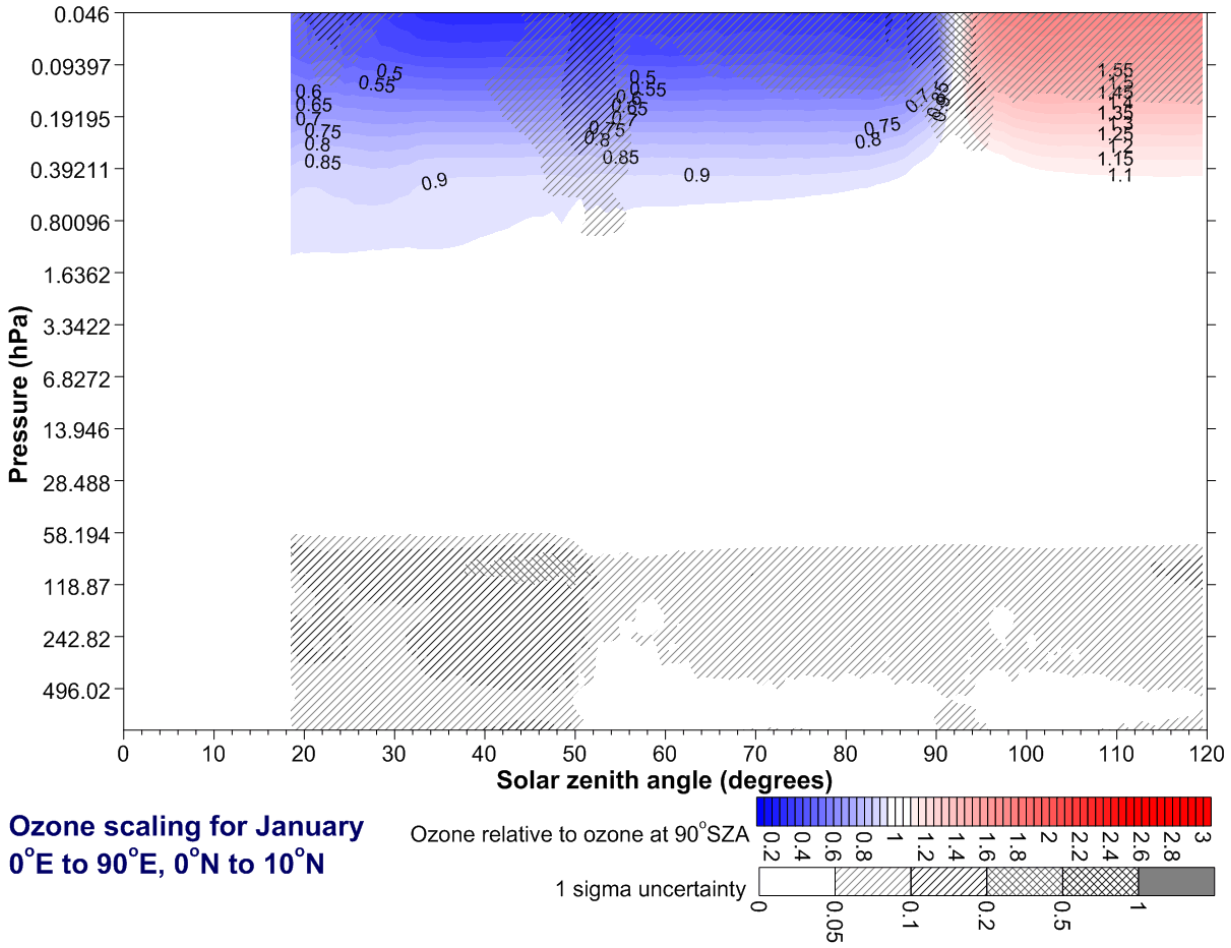

Figure 5.3: The ratio of ozone at each SZA and pressure to the ozone mixing ratio at 90° SZA using the colour scale shown along the bottom. Regions are hatched according the 1σ uncertainty on the values using the hatching scheme also shown along the bottom. As denoted on the plot, this is the climatology for 0°E to 90°E, 0°N to 10°N and for the month of January.

5.2.5 Determining SAGE II-GOMOS systematic biases

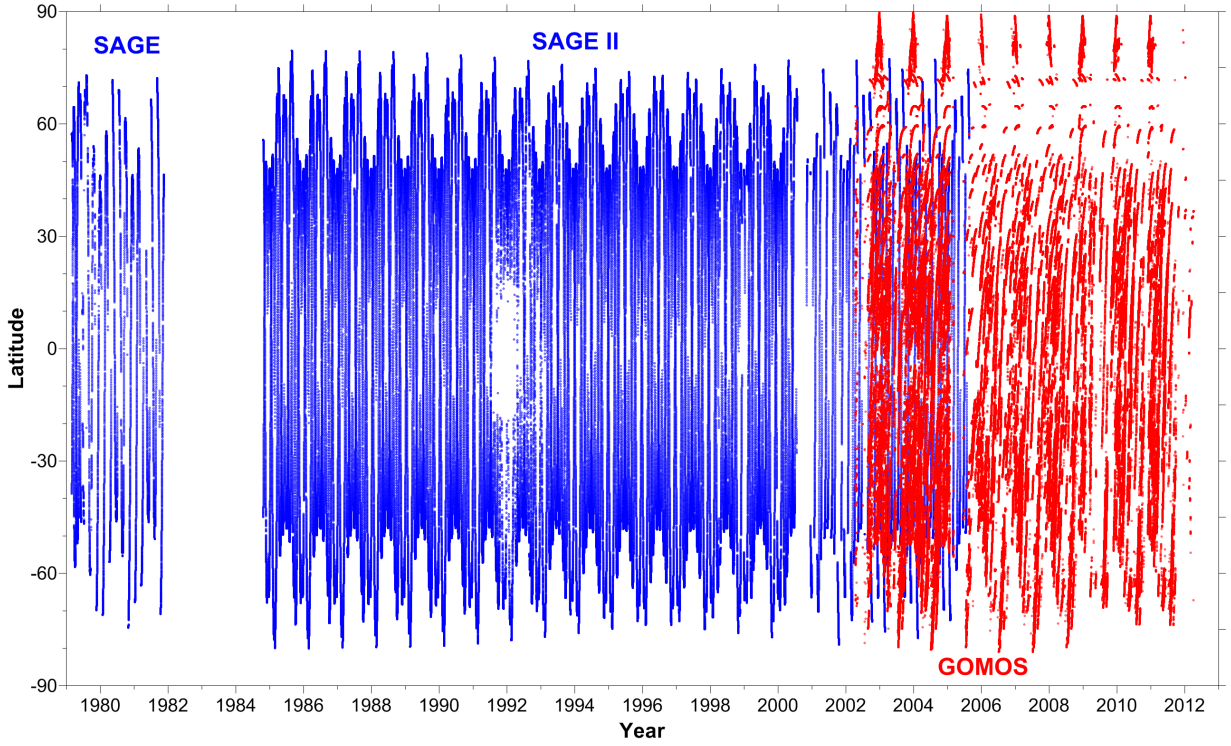

Figure 5.4: The locations in latitude and time of the SAGE and SAGE II measurements (blue) and GOMOS measurements (red) at the 20 km altitude level.

When considering the timing and location of SAGE II and GOMOS measurements (see Figure 5.4) it is clear that two challenges need to be overcome, viz.:

1. The period of overlap between the SAGE II and GOMOS data is a little over 3 years, extending from the start of GOMOS measurements in April 2002 to the end of SAGE II measurements in August 2005. Corrections derived during that overlap period need to be applied to GOMOS measurements all the way to the end of the GOMOS IPF 6.01 database in April 2012.

2. GOMOS measurements extend to higher latitudes than SAGE II, particularly in the northern hemisphere. Corrections derived at lower latitudes need to be projected to these higher latitudes.

Three different methods were explored to determine the systematic biases between the SAGE II and GOMOS measurements on each of the altitude levels (10 km to 69 km; 1 km spacing). In the first method, based on the methodology of Lary and Lait (2006), probability distribution functions (PDFs) of all available SAGE II and GOMOS measurements in some latitude zone and calendar month are compared and the bias is determined from that comparison. In the second method, coincidences between individual SAGE II and GOMOS measurements, within predefined coincidence criteria, are examined and the biases are determined from the differences between those coincident measurements. In the third method, which was that used for the final product, both SAGE II and GOMOS measurements are independently modelled in the overlap period and the bias is taken as the difference between those two models.

The first method suffers from lack of data (in particular SAGE II measurements) for certain months and zones. Relatively large latitude zones of 30° were required to derive meaningful biases. The second method, using coincidence criteria, discards the vast majority of measurements from both instruments as few data meet the requirements for detecting coincidences. The main advantage of using the third

method, i.e. statistically modelling the fields and then subtracting the modelled fields is that all available measurements are used to derive the corrections for all months and latitude zones. It does not matter if there are no data available from either instrument, or there are no coincidences between the two instruments, for certain time periods or latitude zones.

The first two methods are described in the appendix (Sections 5.2.8.1 and 5.2.8.2) while the latter method is described in this section.

Instead of modelling the difference field using only coincident SAGE II and GOMOS measurements, SAGE II and GOMOS ozone number densities were statistically modelled based on measurements available during the overlap period from 15 April 2002 to 22 August 2005. After applying the diurnal cycle correction described in Section 5.2.4, both SAGE II and GOMOS ozone number densities were individually modelled. Because of the relatively short period of overlap between SAGE II and GOMOS (∼3 years) it was felt that it would not be appropriate to determine a drift between SAGE II and GOMOS over this 3 year period and to then project that drift forward to the end of the GOMOS period in April 2012. Therefore, a regression model was used, consisting only of a constant term which was then expanded in Fourier pairs to account for seasonality and in Legendre polynomials to account for possible latitudinal structure

$$f(\theta,t) = c + \sum_{n=1}^{n_F} \sum_{m=1}^{n_L-1} \left(a_{nm}\sin(2n\pi t) + b_{nm}\cos(2n\pi t)\right) L_m(\cos\theta), \tag{5.8}$$

where θ is the co-latitude in radians, time t is measured in decimal years and L_m is the Legendre polynomial of degree m.

It was found that $n_F = 2$ Fourier pairs and $n_L = 9$ Legendre polynomials (including $L_0(x) = 1$) were optimal in the region between 25 and 49 km, and $n_F = 3$ Fourier pairs and $n_L = 7$ Legendre polynomials in the 10-15 km and 50-69 km regions. As GOMOS measurements extend further poleward than SAGE II measurements, to avoid arbitrary differences in modelled fields in regions where there were only GOMOS measurements, but no SAGE II measurements, SAGE II measurements were supplemented with GOMOS measurements poleward of 50° N and 50° S if there were no SAGE measurements in that month and 5° latitude zone. This also causes the modelled differences to tend to zero (but not exactly zero because the regression model is somewhat stiff in latitude) at high latitudes, which is desirable.

As the least-square fitting routine places a higher weight on measurements with small uncertainties, it was found that ozone measurements close to zero with small absolute uncertainties could bias the fit towards zero. To avoid this undue bias, the uncertainty of any measurement was limited to a minimum of 10% of the average uncertainty of all measurements of the instrument at a particular altitude level. Especially GOMOS measurements close to zero (that can often be negative) seemed to have unphysically small absolute measurement errors, and we believe that limiting the measurement uncertainty in this way better reflects the true physical limitations of the instrument.

5.2.6 Applying the corrections to GOMOS

GOMOS data were corrected using the difference between the two regression fitted ozone fields for SAGE II and GOMOS. The correction is only applied to GOMOS values if the modelled difference diff between SAGE II and GOMOS is statistically significant based on its t-value calculated as $\mathrm{diff}/\sigma_{\mathrm{diff}}$ where σ_{diff} is the uncertainty on the modelled difference. Where the t-value > 2, diff is applied to correct the GOMOS measurement. Where the t-value < 1, no correction is applied to the GOMOS value. For t-values between 1 and 2 a linear scaling is applied to diff before it is used to correct the GOMOS measurements. This ensures that the GOMOS data are only corrected when statistical confidence in the correction is high. The uncertainty on GOMOS measurements is adjusted with $\sigma_{\mathrm{GOMOS,corr}} = \sqrt{\sigma^2_{\mathrm{GOMOS}} + \sigma^2_{\mathrm{diff}}}$.

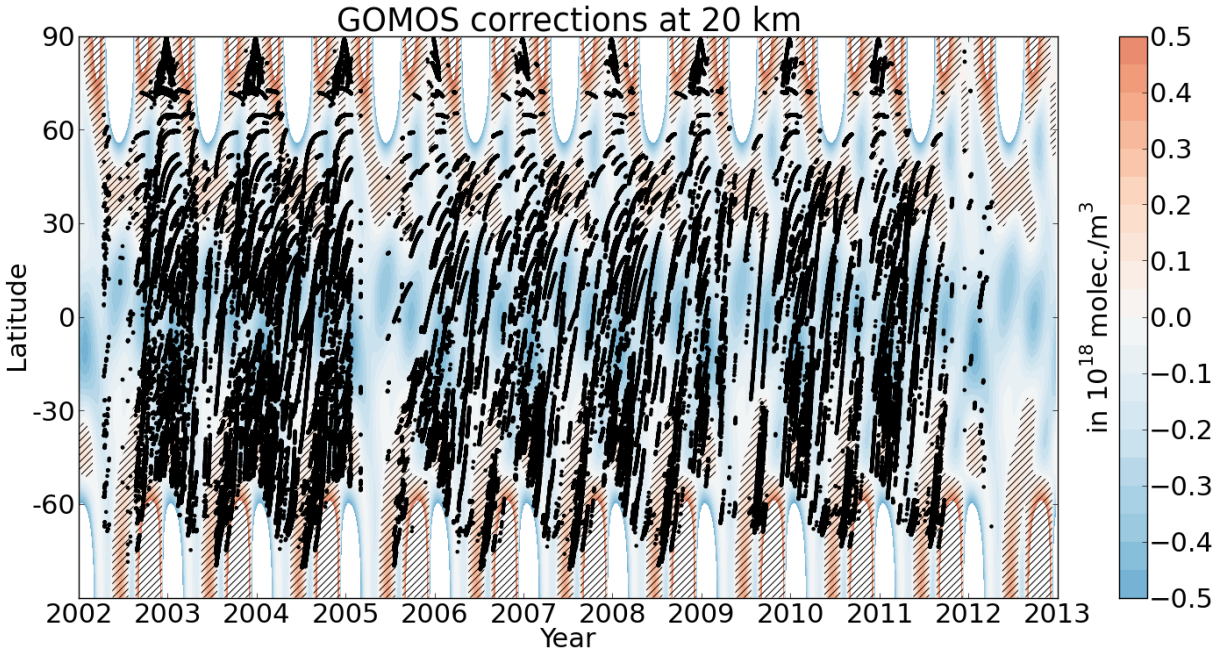

Figure 5.5: The calculated GOMOS corrections ($n_F = 3$, $n_L = 7$) at 20 km altitude are shown in colour. The black dots show the locations of the GOMOS measurements which were then corrected. Hatched regions show where the correction is not statistically significant at the 1σ level.

Figure 5.5 shows an example of the GOMOS correction applied at 20 km altitude. Note that the correction is the same for every year, but seasonal and latitudinal dependencies within a year are accounted for. In blue regions, GOMOS values were too high compared to SAGE II, and are corrected downwards. In red regions, GOMOS values were too low. Corrections close to the poles are mostly statistically insignificant.

5.2.7 The calculation of monthly means

5.2.7.1 Zonal and monthly mean representativeness corrections

It is essential when calculating monthly mean zonal mean ozone values from point-like measurements such as those from SAGE II and GOMOS, to correct for zonal mean monthly mean representativeness. For example, if it so happens that there are more measurements towards the beginning of the month than towards the end of the month, and ozone is decreasing through the month, then the calculation of the monthly mean will be biased high. Similarly, if more ozone measurements are available towards the north of the zone and there is a strong negative north-south gradient in ozone across the zone, the zonal mean will be biased high. Two methods were investigated to correct both SAGE II and GOMOS ozone values for their zonal mean monthly mean representativeness. The first one uses total column ozone fields from the Bodeker Scientific combined total column ozone (TCO) database (see `http://www.bodekerscientific.com/data/total-column-ozone`). However, this approach assumes that the morphology of the total column ozone field is a good estimate of the ozone field at all levels in the atmosphere which might not be the case, especially at higher altitude levels. Thus, in a second approach, a statistical model was fitted to the available ozone data and then used to calculate the zonal mean monthly mean sampling bias correction (see Appendix 5.2.8.3), but problems resulting in large correction factors in regions with low ozone number densities precluded the use of this method and so the total column ozone method, described below, was used to calculate the sampling bias corrections.

Individual measurements were corrected for their zonal mean monthly mean representativeness using TCO fields as follows:

$$O_{3,corr} = O_{3,orig}(\theta, \phi, z, t) \times \frac{\overline{O_{3,TCO}}(5^\circ, \text{month})}{O_{3,TCO}(\theta, \phi, t)} \tag{5.9}$$

where

$O_{3,corr}$ is the bias corrected ozone number density,

$O_{3,orig}$ is the original ozone number density value interpolated onto geopotential height z at latitude θ, longitude ϕ at time t,

$\overline{O_{3,TCO}}(5^\circ, \text{month})$ is the Bodeker Scientific 5° zonal mean monthly mean total column ozone, and

$O_{3,TCO}$ is the Bodeker Scientific total column ozone at the same time and location as $O_{3,orig}$.

Daily and monthly mean total column ozone fields were obtained from the Bodeker Scientific combined total column ozone database (Bodeker et al. (2005)). Applying equation (5.9) corrects the ozone measurements for their sampling bias both in terms of geographical coverage and coverage within the month of interest. In no way does equation (5.9) normalize the ozone number density to match the total column ozone when vertically integrated. It simply assumes that the ratio between the spot ozone measurement and the zonal mean monthly mean value at that altitude is the same as the ratio between a spot total column ozone measurement at the same latitude and longitude and the monthly mean zonal mean total column ozone. An example of this bias correction is shown in Figure 5.6. The correction results in a narrower PDF whose peak is better representative of the true monthly mean. Such corrections were applied to both the SAGE II and the GOMOS measurements before the monthly means were calculated.

5.2.7.2 Construction of the SAGE II-GOMOS merged data product

Once GOMOS is corrected with respect to SAGE II, individual measurements from both instruments are comparable and can be combined in the calculation of zonal mean monthly means. To identify outliers, the residuals of all measurements relative to the model using full spherical harmonics described in Appendix 5.2.8.3 were averaged by latitudinal zone and month (irrespective of year), and the

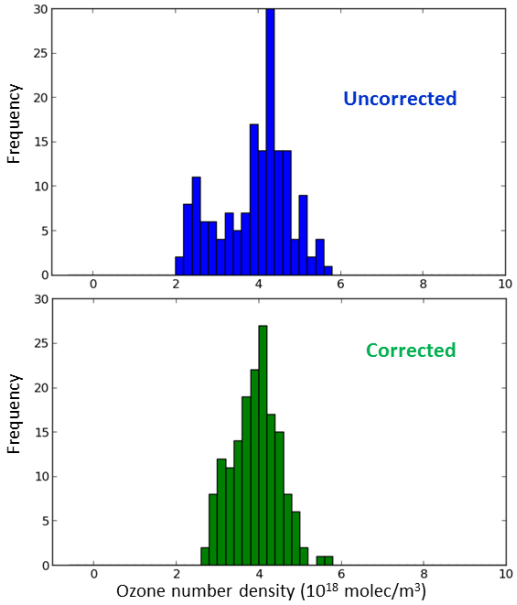

Figure 5.6: Probability distribution functions of GOMOS data at 25 km between 55° S and 50° S in the month of August 2002 where no corrections have been applied (upper panel) and where the measurements have been corrected for their monthly mean zonal mean representativeness.

standard deviation of the residuals σ_{res} was calculated. Measurements that were more than $3\sigma_{\text{res}}$ away from the modelled value were identified as outliers and discarded. Each measurement was corrected for its mean representativeness using Equation (5.11). Zonal mean monthly means were calculated as weighted means taking into account the uncertainty on each measurement using weights $w_i = 1/\sigma_i^2$. As uncertainties of SAGE II measurements are typically smaller than of GOMOS, this will give SAGE II measurements more weight in the overlap period. The uncertainty on the weighted mean is given by

$$\sigma_{\bar{x}} = \sqrt{\frac{1}{\sum_{i=1}^{n} w_i} \times \frac{1}{(n-1)} \sum_{i=1}^{n} w_i (x_i - \bar{x})^2}. \tag{5.10}$$

If there was only one measurement in a zone for a certain month, the uncertainty on that measurement was used.

Figure 5.7 illustrates the effects of the correction to GOMOS on the weighted zonal means. It shows weighted zonal means of SAGE II (black dots), the original GOMOS data (green dots) and the GOMOS data corrected for systematic biases relative to SAGE II (red dots) in the 0°N to 5°N zone at (a) 16 km and (b) 20 km. All three time series were corrected for their zonal mean monthly mean representativeness. It can be clearly seen that the corrected GOMOS data are much better aligned with the SAGE II data. Furthermore, the overall variation in the GOMOS data is reduced as can be seen particularly well in Figure 5.7 (b). This in turn reduces the uncertainty on the zonal means. It should be emphasized that the weighted means shown in Figure 5.7 were only calculated separately for SAGE II and GOMOS for illustrative purposes. For the final product, the weighted means were calculated from both SAGE II and corrected GOMOS data together if measurements from both instruments were available.

Any negative zonal mean monthly means were removed as they are unphysical. Negative values were occasionally found in zones with very few measurements, especially at low altitudes where neither SAGE II nor GOMOS are very reliable. However, it is not recommended to remove all negative values before calculating averages as this might introduce an artificial high bias. The final data set also provides counts of how many measurements were used in the calculation of the zonal mean monthly

means. Obviously, averages with fewer measurements might be less reliable, and users of the database will be able to use their own judgment on which values to use based on the counts of measurements averaged.

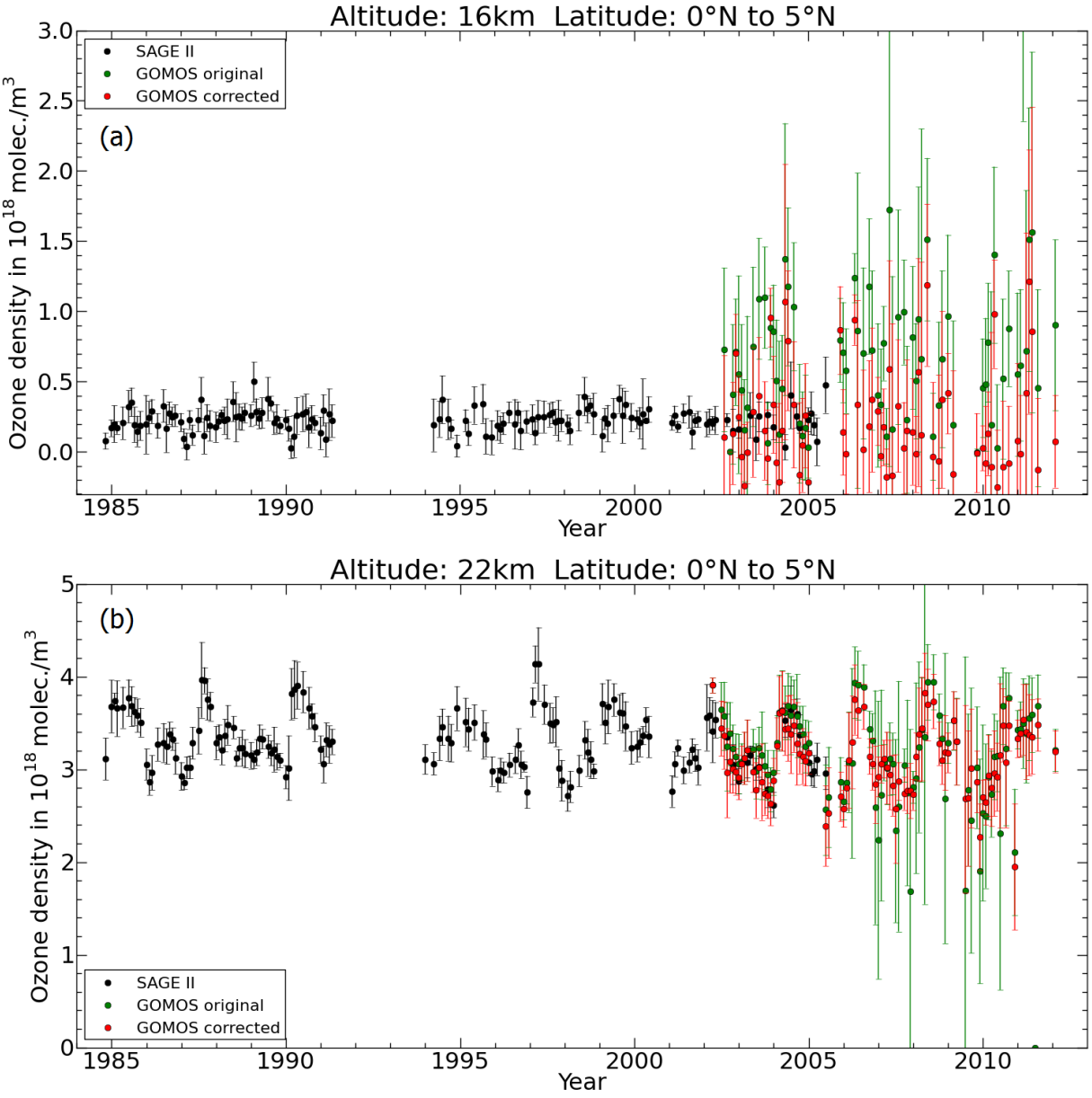

Figure 5.7: Zonal mean monthly mean ozone number densities for SAGE-II and GOMOS in 0°N to 5°N zone. All measurements were first corrected for their zonal mean monthly mean representativeness. (a) At 16 km altitude. (b) At 22 km altitude.

5.2.8 Appendix: Merging SAGE II and GOMOS vertical ozone profile measurements

5.2.8.1 Bias corrections based on PDFs

To obtain a systematic bias correction between SAGE II and GOMOS, probability distribution functions (PDFs) of ozone measurements from SAGE II and GOMOS are compared at each altitude level, in each 30° latitude zone, and in each calendar month. Before generating the PDFs, the individual measurements were corrected for their zonal mean monthly mean representativeness using Equation (5.9). An example of SAGE II and GOMOS PDFs is shown in Figure 5.8.

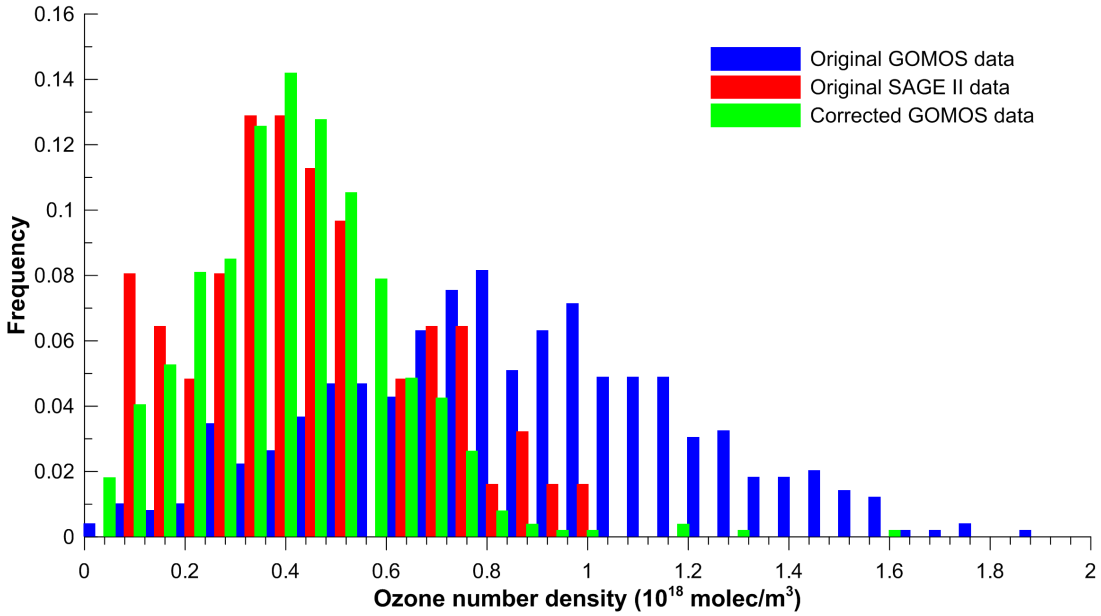

Figure 5.8: The PDF of the SAGE II (red), uncorrected GOMOS (blue) and corrected GOMOS (green) ozone measurements in January at 15 km between 0°S and 30°S.

Means of the uncorrected SAGE II and GOMOS PDFs are calculated and used to correct the GOMOS data as follows:

$$GOMOS_{corr} = GOMOS_{orig} \times \frac{\overline{SAGEII} - \overline{GOMOS}}{\overline{GOMOS}} \tag{5.11}$$

where overbars denote the mean of the PDF.

There are two particular challenges associated with this method, viz.

1. There are few SAGE II measurements above ∼60 km and few SAGE II measurements below ∼15 km.

2. In some zones (e.g. 0°S to 30°S) there are no SAGE II measurements in some months (e.g. February).

GOMOS on the other hand has typically more than 200 measurements in each calendar month at each altitude level between 10 and 70 km. In response to these limitations single correction factors were derived across all months in the upper atmosphere and poleward of 60°N. In cases where no corrections could be derived for some month e.g. February between 0°S and 30°S, the corrections derived in January and March were averaged.

An indication of the effect of these corrections is shown in Figure 5.9.

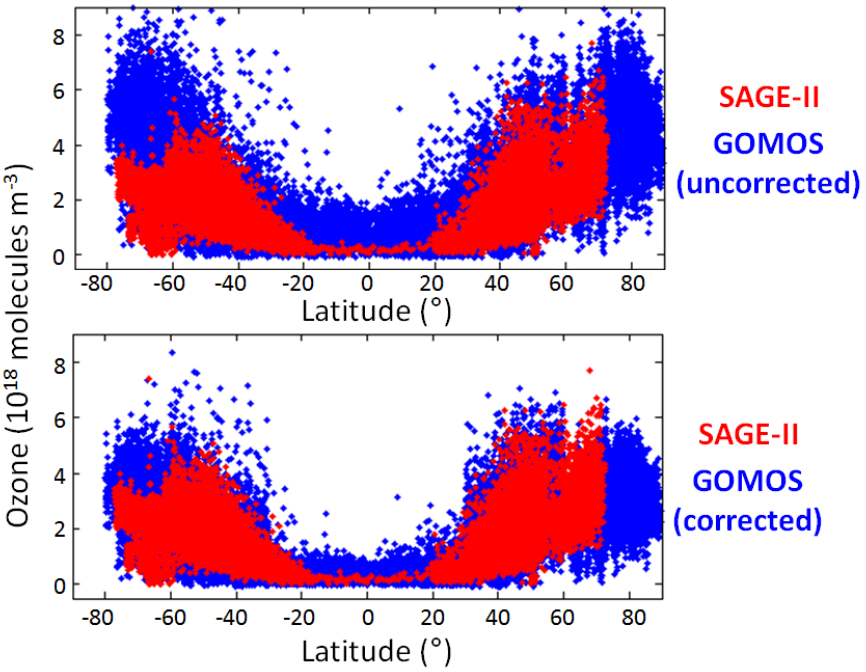

Figure 5.9: (upper panel) SAGE II (red) and uncorrected GOMOS (blue) ozone measurements at 15 km altitude; (lower panel) SAGE II and corrected GOMOS measurements at 15 km altitude.

5.2.8.2 Bias corrections based on coincidences

In this part of the study, corrections for the GOMOS data are derived by locating spatial and temporal coincidences between SAGE II and GOMOS measurements where the coincidences are defined by Δlatitude, Δlongitude and Δtime limits for data on the same altitude level.

Optimizing coincidence criteria The choice of what would be termed a coincidence between a SAGE II and a GOMOS measurement is somewhat arbitrary. If the coincidence criteria are too tight then too few coincidences would be identified and a robust determination of the systematic biases between the SAGE II and GOMOS measurements would not be possible. On the other hand, if the coincidence criteria are set too loose then differences between apparently coincident ozone measurements may result from real geophysical differences in the ozone measurements rather than inter-instrument biases. To find the best possible criteria for identifying SAGE II and GOMOS measurements as being coincident, a wide range of criteria was explored:

- Δtime values of 2, 4, 6, 12, 24 and 48 hours were explored.
- Δlatitude values of 1°, 2°, 3°, and 5° were explored.
- Δlongitude values of 10°, 15°, 20°, 30°, 45°, and 60° were explored.

We considered how often we would have coincidences in 3 month periods, in 30° latitude zones, under every possible combination of coincidence criteria. These metrics were averaged over the 31 altitudes levels between 20 km and 50 km. For example, choosing a 48 hours, 5° latitude and 60° longitude criterion would give at least one SAGE II/GOMOS coincidence in 55.8% of the 3 month, 30° latitude cells averaged over 20 to 50 km. The stricter criterion of 12 hours, 2° latitude and 10° longitude gave a coincidence in 50.4% of the cells and so these are the criteria that were used to define SAGE

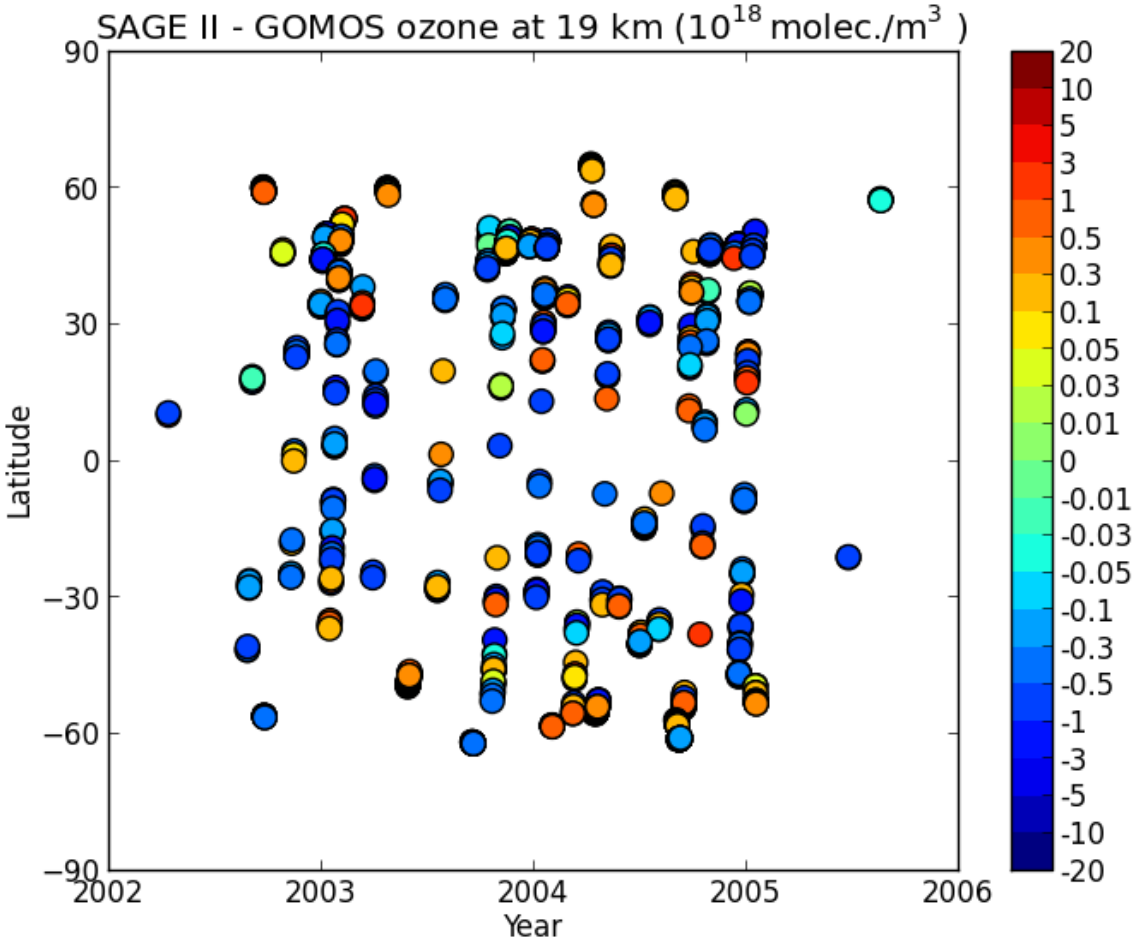

Figure 5.10: An example SAGE II – GOMOS ozone difference field at 19 km altitude.

II/GOMOS coincidences in this study. An example SAGE II – GOMOS difference field is shown in Figure 5.10.

Modelling the coincident difference field The differences were described by a statistical model that considers a single offset which is expanded in Fourier pairs to account for possible seasonality in the differences and in Legendre polynomials to account for possible latitudinal structure in the differences as in Equation 5.8. The statistical model for describing the difference field then requires selection of the number of Fourier pairs and the number of Legendre polynomials in which to expand the offset value. It was found that there was little systematic seasonality in the difference fields (which was corroborated by the PDF approach for determining systematic biases between the SAGE II and GOMOS data) and so the number of Fourier pairs was set to zero. Five Legendre polynomials were found to be sufficient to describe the meridional structure in the difference fields without the danger of over-fitting. A goal was to maximize the area over which modelled differences would be statistically significantly different from zero. At each level, SAGE II–GOMOS differences from that level, as well as the levels above and below, were passed to the statistical regression model under the assumption that the structure of the differences would be similar, or at the very least change linearly, across the three levels. The model was then used to correct the GOMOS measurements and the uncertainty on the correction was incorporated into a new estimate of the measurement uncertainty.

5.2.8.3 Zonal mean monthly mean representativeness corrections

Rather than using total column ozone data to derive the required monthly mean zonal mean representativeness corrections as described in Section 5.2.7.1, it might be considered better to derive these corrections from the data themselves. To that end we have explored a statistical model that captures the long-term secular change in ozone (using Equivalent Effective Stratospheric Chlorine (EESC) as a predictor) $f(\theta, \phi, t) = a_0 + a_1 \times \text{EESC}$. Zonal and meridional structure in daily ozone fields is accounted for by expanding both the Offset and EESC regression coefficients in full spherical harmonics

$$a = \sum_{n=0}^{n_F} \sum_{\ell=0}^{n_L-1} \sum_{m=0}^{\ell} a_{nlm} \left(\sin(2n\pi t) + \cos(2n\pi t)\right) P_\ell^m(\cos\theta) \left(\sin(m\phi) + \cos(m\phi)\right), \tag{5.12}$$

where θ and ϕ are the latitude and longitude in radians, time t is measured in decimal years and P_ℓ^m is the associated Legendre polynomial of degree ℓ and order m. Because a different model is fitted at each altitude level, and because it is the data themselves that determine the morphology of the daily ozone fields, this provides a data source more specific to each altitude level for determining the zonal mean monthly mean representativeness corrections. The optimal number of Fourier pairs and spherical harmonics to use was taken from Bodeker et al. (2013), but the order m of the spherical harmonics was restricted to a maximum of 4, i.e. $m_{\max} = \min(\ell, 4)$. Both the original SAGE II data and corrected GOMOS data are used simultaneously in these fits which extend from 1984 to 2012.

Using this model, monthly mean zonal means are calculated by evaluating the model on a 5° × 5°latitude–longitude grid at each altitude level on the 5th, 15th and 25th of each month and averaging the values. The mean representativeness correction is then given by

$$O_{3,corr} = O_{3,orig}(\theta, \phi, z, t) \times \frac{\overline{O_{3,\text{model}}}(5^\circ, z, \text{month})}{O_{3,\text{model}}(\theta, \phi, z, t)}. \tag{5.13}$$

This method has a number of challenges, especially at lower and upper levels where ozone values show a large range and have associated large uncertainties. This is especially challenging when using GOMOS ozone values which can often be negative (these cannot simply be ignored as this would result in a high bias when calculating means). The regression model fit $O_{3,\text{model}}(\theta, \phi, z, t)$ itself then often goes negative or generates values very close to zero which can cause very large corrections when used as the denominator in Equation (5.13) in the calculation of the zonal mean monthly mean sampling bias correction. Until these problems can be adequately addressed we have reverted to using total column ozone to calculate the zonal mean monthly mean sampling bias correction. One possibility to explore in the future is to use daily ozone fields from reanalyses, or from a chemistry transport model, to calculate these corrections.

Bibliography

Bertaux, J.L., Kyrl, E., Fussen, D., Hauchecorne, A., Dalaudier, F., Sofieva, V., Tamminen, J., Vanhellemont, F., Fanton d'Andon, O., Barrot, G., Mangin, A., Blanot, L., Lebrun, J.C., Prot, K., Fehr, T., Saavedra, L., Leppelmeier, G.W., and Fraisse, R.: Global ozone monitoring by occultation of stars: an overview of GOMOS measurements on ENVISAT, Atmos. Chem. Phys., 10, 12091-12148, 2010.

Bodeker, G.E., Shiona, H., and Eskes, H.: Indicators of Antarctic ozone depletion, Atmos. Chem. Phys., 5, 2603-2615, 2005.

Bodeker, G.E., Hassler, B., Young, P.J., and Portmann, R.W.: A vertically resolved, global, gap-free ozone database for assessing or constraining global climate model simulations, Earth Syst. Sci. Data, 5, 31-43, 2013.

Bogumil, K., Orphal, J., Homann, T., Voigt, S., Spietz, P., Fleischmann, O., Vogel, A., Hartmann, M., Bovensmann, H., Frerik, J., and Burrows, J.: Measurements of molecular absorption spectra with the SCIAMACHY pre-flight model: instrument characterization and reference data for atmospheric remote sensing in the 230-2380 nm region, J. Photoch. Photobio. A, 157, 167-184, doi:10.1016/S1010-6030(03)00062-5, 2003.

Chipperfield, M.P., Fioletov, V.E., (lead authors), Bregman, B., Burrows, J.P., Connor, B.J., Haigh, J.D., Harris, N.R.P., Hauchecorne, A., Hood, L.L., Kawa, S.R., Krzyscin, J.W., Logan, J.A., Muthama, N.J., Polvani, L., Randel, W.J., Sasaki, T., Sthelin, J., Stolarksi, R.S., Thomason, L.W., and Zawodny, J.M.: Global Ozone: Past and Present, Chapter 3 in "Scientific Assessment of Ozone Depletion: 2006", Global Ozone Research and Monitoring Project-Report No. 50, World Meteorological Organization, Geneva, 2007.

Damadeo, R.P., Zawodny, J.M., Thomason, L.W., and Iyer, N.: SAGE version 7.0 algorithm: application to SAGE II, Atmospheric Measurement Techniques Discussions, 6, 5101-5171, 2013.

Daniel, J.S., Solomon, S. and Albritton, D.L.: On the evaluation of halocarbon radiative forcing and global warming potentials, J. Geophys. Res., 100, 1271-1285, 1995.

Forster, P.M.d.F., and Shine, K.P.: Radiative forcing and temperature trends from stratospheric ozone changes, J. Geophys. Res., 102 (D9), 10841-10855, 1997.

Forster, P.M.d.F.: Radiative forcing due to stratospheric ozone changes 1979-1997, using updated trend estimates, J. Geophys. Res., 104 (D20), 24395-24399, 1999.

Hassler, B., Bodeker, G.E., and Dameris, M.: Technical Note: A new global database of trace gases and aerosols from multiple sources of high vertical resolution measurements, Atmos. Chem. Phys., 8, 5403-5421, 2008.

Lary, D.J., and Lait, L.: Using probability distribution functions for satellite validation, IEEE Transactions on Geoscience and Remote Sensing, 44(5), 1359-1366, 2006.

Meijer, Y.J., Swart, D.P.J., Allaart, M., Andersen, S.B., Bodeker, G.E., Boyd, I., Braathen, G., Calisesi, Y., Claude, H., Dorokhov, V., von der Gathen, P., Gil, M., Godin-Beekmann, S., Goutail, F., Hansen, G., Karpetchko, A., Keckhut, P., Kelder, H.M., Koelemeijer, R., Kois, B., Koopman, R.M., Kopp, G., Lambert, J.-C., Leblanc, T., McDermid, I.S., Pal, S., Schets, H., Stubi, R., Suortti, T., Visconti, G., and Yela, M.: Pole-to-pole validation of Envisat GOMOS ozone profiles using data from ground-based and balloon sonde measurements, J. Geophys. Res., 109, D23305, doi:10.1029/2004JD004834, 2004.

5.3 Algorithms for Merging Vertical Ozone Profile Measurements – FMI approach (WP–22)

5.3.1 Introduction

The Stratospheric Aerosol and Gas Experiment (SAGE) II solar occultation instrument from 1984–2005 and the Global Ozone Monitoring by Occultation of Stars instrument (GOMOS) from 2002–2012 measured ozone profiles from the stratosphere to the mesosphere. Global coverage, good vertical resolution, and the self calibrating measurement method make data from these instruments valuable for the detection of changes in vertical distribution of ozone over time. As both instruments share a common measurement period from 2002–2005, it is possible to inter-calibrate the data sets. We combine the data sets using inter-calibration and produce a new stratospheric ozone profile data set of 26 years. For additional details and references, see Kyrölä et al. (2013).

5.3.2 Data sets

The SAGE II and GOMOS ozone data sets used in this work are new versions. The SAGE II data version is 7.0, which was issued in November 2012. The GOMOS data version is IPF 6, which was issued in November 2012. Earlier product versions, GOMOS IPF 5 and SAGE II 6.2, have been successfully validated using ground-based measurements (For GOMOS, see Gijsel et al. (2010); for SAGE II, see Wang et al. (2002)). GOMOS IPF version 6 ozone values differ only slightly from the IPF version 5. SAGE II version 7 ozone values are 1-2% smaller than the ones in version 6.2. This difference is mainly a consequence of the change of the ozone cross section. The new cross section is now the same as the one used by the GOMOS retrieval. The preliminary validation work for this data version is underway Damadeo et al. (2013). SAGE II and GOMOS monthly average data have been compared against to several other satellite data sets in the recent SPARC Data Initiative publication Tegtmeier et al. (2013). The agreement was found be good, but in some cases the special sampling patterns of occultation measurements were found to be the reason for discrepancies (see Toohey et al. (2013)).

5.3.3 Comparison of SAGE II and GOMOS measurements from 2002–2005

Both SAGE II and GOMOS took measurements during the period of 2002 to 2005. During this time interval SAGE II measured 12 000 solar occultations (5800 sunrises and 6200 sunsets) and GOMOS 192 000 quality controlled stellar occultations during nighttime (solar zenith angle at true tangent point larger than 105°). The large number of measurements allows for a direct comparison between SAGE II and GOMOS ozone profiles. We use the following coincidence criteria (latitude=θ, longitude=ϕ, time=t):

$$\Delta\theta < 2^\circ,\ \Delta\phi < 10^\circ,\ \Delta t < 12\text{h} \tag{5.14}$$

The method used to characterize the difference at each altitude, z, for a given profile is

$$\Delta(z) = 100\frac{\langle f_S(z) - f_G(z)\rangle}{\langle f_G(z)\rangle} \tag{5.15}$$

where f_S and f_G denote SAGE II and GOMOS vertical profiles in the altitude range 20-60 km with 1 km steps. The profiles are compared directly without averaging kernels as the vertical resolutions are comparable. The brackets denote the median over all the collocated measurements.

In Fig. 5.11 we show the difference between SAGE II and GOMOS collocated ozone profiles using the coincidence criteria defined above. We show SAGE II sunset and sunrise data separately because there is a clear difference between the values of these measurements. Above 55 km the difference between day and night ozone can be seen as negative differences between SAGE II and GOMOS. For 35-55 km there is more ozone in SAGE II sunset measurements than either GOMOS nighttime

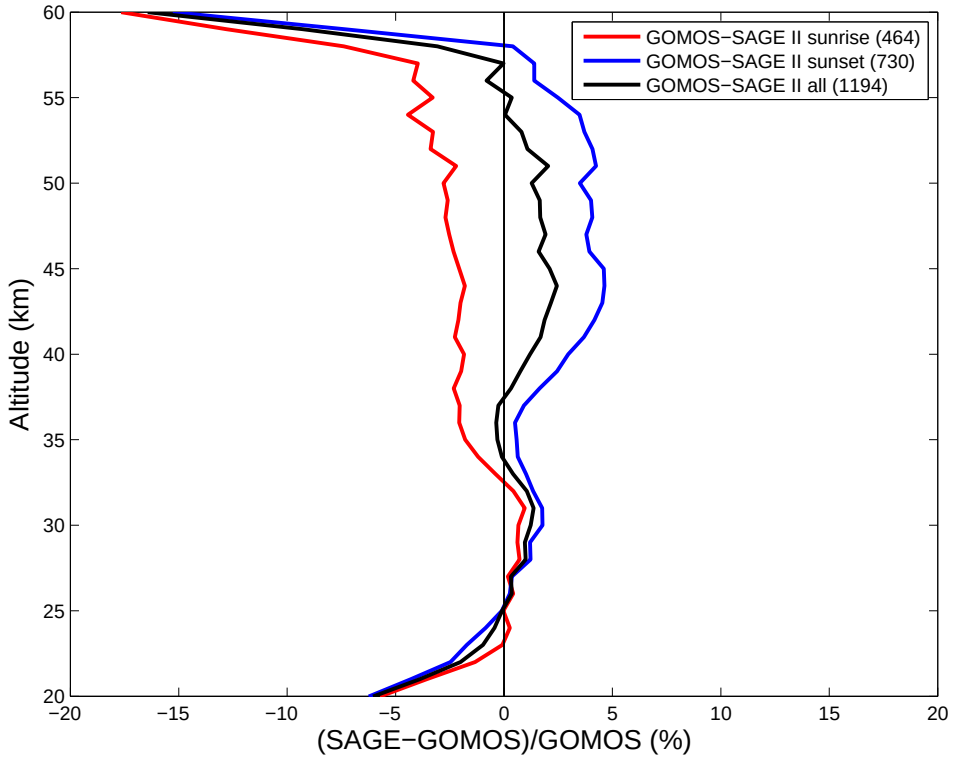

Figure 5.11: The percent difference between SAGE II and GOMOS measurements for the collocations in 2002–2005. The corresponding differences between SAGE II sunrise and sunset measurements are also shown. The line labels show also the number of collocations.

or SAGE II sunrise measurements. The overall median SAGE II difference profile is biased towards sunset measurements as the number of sunsets clearly exceeds the number of sunrises. In the 25–35 km range the differences between all the data sets are small. Below 25 km all the differences increase again and are 5% at 20 km.

The observed large diurnal differences in ozone values at altitudes below 50 km (Figs. 5.11) are in contradiction to our understanding of ozone behavior in the stratosphere. Chemical box models predict very small variations in the stratosphere. The recent detailed measurements of the ozone diurnal cycle by the SMILES instrument and simulations by chemical-transport models show (see Sakazaki et al. (2013)), however, a clear diurnal cycle of ozone in the stratosphere. SMILES results show that the magnitude between sunrise and sunset is about 4% (0.2 ppm). From Fig. 5.11 the SAGE II sunset-sunrise difference is about 6%. It remains unknown as to why the differences inferred from SMILES are smaller than the ones observed by SAGE II and GOMOS.

5.3.4 Sampling differences

We combine SAGE II and GOMOS data using a vertical grid in 20–60 km with a 1 km step. Data are averaged in zonal direction in the latitude band of 10° and covering one month. The combined data set will be limited to the latitude region 60°S–60°N in order to avoid seasonal gaps in the data. The extent in time covers years 1984–2011 (there are only a few GOMOS data from 2012 because of worsening GOMOS instrumental problems and finally because of the Envisat failure on April 8, 2012).

The relatively large size of the time-latitude cells allows natural variability of the ozone field to affect the representativity of the cell estimates. In order to quantify this we define the latitudinal or

temporal asymmetry of measurements in a grid cell as

$$a_S = \frac{2\langle x - x_c \rangle}{\Delta x}. \tag{5.16}$$

This measures the mean location of the measurements x with respect to the center of the cell centered at x_c and having width Δx. Fig. 5.12 shows time series of asymmetries and ozone densities in the latitude band 50°N–60°N. It is clear that large variability of asymmetries takes place for both instruments. In this case, there is a small SAGE II latitudinal asymmetry followed by a considerable positive asymmetry of GOMOS measurements. This may explain the change seen in the ozone densities at 40 km between SAGE II and GOMOS. In Fig. 5.13 we show the time averaged latitudinal and temporal asymmetries as a function of latitude. In the northernmost latitude band the mean SAGE II latitude asymmetry is -0.13 and GOMOS is considerably larger (0.27). At other latitudes the asymmetry differences between the two instruments are smaller and probably do not cause jumps in the time series of ozone density. The temporal asymmetry differences are smaller and we believe that they have a smaller impact on densities. In a recent articleToohey et al. (2013) the authors explore more generally consequences from uneven sampling of satellite instruments.

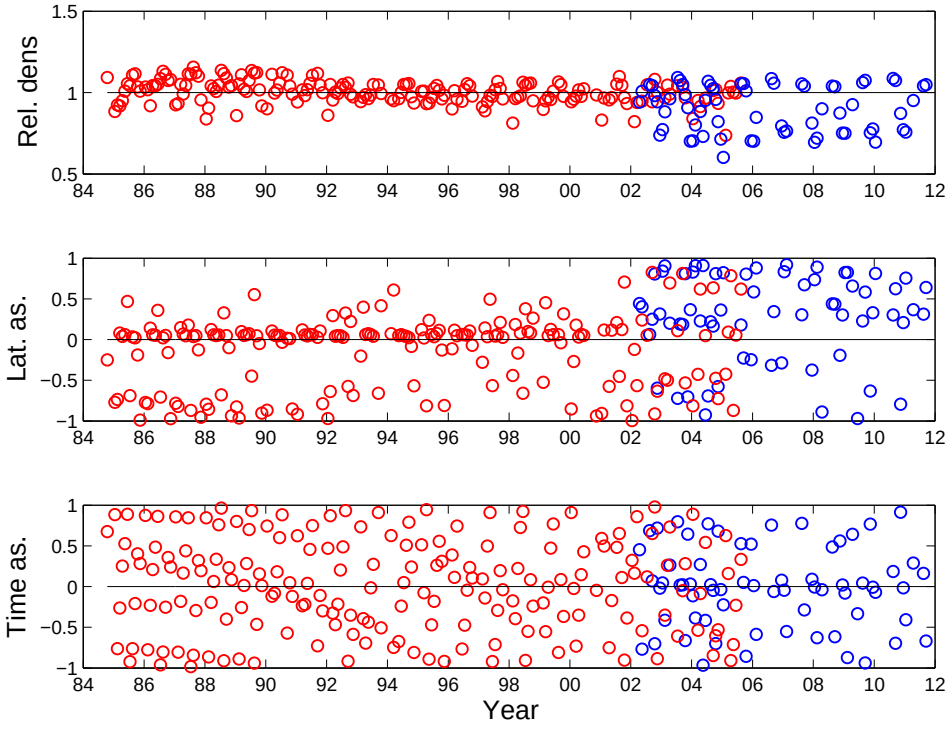

Figure 5.12: Asymmetries of the monthly time series in the 50°N-60°N latitude range. Top: GOMOS and SAGE II ozone densities at 40 km scaled by the median of the combined time series at 40 km, middle: latitude asymmetries, bottom: time asymmetries. Red circles are for SAGE II and blue circles for GOMOS data.

5.3.5 Removal of bias

It is clear that we cannot create a homogeneous data set from SAGE II and GOMOS without a proper consideration of the bias between these two data sets that was discussed earlier. We have shown that the local time of the measurements has a strong influence on the bias. In Kyrölä et al. (2013) we show that the bias profiles are nearly independent on latitude or year (2002–2005). We assume hereafter that the bias profiles derived from collocated measurements in 2002–2005 represent a constant bias

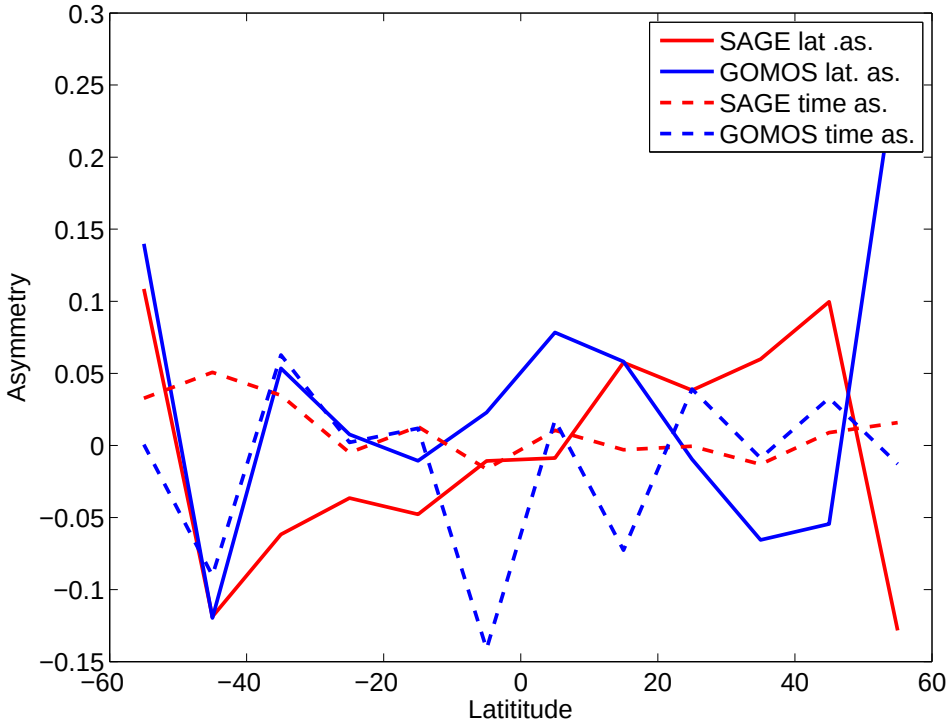

Figure 5.13: The mean latitudinal and temporal asymmetries as a function of latitude.

for the whole time period considered 1984–2011. This assumption could be tested if a stable third instrument could be found for this long time period.

The easiest solution for the bias problem would be to simply ignore any sunrise-sunset difference and correct the remaining bias from either GOMOS or SAGE II data. This would, however, require a near complete similarity between the sunrise and sunset data sets. Because this is not the case (see Fig. 5.11), we continue with the separate sunrise and sunset data.

The decisive parameter that controls the relative bias between SAGE II and GOMOS is the local hour of the measurement. Therefore, we have three measurement sets: GOMOS nighttime, and sunsets and sunrise from SAGE II. We have decided to keep the GOMOS data set as the reference and to shift the two SAGE II populations in such a way that they agree with the GOMOS data set in the common data period 2002–2005. Here, we use the average, altitude dependent bias profiles from Fig. 5.11 for sunset and sunrise SAGE II measurements. Individual profiles are shifted using the appropriate bias profile. In this way the corrected SAGE II profiles agree on average with the collocated GOMOS profiles for 2002–2005. We extend the same bias correction procedure to the SAGE II measurements from 1984 to 2001 before the common measurement period. The estimated uncertainty of the bias correction (small) is added to the error budget.

5.3.6 The combined data set

We have to decide what statistical estimators to use to characterize data in the grid cells extending 10° in latitude and one month in time. We first construct individual instrument data series and the averages in time-latitude cells are calculated by the median of the values. Outliers are removed by $|x - median(x)| > 3 \times 1.4826 \times median(|x - median(x))|$. These individual instrument time series represent the combined data set for 1984–2001 and 2006–2011. For years 2002–2005, we have measurements from both instruments. For the combined data, we have decided to take the weighted mean of the medians of the individual instrument data sets. The weights are the error estimates of the individual instrument medians. It is not obvious how to evaluate the error of the resulting

weighted mean. If the difference between the instrument medians is larger than their error estimates predict, there is good reason to believe that the two instruments have not measured a homogeneous and stationary ozone field. To allow this kind of added uncertainty, we estimate the error using the dispersion correction for weighted mean error (see `http://en.wikipedia.org/wiki/Weighted_mean`). Figure 5.14 shows examples of the individual time series and the combined time series.

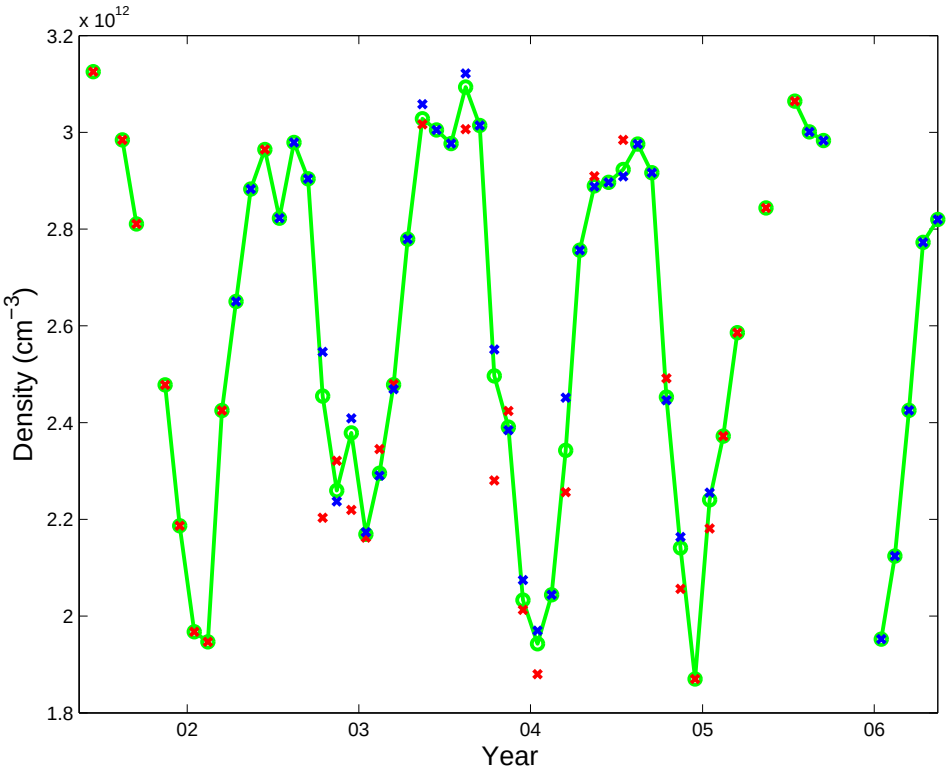

Figure 5.14: An example of the combined SAGE II and GOMOS data sets at 30 km between 40°N-50°N. Red crosses indicate SAGE II data, blues crosses indicate GOMOS data, and the green line with circles indicates the combined data.

5.3.7 Conclusions

The combined data set SAGE II–GOMOS has been used for ozone trend study in recent publications Kyrölä et al. (2013) and Laine et al. (2013). In doing so we have assumed that both the data sets, SAGE II and GOMOS, are stable in time. This is quite a natural mode of thought from researchers considering occultation instruments as self-calibrating. Several careful studies are now ongoing for investigations of possible drifts in satellite instrument ozone data.

Bibliography

R. P. Damadeo, J. M. Zawodny, L. W. Thomason, and N. Iyer. SAGE version 7.0 algorithm: application to SAGE II. *Atmospheric Measurement Techniques*, 6:3539–3561, December 2013.

E. Kyrölä, M. Laine, V. Sofieva, J. Tamminen, S.-M. Päivärinta, S. Tukiainen, J. Zawodny, and L. Thomason. Combined SAGE II -GOMOS ozone profile data set for 1984–2011 and trend analysis of the vertical distribution of ozone. *Atmospheric Chemistry and Physics*, 13(21):10645–10658, 2013.

M. Laine, N. Latva-Pukkila, and E. Kyrölä. Analyzing time varying trends in stratospheric ozone time series using state space approach. *Atmospheric Chemistry & Physics Discussions*, 13:20503–20530, August 2013.

T. Sakazaki, M. Fujiwara, C. Mitsuda, K. Imai, N. Manago, Y. Naito, T. Nakamura, H. Akiyoshi, D. Kinnison, T. Sano, M. Suzuki, and M. Shiotani. Diurnal ozone variations in the stratosphere revealed in observations from the Superconducting Submillimeter-Wave Limb-Emission Sounder (SMILES) on board the International Space Station (ISS). *Journal of Geophysical Research (Atmospheres)*, 118:2991–3006, April 2013.

S. Tegtmeier, M. I. Hegglin, J. Anderson, A. Bourassa, S. Brohede, D. Degenstein, L. Froidevaux, R. Fuller, B. Funke, J. Gille, A. Jones, Y. Kasai, K. Krüger, E. Kyrölä, G. Lingenfelser, J. Lumpe, B. Nardi, J. Neu, D. Pendlebury, E. Remsberg, A. Rozanov, L. Smith, M. Toohey, J. Urban, T. Clarmann, K. A. Walker, and R. H. J. Wang. SPARC Data Initiative: A comparison of ozone climatologies from international satellite limb sounders. *Journal of Geophysical Research (Atmospheres)*, 118:12229, November 2013.

M. Toohey, M. I. Hegglin, S. Tegtmeier, J. Anderson, J. A. Añel, A. Bourassa, S. Brohede, D. Degenstein, L. Froidevaux, R. Fuller, B. Funke, J. Gille, A. Jones, Y. Kasai, K. Krüger, E. Kyrölä, J. L. Neu, A. Rozanov, L. Smith, J. Urban, T. Clarmann, K. A. Walker, and R. H. J. Wang. Characterizing sampling biases in the trace gas climatologies of the SPARC Data Initiative. *Journal of Geophysical Research (Atmospheres)*, 118:11847, October 2013.

J. A. E. van Gijsel, D. P. J. Swart, J.-L. Baray, H. Bencherif, H. Claude, T. Fehr, S. Godin-Beekmann, G. H. Hansen, P. Keckhut, T. Leblanc, I. S. McDermid, Y. J. Meijer, H. Nakane, E. J. Quel, K. Stebel, W. Steinbrecht, K. B. Strawbridge, B. I. Tatarov, and E. A. Wolfram. GOMOS ozone profile validation using ground-based and balloon sonde measurements. *Atmospheric Chemistry & Physics*, 10:10473–10488, 2010.

H. J. Wang, D. M. Cunnold, L. W. Thomason, J. M. Zawodny, and G. E. Bodeker. Assessment of SAGE version 6.1 ozone data quality. *Journal of Geophysical Research*, 107(D23):1–18, 2002.

5.4 Extending ESA ozone CCI profiles (WP–22)

5.4.1 Extending ESA ozone CCI nadir profiles with SBUV(/2)

One of the tasks within WP22 was to demonstrate how the SBUV(/2) data set can be used to extend the ESA ozone CCI nadir profiles. We have data for 1997, 2007 and 2008 from the ESA ozone CCI and have demonstrated how the SBUV(/2) data sets can be used to provide internally consistent data for all other years for which SBUV(/2) data are available. The actual proposal calls for a demonstration of how the ESA data can be used to extend the SBUV(/2) data but this makes little sense since the SBUV(/2) data cover a wider time period than the ESA data and so we have rather shown how the ESA data can be extended using the SBUV(/2) data. If ever the ESA data come to span a longer period than the SBUV(/2) data then the same technique can be used, in reverse, to extend the

SBUV(/2) data. The approach uses SBUV(/2) data across a number of pressure levels as predictors of ESA-CCI data at a given pressure level i.e.

$$O_{3,\mathrm{ESA\_CCI}}(P_j) = a_0 + \sum_{i=1}^{N} a_i \times O_{3,\mathrm{SBUV(/2)}}(P_i) \tag{5.17}$$

where:

$O_{3,\mathrm{ESA\_CCI}}(P_j)$ is the ozone in a partial column from the ESA ozone CCI centred at some target pressure P_j.

The a_i are fit coefficients determined using a least squares fitting approach.

$O_{3,\mathrm{SBUV(/2)}}(P_i)$ is the ozone in a partial column from the SBUV(/2) data set centred at some target pressure P_i.

N is the number of pressure levels for which SBUV(/2) data are available.

Once this equation has been fitted to the available ESA ozone CCI limb data and the a_i fit coefficients have been determined, the equation can be applied to all available SBUV(/2) data to provide a proxy for the ESA ozone CCI data over time periods where the data are not available. Examples of the application of the procedure for two different latitude zones and for two different pressure layers are shown in Figu5.15. The procedure provides a robust estimate of what ESA ozone CCI nadir data would likely be during the period for which no data are available.

One potential criticism of this approach is that the relative weighting (the a_i values) applied to the partial ozone columns from SBUV(/2) might be time dependent. We tested this by replacing the a_i values with $a_i = a_{i0} + a_{i1} \times t$, where t is the decimal year. It was found that because only three years of ESA ozone CCI data are available, with the doubling of the number of fit coefficients, significant over-fitting occurs. Until more ESA ozone CCI data become available it must be assumed that the weightings applied to the SBUV(/2) partial columns are time independent.

5.4.2 Extending ESA ozone CCI limb profiles with the BS merged SAGE II and GOMOS data set

One of the tasks within WP22 was to demonstrate how the merged SAGE II+GOMOS data set generated in the first part of the WP can be used to extend the ESA ozone CCI limb profiles. For this study ESA ozone CCI limb data were only available for 2007 and 2008. The actual proposal called for a demonstration of how the ESA data can be used to extend the SAGE II+GOMOS data but this makes little sense since the SAGE II+GOMOS data cover a wider time period than the ESA data and so we show rather how the ESA data can be extended by the SAGE II+GOMOS data. An identical approach to that described by Equation (5.17) was used whereby SAGE II+GOMOS monthly mean zonal mean time series on altitude levels are used as predictors of ESA ozone CCI limb profile data on pressure levels. Examples of the performance of the method are shown for two latitude zones and two pressure levels in Figure 5.16. With only two years of ESA ozone CCI limb data being available it was not possible to test the application of this method assuming non-stationary fit coefficients (which is more likely necessary when using time series on altitude levels as predictors of time series on pressure levels).

These methods based on Equation (5.17) remove the requirement to match vertical weighting functions of nadir and limb viewing instruments. Essentially a regression model is used to determine the optimum weighting function to be applied to the SBUV(/2) data or to the SAGE II+GOMOS data to best match the ESA ozone CCI data.

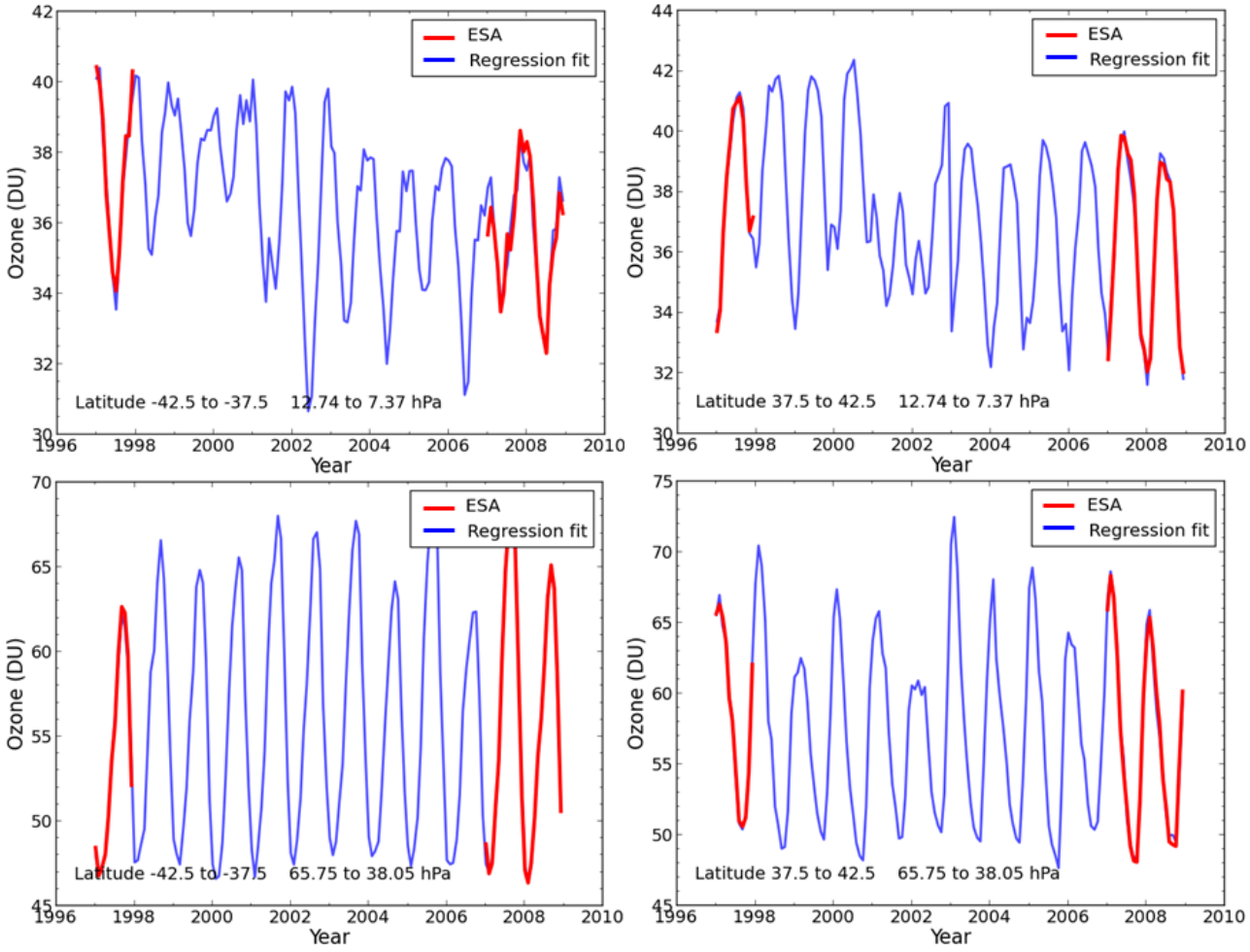

Figure 5.15: Examples of the application of Equation (5.17) to fill missing ESA ozone CCI nadir data (available in 1997, 2007 and 2008) in the intervening period (1998-2006). The red lines show the available ESA ozone CCI data while the blue lines show the regression model fit to the data and the synthetic ESA ozone CCI data generated by applying Equation (5.17), after the a_i fit coefficients have been determined, to the available SBUV(/2) data.

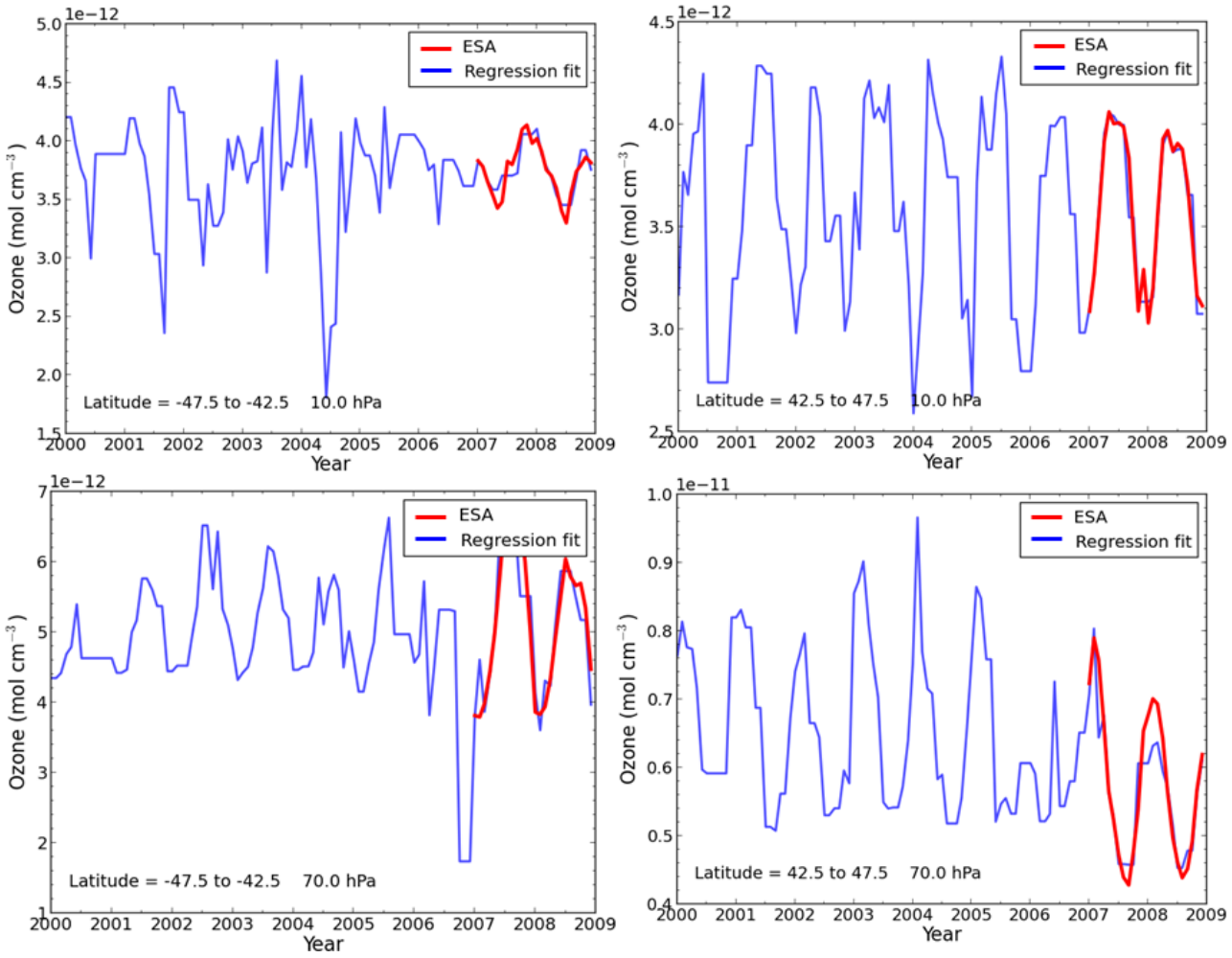

Figure 5.16: Examples of the application of Equation (5.17) to fill missing ESA ozone CCI limb data (available in 2007 and 2008) for the period 2000 to 2006. The red lines show the available ESA ozone CCI limb ozone data while the blue lines show the regression model fits to the data and the synthetic ESA ozone CCI data generated by applying Equation (5.17), after the a_i fit coefficients have been determined, to the available SBUV(/2) data.

6 Algorithm Theoretical Baseline – Water Vapor

6.1 Algorithms for the Maturation of SCIAMACHY Water Vapor Products (WP–13)

The current version of the water vapor retrieval (V3.01) from SCIAMACHY limb measurements is largely identical with the version 3 presented in Rozanov et al. (2011). The IUP-scientific retrieval processor is based on the software package SCIATRAN (Rozanov et al., 2002) Version 3.1. The water vapor retrieval from SCIAMACHY limb measurements done using the Optimal Estimation type approach (Rodgers, 2000) with first order Tikhonov constraints. Neglecting all errors, the linearized inverse problem is written as

$$\vec{y} = \vec{F}\left(\vec{x}_{\mathtt{a}}\right) + \mathbf{K}\left(\vec{x} - \vec{x}_{\mathtt{a}}\right), \tag{6.1}$$

where the mapping $\vec{F}$ represents the radiative transfer operator, $\vec{y}$ is the measurement vector, $\vec{x}$ is the state vector with the atmospheric parameters,

$$\mathbf{K} \equiv \left.\frac{\partial \vec{F}(\vec{x})}{\partial \vec{x}}\right|_{\vec{x}\,=\,\vec{x}_{\mathtt{a}}} \tag{6.2}$$

is the Jacobian matrix or weighting function matrix.

The linear inverse ill-posed problem represented by Eq. 6.1 is solved minimizing:

$$\left\|\vec{F}\left(\vec{x}_{\mathtt{a}}\right) + \mathbf{K}\left(\vec{x} - \vec{x}_{\mathtt{a}}\right) - \vec{y}\right\|^2_{\mathbf{P}} + \left\|\left(\vec{x} - \vec{x}_{\mathtt{a}}\right)\right\|^2_{\mathbf{Q}} \longrightarrow \min. \tag{6.3}$$

Here, $\mathbf{Q}$ is a constraint matrix for the state vector and $\mathbf{P} = \mathbf{S}_{\varepsilon}^{-1}$ is the inverse error covariance matrix of the measurement vector $\vec{y}$. The matrix $\mathbf{S}_{\varepsilon}$ is often referred to as the noise covariance matrix. The state vector constraint matrix, $\mathbf{Q}$, consist of two matrices, namely, the inverse a priori covariance matrix as commonly used in the optimal estimation approach (Rodgers, 2000) and a smoothness constraint matrix:

$$\mathbf{Q} = \mathbf{S}_{\mathtt{a}}^{-1} + \mathbf{R}^T\mathbf{R}. \tag{6.4}$$

The solution of the linear inverse problem given by Eq. (6.3) is obtained as follows:

$$\vec{x} = \vec{x}_{\mathtt{a}} + \Big(\mathbf{K}^T\,\mathbf{P}\,\mathbf{K} + \mathbf{Q}\Big)^{-1}\mathbf{K}^T\,\mathbf{P}\Big(\vec{y} - \vec{F}\left(\vec{x}_{\mathtt{a}}\right)\Big). \tag{6.5}$$

6.1.1 SCIAMACHY limb measurements and calibration

For the water vapor retrieval limb data from channel 6 between 1352 and 1410 nm are used. We use level 1c data version 7.03 (before 21 June 2010) and 7.04 afterward. There are two different consolidation versions for V 7.04: U and W. It was not possible to use a consistent level 1 version due to the long time necessary to process the water vapor retrieval. The influence of different level 1c data on the result were tested and are usually negligible. The spectral sampling is 0.78 nm, the spectral resolution 1.26 (FWHM) in this wavelength range. The following pixels numbers of channel 6 are excluded as bad or death pixels: 5405, 5630, 5631, 5787, 5788, 5803, 5804, and 5843. Spectra of tangent height number 6 to 10 (about 12.0, 15.3, 18.6, 21.9, 25.2 km) are used for the water vapor retrieval, i.e. the vertical sampling is about 3.3 km. The vertical instantaneous field of view of the

SCIAMACHY instrument is about 2.6 km at the tangent point, the horizontal cross-track resolution about 240 km (Rozanov et al., 2011). The spectra are calibrated for non-linearity, leakage current, pixel-to-pixel gain, stray light, and wavelength (calibration flags 0,1,2,4,5, etalon (3) does not apply for channel 6 data). No polarization correction and no absolute radiometric calibration are applied. For the limb dark correction the GADS (Global Annotation Dataset) correction is used. The limb spectra are divided by the uncalibrated ASM diffuser solar spectrum at each tangent height. For the retrieval, only the differential absorption structure is considered. This is calculated by subtracting a cubic polynomial from all measured limb and simulated spectra.

6.1.2 Auxiliary Data

The temperature and pressure profiles for the location, date and time of each limb measurement are taken from the ECMWF ERA-Interim reanalysis.

6.1.3 Cloud filter

Clouds can be identified in SCIAMACHY measurements through a color ratio method (see Savigny et al., 2005, Eichmann et al., 2009, and Rozanov et al., 2011). We use V1.9 of the cloud filter with three wavelength pairs ((750 nm, 1090 nm), (1090 nm, 1552 nm) and (1552 nm, 1685 nm)) and exclude all profiles, where clouds are detected higher than 10 km altitude.

6.1.4 Radiative transfer model

The spectra are simulated using the forward model of SCIATRAN. The single scattered contribution is calculated in a fully spherical atmosphere. The multiple scattered contribution is calculated with the combined differential-integral approach using a pseudo-spherical model with solar zenith angle and viewing angles set according to the spherical ray tracing. The refraction is taken into account during ray tracing. Weighting functions are calculated using the single scattering approximation. The forward model uses the correlated-k distribution technique (Buchwitz et al., 2000) with ESFT (exponential-sum fitting of transmissions) coefficients calculated using the HITRAN 2008 database (Rothman et al., 2009). This data set uses 10 coefficients precalculated at 20 pressure and 9 temperature grid points for 0.2 nm spectral bins. The SNR is calculated from the residuals of the spectra after the shift correction (see Sect. 6.1.5) with a correction factor of 1.5. The SNR is usually between 400 and 700 decreasing from lower to higher altitudes.

6.1.5 Shift correction

All spectra are corrected for a possible wavelengths misalignment. The misalignment can be caused by a changing illumination of the instrument entrance slit during the vertical scan and temperature distension of the detector array. The correction is performed for each tangent height independently minimizing the following quadratic form with respect to parameters s_i, $c_{\rm sim}$, and $c_{\rm sol}$ The subscript n is omitted although s_i, $c_{\rm sim}$, and $c_{\rm sol}$ are tangent height dependent.

$$\left\| \hat{I}_{\rm n}(\lambda) - \hat{I}_{\rm sol}(\lambda) - \hat{I}_n^{\rm sim}(\lambda) - \sum_{i=1}^{5} s_i \, W_{{\rm n},i}(\lambda) - c_{\rm sim} \, \frac{\partial \hat{I}_{\rm n}^{\rm sim}(\lambda)}{\partial \lambda} - c_{\rm sol} \, \frac{\partial \hat{I}_{\rm sol}(\lambda)}{\partial \lambda} \right\|^2 \longrightarrow \min. \qquad (6.6)$$

Hence, $W_{n,i}(\lambda)$ are the vertically integrated weighting functions for water vapor and methane with $i = 1, 2$ and the weighting functions for albedo, tropospheric correction, and stratospheric aerosol extinction with $i = 3, 4, 5$. A spectral point is considered as an outlier if the remaining residual is larger than six times the RMS.

6.1.6 Iterative approach

A Gauss-Newton iterative scheme (Rodgers, 2000) is applied to account for the non-linearity of the inverse problem. For x_{i+1} Eq. 6.5 results in:

$$\vec{x}_{\mathtt{i+1}} = \vec{x}_{\mathtt{a}} + \left(\mathbf{K}_{\mathtt{i}}^T\ \mathbf{P}\ \mathbf{K}_{\mathtt{i}} + \mathbf{Q}\right)^{-1} \times \mathbf{K}_{\mathtt{i}}^T\,\mathbf{P}\Big(\vec{y} - \vec{F}\,(x_{\mathtt{i}})\ + \mathbf{K}_{\mathtt{i}}\,(\vec{x}_{\mathtt{i}} - \vec{x}_{\mathtt{a}})\Big). \tag{6.7}$$

The iterative process, which is limited to a maximum of 12 steps, is stopped after one of the following convergence criteria is reached. The first criterion is that the relative change of the root mean square (RMS) of the fit residual $RMS_{i+1}/RMS_i - 1$ is lower than 10^{-3}. The second criterion is the relative change of the retrieved parameters with a threshold of 0.01%, which is defined as the maximum change in the number densities between 12 km and 23 km.

6.1.7 Methane

Absorption bands of methane are included in the retrieval. This improves the spectral fits, although the methane absorption is much weaker than the one for water vapor. Therefore, a reliable retrieval of methane is not possible.

6.1.8 Albedo

Because also the differential absorption structure is influenced by the albedo, it is included in the retrieval using the numerical perturbation method (with a perturbation of 0.3) to obtain weighting functions.

6.1.9 Tropospheric correction

The retrieval includes a tropospheric correction, i.e. the scaling of the tropospheric profile and surface elevation. In each iteration either the scaling factor for the tropospheric correction or the surface elevation is retrieved using the numerical perturbation method to obtain the corresponding weighting functions. The perturbation is 4 km in the first iteration and 2 km in all other iterations for the elevation. For the scaling of the tropospheric column the perturbation is -80%. The surface elevation is retrieved at least during the first 3 iterations. The retrieval of the scaling of the tropospheric profile is started, when the result for the surface elevation changed with less than 0.5 km between the two preceding iterations.

6.1.10 Aerosol correction

The stratospheric aerosols are assumed to be non-absorbing. The vertical profile of the aerosol extinction coefficient is estimated by fitting radiance profiles averaged around 1090 and 1552 nm. The LOWTRAN background aerosol (Kneizys et al., 1986) is used for the phase function and as a priori. For the troposphere, the retrieved aerosol extinction for the lowest altitude is maintained and the profile shape from the a priori profile is used employing a smoothing constraint of 10 km. In the water vapor retrieval a scaling factor for the aerosol profile is retrieved. The numerical perturbation method (with a perturbation of 0.5) is used to obtain weighting functions. Only altitudes higher than 10 km are perturbed to determine the scaling factor.

6.1.11 Regularization

The trace gas vertical distributions according to the US Standard 1976 model atmosphere are used as a priori for methane and water vapor. A priori uncertainties are set to 300% for water vapor, 30% for methane. Different to Rozanov et al. (2011) the a priori for tropospheric contribution, surface albedo and stratospheric aerosol scaling are not replaced after each iterative step to achieve a faster

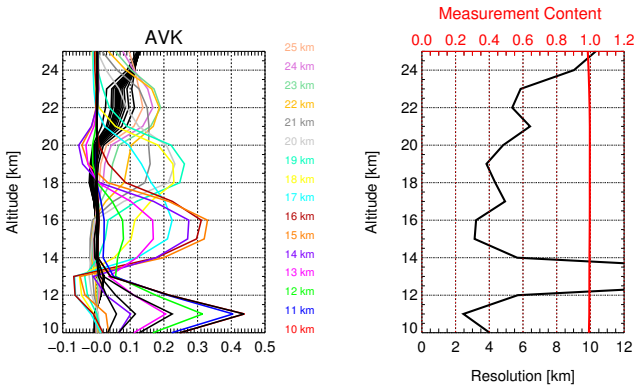

Figure 6.1: Averaging Kernels (left) and resolution (right) of a profile which is sorted out by the resolution filter.

convergence. The a priori uncertainties are: 0.1 for albedo, 30% for stratospheric aerosol scaling, 100% for tropospheric scaling, and 3 km for elevation For water vapor, the smoothness coefficient increases linearly from 5 at 10 km to 10 at 30 km, while smoothness coefficient of 1 is used at all altitude layers for methane.

6.1.12 Data filtering

The retrieved profiles are filtered based on convergence of the retrieval and RMS of the residual. Tests with different filters were performed, resulting in two different data sets, V3.01 and V3.02. Before the retrieval is performed, V3.01 is filtered for clouds (see Subsect. 6.1.3) and data which could be influenced by the South Atlantic Anomaly (SAA). Additionally, all profiles were the retrieval is not converging within 12 iterations are omitted. This is slightly different to the water vapor data in SPARC (V3.0), where profiles are only omitted, if the retrieval does not reach convergence and the RMS of the residual is larger than 0.01. For V3.02 an additional filter for the resolution is applied. The resolution is calculated as inverse of the information content, which is given by the diagonal elements of the Averaging Kernel (AVK) matrix. In V3.02 profiles are excludes, if the resolution exceeds 8 km between 11 and 20 km altitude or if a resolution is smaller or equal to zero. This should exclude profiles, with reduced data quality in parts of the profile. An analysis of the filtered data shows that many profiles in the mid and high latitudes are filtered, where the vertical distance between the lowest measurements is increased due to refraction. If a retrieval grid point falls exactly between two measurement altitudes, this results in two maximums of the AVK and unrealistic resolution values. An example is shown in Fig. 6.1, where this occurs for 13 km height. In these cases, the resolution indicates that the retrieval grid is too dense compared to the vertical sampling. This means for the effected altitudes that they contain only information from above and below, but should not decrease the quality of the profile in general. Therefore it is questionable, if the resolution filter should be applied.

6.1.13 Error Characterization

The error characterization is expected to be similar to the one for V3 presented in Rozanov et al. (2011), which is based on simulated retrieval and is summarized below. An error characterization for data V3.01 remains still to be done. Albedo, a scaling factor for aerosols and surface elevation are part of the retrieval.

1. Albedo The effects of tropospheric albedo on the retrieval is smaller than 0.5 % if an albedo of 1 or 0 is assumed and the real albedo is 0.5.

2. Tropospheric water vapor A doubling/halving of the tropospheric water vapor causes errors up to about 3 %.

3. Aerosol Errors due to stratospheric aerosols are usually smaller than 10 %. An exception is high volcanic aerosol loading, but this does occur seldom during the measurement time of SCIAMACHY and should be excluded by the cloud filter.

4. Clouds Errors due to clouds below the retrieved profile are usually about 10 %, they can reach up to 20 % for large scattering angles.

5. Surface elevation Assuming a surface elevation of 6 km when it is 2.2 km leads to an error of up to 2 %.

Bibliography

Buchwitz, M., Rozanov, V. V., and Burrows, J. P.: A correlated-k distribution scheme for overlapping gases suitable for retrieval of atmospheric constituents from moderate resolution radiance measurements in the visible/near-infrared spectral region, J. Geophys. Res., 105, 15247–15261, 2000.

Eichmann, K.-U., von Savigny, C., Reichl, P., Robert, C., Steinwagner, J., Bovensmann, H., and Burrows, J. P.: SCODA: SCIAMACHY Cloud Detection Algorithm from Limb Radiance Measurements - Algorithm theoretical basis document, Tech. rep., Institute of Environmental Physics, University of Bremen, unpublished technical document, 2009.

Kneizys, F. X., Shettle, E. P., Abreu, L. W., Chetwynd, J. H., Anderson, G. P., Gallery, W. O., Selby, J. E. A., and Clough, S. A.: Users Guide to LOWTRAN 7, Tech. rep., Air Force Geophysics Laboratory AFGL, 1986.

Rodgers, C. D.: Inverse Methods for Atmospheric Sounding: Theory and Practice,World Scientific, 2000.

Rothman, L., Gordon, I., Barbe, A., Benner, D., Bernath, P., Birk, M., Boudon, V., Brown, L., Campargue, A., Champion, J.-P., Chance, K., Coudert, L., Dana, V., Devi, V., Fally, S., Flaud, J.-M., Gamache, R., Goldman, A., Jacquemart, D., Kleiner, I., Lacome, N., Lafferty, W., Mandin, J.-Y., Massie, S., Mikhailenko, S., Miller, C., Moazzen-Ahmadi, N., Naumenko, O., Nikitin, A., Orphal, J., Perevalov, V., Perrin, A., Predoi-Cross, A., Rinsland, C., Rotger, M., Simeckova, M., Smith, M., Sung, K., Tashkun, S., Tennyson, J., Toth, R., Vandaele, A., and Vander Auwera, J.: The HITRAN 2008 molecular spectroscopic database, J. Quant. Spectrosc. Ra., 110, 533–572, doi:10.1016/j.jqsrt.2009.02.013, 2009.

Rozanov, V. V., Buchwitz, M., Eichmann, K.-U., De Beek, R., and Burrows, J. P. SCIATRAN - a new radiative transfer model for geophysical applications in the 240 – 2400 nm spectral region: The pseude-spherical version. Adv. Space. Res. 29, 11, 1831 – 1835, 2002.

Rozanov, A., K. Weigel, H. Bovensmann, S. Dhomse, K.-U. Eichmann, R. Kivi, V. Rozanov, H. V?mel, M. Weber, and J. P. Burrows, Retrieval of water vapor vertical distributions in the upper troposphere and the lower stratosphere from SCIAMACHY limb measurements, Atmos. Meas. Techn., 4, 933-954, doi:10.5194/amt-4-933-2011, 2011

von Savigny, C., Ulasi, E. P., Eichmann, K.-U., Bovensmann, H., and Burrows, J. P.: Detection and mapping of polar stratospheric clouds using limb scattering observations, Atmos. Chem. Phys., 5, 3071-3079, doi:10.5194/acp-5-3071-2005, 2005.

6.2 Algorithms for Merging Vertical Water Vapor Profile Measurements (WP–27)

6.2.1 Introduction

This section describes the algorithm proposed to merge monthly mean zonal mean water vapour data from five different satellite-based instruments. The algorithm is applied independently at each latitude and altitude. A description of the generated data product is given in the PSD.

6.2.2 The Procedure

1. Select the time series that will be used as the foundation time series i.e. the time series that all other time series will be normalized to. Data sets using two different foundation time series were generated, one using SAGE II and one using HALOE. For illustrative purposes in this section, the example using SAGE II as the foundation time series is shown.

2. Identify the instrument providing measurements with the largest temporal overlap with the foundation time series (in this case SAGE II). This is done so as to minimize the uncertainty in the difference function between the foundation time series and the incoming time series. In this case it was the HALOE time series.

3. Calculate the difference between the foundation time series and the incoming time series selected in step 2. The time dependent difference function $f(t)$ is fitted considering an offset a_1, a trend $a_2 t$, and two Fourier pairs to account for the annual cycle and semi-annual cycle:

$$f(t) = a_1 + a_2 t + a_3 \sin(2\pi t) + a_4 \cos(2\pi t) + a_5 \sin(4\pi t) + a_6 \cos(4\pi t) \tag{6.8}$$

   The fit is weighted by the uncertainty of the difference values. The uncertainty function of the difference $\sigma_f(t)$ is calculated as:

$$\sigma_f(t)^2 = \sum_{i=1}^{6} \left(\frac{\partial f(t)}{\partial a_i} \right)^2 \cdot \sigma_{a_i}^2 + 2 \sum_{i=1}^{5} \sum_{k=i+1}^{6} \frac{\partial f(t)}{\partial a_i} \frac{\partial f(t)}{\partial a_k} \cdot \mathrm{cov}(a_i, a_k) \tag{6.9}$$

   For these two functions, a_1 ... a_6 are the fit coefficients, $\sigma_{a_i}^2$ is the variance of a_i and cov(a_i, a_k) the covariance between a_i and a_k.

4. Correct the incoming time series $T_{incoming}$ and its measurement uncertainties $\sigma_{incoming}$ using the difference function $f(t)$ and the uncertainties on the differences σ_f :

$$T_{\mathrm{incoming,corr}}(t) = T_{\mathrm{incoming}}(t) + f(t) \tag{6.10}$$

$$\sigma_{\mathrm{incoming,corr}}(t) = \sqrt{\sigma_M^2(t) + \sigma_f^2(t)} \tag{6.11}$$

5. Calculate the weighted average between the foundation time series and the corrected incoming time series to create a merged temperature T_{merged} time series. Also calculate uncertainties on the merged time series σ_{merged} using the weightings $\omega_{\mathrm{foundation}} = 1/\sigma_{\mathrm{foundation}}^2$ and $\omega_{\mathrm{incoming,corr}} = 1/\sigma_{\mathrm{incoming,corr}}^2$:

$$T_{\mathrm{merged}} = \frac{\omega_{\mathrm{foundation}} \cdot T_{\mathrm{foundation}} + \omega_{\mathrm{incoming,corr}} \cdot T_{\mathrm{incoming,corr}}}{\omega_{\mathrm{foundation}} + \omega_{\mathrm{incoming,corr}}} \tag{6.12}$$

$$\sigma_{\mathrm{merged}} = \omega_{\mathrm{foundation}} + \omega_{\mathrm{incoming}} \tag{6.13}$$

   This merged data set now becomes the new foundation data set.

6. Steps 2-5 are repeated to fold in the remaining time series.

This algorithm has two exit conditions, viz:

- The data from the next instrument to be merged has less than 10 common months with the foundation time series.
- The fit coefficient a_1 is greater than 10^5

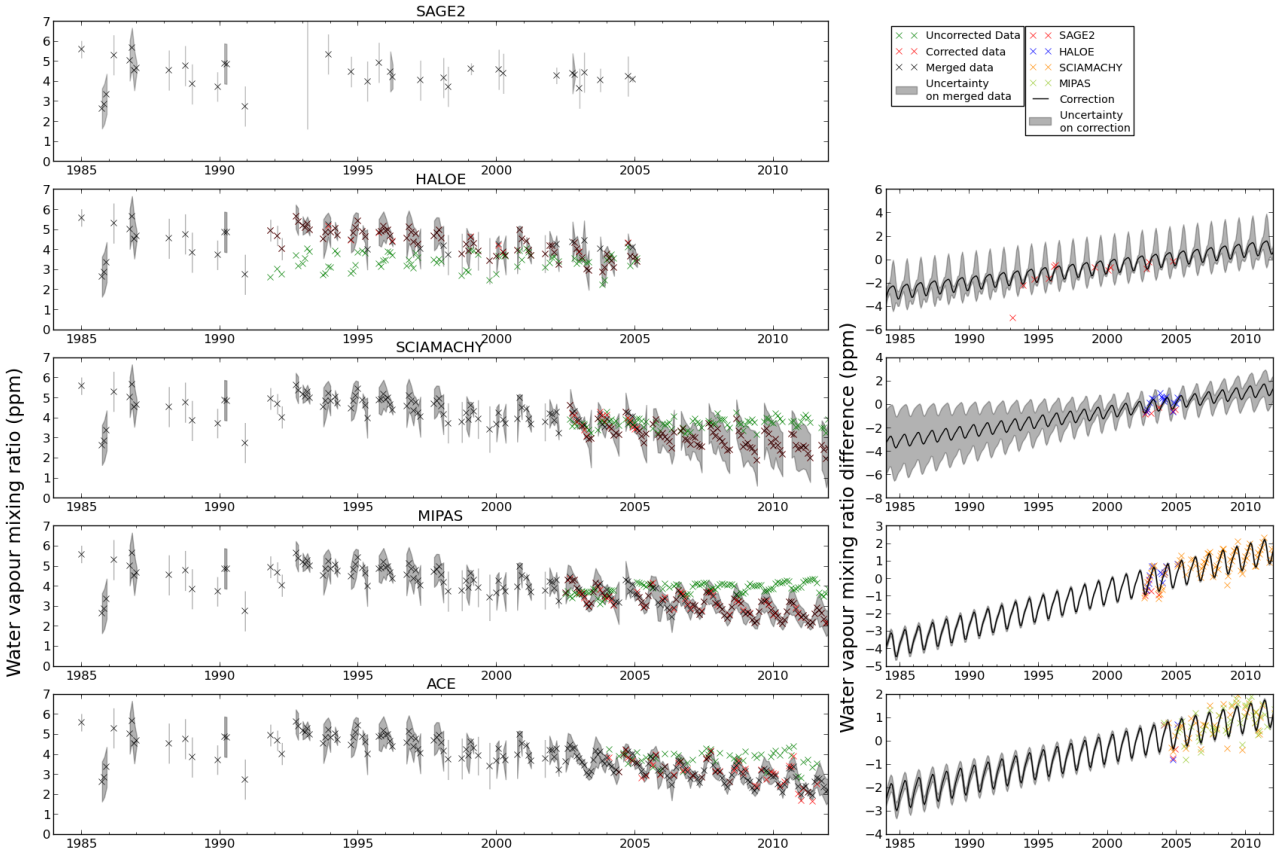

Figure 6.2: An example of the generation of the new water vapour time series using the algorithm described in Section 6.2.2, in this case showing the time series at 16 km and between 60°S and 65°S. The upper left panel shows the SAGE II monthly means and their 1σ uncertainties which form the foundation time series for the algorithm. The second row of panels shows the uncorrected HALOE monthly mean water vapour (green) in the leftmost panel and their differences against the SAGE II data in the rightmost panel (red crosses). The regression model fit to these differences is shown as a black line in the rightmost panel together with the uncertainty on the regression model fit (grey shaded area). The regression model fit is then used to correct the HALOE data which is then shown as the red crosses in the leftmost panel. The black crosses and grey shaded region in the leftmost panel show what a merged SAGE II and HALOE water vapour data set would look like. The remaining data sets are then successively folded in as described in the text. The final resultant data set is displayed as a black crosses and grey shaded region in the bottom left panel.

This process is shown graphically in Figure 6.2 for a single zone and altitude. The inclusion of each additional data set reduces the uncertainty on the final product (as long as they are appropriately

corrected). The water vapour data are more sparse compared to the data sets used in the WP24 UTLS temperature data set with the result that the merged water vapour data product does not cover all altitudes and latitude zones. Only merged data sets containing more data from more than two satellites data are included in the final data product.

7 Algorithm Theoretical Baseline – Short Lived Species

In this section the theoretical baseline of the algorithms used for creating short-lived species climatologies is described. Section 7.1 summarises the general methodology adopted for creating climatologies (including short-lived species) within the SPARC data initiative. Further, we briefly outline in Section 7.2 the algorithms used for creating "scaled" climatologies with respect to local solar time.

7.1 Algorithms for the Computation of Short Lived Species Climatologies (WP–16)

The description below is based on a draft version of the SPARC data initiative (SPARC-DI) report. For instrument specific details please consult the report.

Monthly zonal mean trace gas climatologies are calculated for each species using 5∘ latitude bins on a pressure grid with 28 levels between 300 and 0.1 hPa. The original data products are first interpolated to the SPARC pressure grid using log-linear interpolation. For instruments providing data on an altitude grid conversion from altitude to pressure levels is done using retrieved temperature/pressure profiles or meteorological analyses. The same pressure and temperature profiles are used to convert products to volume mixing ratio if number densities are retrieved. Original data have been carefully screened according to recommendations given in relevant quality documents, in published literature, or according to best knowledge of the involved instrument scientists. Zonal mean products are calculated as the average of all of the measurements on a given pressure level within each latitude bin. For some species and instruments, averaging was done in log(VMR) (instead of VMR) space. Typically a minimum of 5-10 measurements within the bin is required (depending on data set). The mean value and the 1-σ standard deviation of the measurements, along with the number of averaged data values, are given within each latitude bin at each pressure level. The mean, minimum, and maximum local solar time, average day of the month, and average latitude of the data within each bin for a selected pressure level are also provided.

For species with large diurnal variations (e.g. ClO, NO, NO_2) the measurements are separated based on the local solar time. Additional climatologies are built using a photochemical box model to scale the measurements to a common local solar time in order to enable direct comparison between products from different instruments with different spatio-temporal sampling patterns.

7.2 Algorithms for Creating Local Time Corrected Climatologies (WP–16)

Most of the instruments measure at two distinct local solar times at each latitude, either because they are in polar sun-synchronous orbit, with one local solar time for the ascending orbit and one for the descending orbit, or because they are solar occultation instruments that measure only at sunrise and sunset as seen from the satellite. The climatologies for the instruments that sample two local solar times are separated into AM and PM (or day and night). Instruments observing from non sun-synchronous orbits are characterised by drifting observation times with respect to local solar time. Climatologies for those instruments are roughly separated into daytime and nighttime measurements.

Scaled climatologies are typically calculated for 10 AM and 10 PM, the approximate local time of the Envisat/MIPAS measurements, for all short-lived species (e.g. NO, NO_2, etc.) with exception of ClO. The ClO climatologies are scaled to 1:30 AM and 1:30 PM, which is the approximate local time of the Aura-MLS measurements (for about 60°S to 60°N). Some SPARC-DI climatologies have been produced by scaling measurements to sunrise/sunset allowing for comparisons with solar occultation instruments.

$$\frac{\mathrm{VMR}^{\mathrm{observed}}(\text{corrected LST})}{\mathrm{VMR}^{\mathrm{model}}(\text{corrected LST})} = \frac{\mathrm{VMR}^{\mathrm{observed}}(\text{LST of observation})}{\mathrm{VMR}^{\mathrm{model}}(\text{LST of observation})} \tag{7.1}$$

The scaling to the corrected local solar time is done profile-by-profile, i.e. before averaging. The scaling usually uses lookup tables calculated from a photo-chemical box model initialised with climatological inputs. OSIRIS scaling factors for NO_2 are obtained from a photochemical model initialised with measured trace gas abundances and temperature. Data are filtered using molecule specific thresholds for the scaling factors. Typically, scaling factors larger than 5 are not considered reliable (subject to optimisation for each molecule). The corresponding measurements are excluded before the LST scaled climatologies are calculated. On the other hand, very small scaling factors (e.g. smaller 0.01) will simply lead to very low species concentrations (and thus a loss of measurement information), mainly determined by the diurnal variation in the model.

Other filters applied to the scaled climatologies include a minimum number of measurements requirement and a minimum measurement response treshold. Moreover, as the relevant photo-chemical models include only gas-phase chemistry, pressure-latitude regions in the lower stratosphere are excluded from the scaled climatologies during extended periods when heterogenous chemical reactions are possible. Further, the consistency of scaled model time-series obtained separately from ascending and descending orbit portions can be exploited as an internal quality criterion when it comes to trend analyses for a species under study. Intercomparisons with external data sets from other satellites, if available, provide another valuable source of information.

8 Summary and Conclusions

In this document, the algorithms applied to retrieve the products and climatologies to be delivered within the SPARC Initiative have been described. The quality of the data is addressed in the Product Validation Report.